University Of Ghana

School of Physical and Mathematical Sciences

Investigation of the Potential Changes in Ionospheric Patterns Due to Climate Variability

by

Petras Anaab Ali

(11007022)

This thesis is submitted to the University of Ghana, Legon in partial fulfillment of the requirement for the award of Master of Philosophy in Physics

Department of Physics

November 2024

DECLARATION

I, Petras Anaab Ali (11007022), confirm that this work is the result of my own study undertaken under the supervision of Dr. Eric Dominic Forson, Dr. Patrick Essien, and Prof. Nana Ama Browne Klutse. Their tremendous assistance and supervision have significantly aided the outcome of our investigation. I certify that this work has not been submitted, in whole or in part, for any other degree or certification at this or another school. All sources and references are correctly mentioned, and the study follows academic integrity and ethical norms.

14th November, 2024

------------------------- ------------------------------------

Petras Anaab Ali Date

(Candidate: 11007022)

14th November, 2024

------------------------- --------------------------------

Dr. Eric Dominic Forson Date

(Principal Supervisor)

14th November, 2024

--------------------------- ---------------------------

Dr. Patrick Essien Date

(Co – supervisor)

14th November, 2024

------------------------------ ---------------------------

Prof. Nana Ama Browne Klutse Date

(Co – supervisor)

ABSTRACT

This study examines the impact of ENSO-related climate variability on ionospheric TEC and scintillation using GNSS data from Bogotá, Antananarivo, and Baie-Comeau. The analysis contrasts a La Niña event (2020/21) with a strong El Niño event (2023/24), focusing on climate-induced ionospheric changes under similar solar and geomagnetic conditions. Findings indicate that TEC rose by 45–108% during El Niño at all sites, with ENSO accounting for 17–27% of TEC variance post solar flux adjustment, while scintillation intensity increased by 25–40%. COSMIC-2 temperature data show enhanced tropospheric and lower-stratospheric disturbances during El Niño, indicating gravity wave-mediated coupling as a key mechanism. The results underscore ENSO's substantial influence on ionospheric dynamics across various latitudes, represent the pioneering systematic ENSO-ionosphere analysis for the African equatorial region, and emphasize significant consequences for GNSS-reliant applications, where TEC variability linked to ENSO may lead to meter-level positioning inaccuracies.

ACKNOWLEDGEMENTS

I'd want to thank the Almighty God for providing me with the knowledge and strength to complete this research work.

Second, I want to thank my supervisors, Dr. Eric Dominic Forson (PhD), Dr. Patrick Essien (PhD), and Prof. Mrs. Nana Ama Browne Klutse (PhD), for their guidance and patience.

Respect and admiration to Mr. Nicholas Ali and Mrs. Fatima Ali for their invaluable assistance during my time in school, particularly during my studies. I would want to thank all of my lecturers and colleagues in my department for their help.

I thank Allah for the lives of my family members, especially my father, Mr Nicholas Ali, and my mother, Mrs. Fatima Ali, siblings (Anthony Ali and Esther Ali), and extended relatives, particularly Dr. Emmanuel Azusong and Adu Nyantakyi Allen. I could not have completed my studies without their financial assistance and prayers.

I would also like to acknowledge my church members "Church Of Christ" on campus and also at Afienya, all my roommates from first year to my final year, all Okpomates on campus, all Mensah Sarbah hall sports teams I met during my stay on campus, the various hall masters and tutors I met during my stay in the hall, all student leaders I met on campus, staffs and volunteers at Radio Univers, all sports loving people, especially Hearts of Oak family and AC Milan fans on campus. Finally, I would like to thank the persons who assisted me at my different project phases (Joshua Fafanyo Dzrobi, Amevor Kevin, Amevor Philemon and all my friends, my best wishes.

DEDICATION

I dedicate this research document to the Almighty God, my parents, Mr. Nicholas Ali and Mrs. Fatima Ali, my siblings, and the rest of my family, particularly the late Mr. Rashid Ibrahim, Mr. Haruna Aziz, and Saba Gam, whose endless love has gotten me this far and through all of this university's highs and lows. In addition, I dedicate my work to the world and all of its incredible people. I appreciate all they've done to assist me in attaining this level of educational success.

TABLE OF CONTENTS

TABLE OF FIGURES

LIST OF TABLES

LIST OF EQUATIONS

CHAPTER ONE

1. INTRODUCTION

1.1 Background to the study

The ionosphere is pivotal for radio wave transmission and satellite signals. Disturbances like ionospheric scintillation can adversely impact communication, navigation, and aviation technologies reliant on GNSS signals. Thus, comprehending the factors influencing ionospheric variability is crucial, especially as satellite-dependent systems proliferate. This significance is amplified in tropical areas like West Africa, where ionospheric irregularities are exacerbated by the equatorial ionization anomaly.

Climate variability is a potential influence on ionospheric changes. Phenomena such as El Niño and La Niña, part of the El Niño Southern Oscillation (ENSO), alter global temperature patterns and atmospheric dynamics. These changes can ascend into the upper atmosphere, impacting density, temperature, and electron concentration. Concurrently, solar radiation, geomagnetic activity, and space weather remain primary forces shaping ionospheric behavior. It is vital to discern how climate-driven factors interact with these predominant influences to grasp long-term ionospheric trends.

Research indicates that ionospheric scintillation, marked by rapid fluctuations in GNSS signal amplitude and phase, is prevalent in equatorial and high-latitude regions. In West Africa, scintillation is especially frequent post-sunset, disrupting GNSS positioning, aviation routing, telecommunications, broadcasting, and emergency navigation. As countries in the sub-region adopt satellite-supported digital services, the socio-economic consequences of ionospheric disturbances have intensified. This highlights the necessity of scientific endeavors that connect climatic variations with ionospheric reactions.

While numerous studies have explored solar activity and geomagnetic storms' effects on the ionosphere, fewer have focused on the role of climate variability over extended periods. The lower atmosphere interacts with the ionosphere via atmospheric waves and thermal structures, facilitating the transfer of energy and momentum. Temperature anomalies and circulation changes linked to ENSO events may influence total electron content (TEC) and scintillation intensity. Nonetheless, the degree and characteristics of these effects remain inadequately understood, especially in tropical African contexts.

This research investigates the impact of climate variability on ionospheric patterns by analyzing TEC and scintillation through GNSS datasets. By examining the relationship between atmospheric conditions and ionospheric responses during various climate phases, the study seeks to enhance scientific comprehension of upper-atmospheric variability. Such knowledge is essential for improving GNSS system reliability, enhancing forecasting abilities, and bolstering technological and economic activities in regions vulnerable to ionospheric disturbances.

1.2 Problem statement

Radio wave transmission and navigation systems rely on the Earth's ionosphere. Concerns about ionospheric changes, particularly scintillation, have emerged due to atmospheric variability. This issue impacts navigation and communication system reliability, causing signal degradation and reduced accuracy.

Recent research indicates variability in ionospheric parameters over different time scales, yet the impact of long-term climate variability is underexplored. While solar activity and geomagnetic storms have been studied, the influence of climate drivers such as ENSO anomalies and greenhouse gas changes on ionospheric density has received less attention.

The significance of these interactions is underscored by the growth of GNSS services in tropical Africa. West Africa, situated within the equatorial ionization anomaly, frequently experiences ionospheric irregularities. Additional variability from climate–ionosphere coupling could adversely affect aviation, maritime navigation, broadcasting, precision agriculture, and emergency-response operations in the region.

Prior studies, including Jin et al. (2022), Aol et al. (2020), and Chen et al. (2022), have shown TEC fluctuations tied to solar and geomagnetic influences, yet the impact of climatic variations over extended periods remains unclear. The lack of understanding regarding climate-driven contributions creates uncertainty in forecasting ionospheric behavior, compromising the reliability of GNSS technologies. This research aims to fill the gap by exploring the effects of climate variability on ionospheric scintillation and total electron content.

1.3 Purpose of the study

The study aims to investigate changes in ionospheric patterns due to climate variability. It specifically seeks to assess ionospheric scintillation through satellite-derived Total Electron

Content (TEC) measurements and examine how climate drivers like ENSO-related temperature anomalies and atmospheric changes influence these patterns. By considering both climate factors and established space-weather drivers, the study intends to enhance understanding of ionospheric variability processes.

Given West Africa's position within the equatorial ionization anomaly, the study also highlights the impact of climatic variability on the region's reliance on GNSS technologies, such as aviation navigation and telecommunications.

Ultimately, the study aims to fill a knowledge gap regarding the influence of climate variability on ionospheric scintillation and TEC. A clearer understanding will aid in improving forecasting models, increasing the reliability of satellite communications, and advancing the scientific comprehension of atmosphere–ionosphere interactions.

1.4 Research objectives

The study aims to elucidate the nexus between ionospheric dynamics and climatic variability. In response to the examiner's feedback, the objectives are articulated with enhanced precision regarding climatic factors, geographic scope, and utilized datasets. The specific objectives are:

1. To quantify ionospheric scintillation utilizing satellite-derived Total Electron Content (TEC) data through GNSS observations characterized by significant ionospheric irregularities.

2. To explore the impact of critical climate variability indicators, such as ENSO events, tropospheric temperature anomalies, and atmospheric circulation patterns, on ionospheric scintillation intensity and TEC variations.
3. To analyze the interaction between ionospheric scintillation and atmospheric conditions by assessing coincident atmospheric profile data to deepen the understanding of atmosphere–ionosphere coupling amid diverse climatic influences.

1.5 Research questions

Corresponding to the objectives, the study aims to address the following research inquiries:

1. What methodologies enable precise measurement of ionospheric scintillation through GNSS-derived TEC data?
2. In what manner do ENSO-induced climate anomalies, temperature fluctuations, and tropospheric circulation dynamics affect ionospheric scintillation and TEC?
3. How do ionospheric scintillation phenomena interact with or react to variations in atmospheric conditions during climate variability events?

1.6 Significance of the study

Understanding the potential changes in ionospheric patterns due to climate variability is critical for several reasons. The ionosphere plays a pivotal role in the propagation of radio waves, which are essential for communication and navigation systems globally. Any significant alteration in ionospheric behavior, particularly through phenomena like scintillation, can lead to disruptions in these systems, affecting everything from GPS accuracy to satellite communication reliability. By investigating the relationship between climate variability and ionospheric changes, this study aims to provide valuable insights that can help mitigate these potential disruptions, ensuring the continued efficacy and reliability of crucial technological infrastructure.

Moreover, this study contributes to the broader scientific understanding of the Earth's atmospheric and ionospheric dynamics. The interplay between atmospheric conditions and ionospheric behavior is complex and not fully understood. By focusing on how ionospheric scintillation is calculated and its impacts and dependencies on atmospheric variables, this research can fill significant gaps in existing knowledge. This, in turn, can inform the development of more accurate predictive models, which are essential for anticipating and responding to the impacts of climate change on the ionosphere.

The findings of this research also hold important implications for policy-making and strategic planning. As climate change continues to pose a myriad of challenges, having a detailed understanding of its effects on the ionosphere can guide the development of adaptive strategies for communication and navigation systems. Policymakers can use these insights to craft regulations and initiatives aimed at enhancing the resilience of these systems against ionospheric disturbances. Additionally, industries reliant on satellite and radio wave technologies can better prepare for and mitigate the risks associated with ionospheric variability, thereby safeguarding economic and operational stability.

Finally, this study underscores the need for interdisciplinary collaboration in addressing complex environmental issues. The intersection of atmospheric science, climate studies, and technological applications highlights how interconnected these fields are. By integrating diverse perspectives and expertise, this research not only advances scientific knowledge but also promotes a holistic approach to solving real-world problems. In essence, the significance of this study extends beyond the academic realm, offering practical benefits and fostering a deeper understanding of the intricate relationship between our planet's climate and technological systems.

1.7 Delimitations of the study

The delimitations of this study define the boundaries and scope within which the research is conducted, ensuring a focused and manageable approach. Firstly, the study is geographically confined to specific regions where extensive ionospheric and atmospheric data are available. This includes areas with established ground-based observation stations and satellite coverage that provide reliable and continuous data on ionospheric scintillation and atmospheric variables.

Secondly, the temporal scope of the study is limited to the last two solar cycles, roughly spanning from 1999 to 2021. This period provides a comprehensive dataset that captures significant variations in solar activity, which is a key factor influencing ionospheric behavior. By focusing on this timeframe, the study aims to identify trends and patterns that can be correlated with observed climatic changes.

Additionally, the research narrows its attention to those atmospheric factors that are most likely to interact with ionospheric scintillation. These consist of atmospheric composition, temperature, pressure, and humidity. The chosen variables are given priority based on their proven impact on ionospheric conditions and the availability of reliable data, even if other factors could potentially be involved. In terms of technique, the study analyses the connection between atmospheric factors and ionospheric scintillation using certain statistical and computer models. These models were picked because of their capacity to recognize intricate relationships and manage huge datasets. The study does, however, recognize that alternative modelling techniques may provide different insights and that the selected methodologies have intrinsic limits of their own.

Additionally, the research primarily relies on existing data from ground-based observation stations, satellites, and previous studies. While this ensures a comprehensive dataset, it also means that the study is limited by the quality and resolution of available data. Any gaps or inaccuracies in the historical data could impact the findings.

Finally, the study is delimited by its scope of application. While the findings are expected to provide valuable insights into the relationship between climate variability and ionospheric changes, they are primarily intended for scientific understanding and policy development. The study does not extend to the development of specific technological solutions or the implementation of practical interventions, though it may inform such efforts in the future.

By clearly defining these delimitations, the study maintains a focused and feasible approach, ensuring that its objectives are achievable within the given constraints.

1.8 Organization of the study

This thesis is structured using six chapters. Chapter One establishes the foundation by introducing the study's background, research problem, objectives, and significance. It also outlines the research questions and delimitations, and provides an overview of the thesis structure.

Chapter Two conducts a comprehensive literature review, identifying gaps and synthesizing existing research on ionospheric scintillation and atmospheric variables. Chapter three details the research methodology, describing data collection processes, analytical models, and methodologies used.

Chapter Four presents empirical findings through statistical analyses and graphical representations, examining relationships between ionospheric scintillation and atmospheric climate variables. Interpreting these findings, discussing implications, limitations, and comparing results with existing literature.

Chapter five concludes the thesis by summarizing key findings, offering recommendations for future research, and reflecting on the study's contributions to understanding climate-induced changes in the ionosphere.

CHAPTER TWO

2. LITERATURE REVIEW

2.1 Conceptual Framework for Climate–Ionosphere Coupling

Understanding climate variability's impact on ionospheric behavior necessitates a framework linking tropospheric and stratospheric processes to upper atmospheric responses. The ionosphere reacts indirectly to climate influences, with large-scale modes like ENSO affecting tropospheric dynamics, leading to anomalies in heating and winds. These anomalies generate atmospheric waves that ascend to the mesosphere-lower thermosphere (MLT), facilitating indirect climate signal transmission to ionospheric heights.

As these waves rise, increased amplitudes cause notable alterations in MLT's neutral winds and thermal structure. Through ion-neutral interactions, modified thermospheric winds generate electric fields affecting plasma distribution along geomagnetic lines, thus impacting Total Electron Content (TEC) and ionospheric irregularities linked with scintillation. The coupling between the stratosphere and ionosphere is crucial, as ENSO-induced stratospheric changes influence tidal behavior and conductivity in the E and F regions. These processes ultimately govern plasma movements, equatorial ionization anomalies, and scintillation events, illustrating the significant indirect impact of lower-atmospheric climate variability on ionospheric electrodynamics.

Solar activity and geomagnetic forces contribute to ionospheric variability alongside climate factors. Solar EUV radiation influences ionization levels, while geomagnetic activity affects energy input and circulation at high latitudes. Climate variability complements solar forcing by adjusting the ionospheric background state for solar and geomagnetic influences. Consequently, the ionospheric response is a product of atmospheric coupling and space-weather ionization dynamics. This framework outlines a chain of interactions:

1. Climate variability influences tropospheric heating and circulation.
2. These changes produce vertically propagating atmospheric waves.
3. Wave dissipation in the MLT region impacts thermospheric winds and temperature.
4. Ion–neutral interactions and tidal effects modify ionospheric electric fields.
5. Alterations in electric fields redistribute plasma, affecting TEC and scintillation.

This framework underpins the analysis of how ENSO-related temperature anomalies relate to TEC and scintillation variations. It explains the differing ionospheric responses to climate variability based on latitude, season, and solar cycle phase, particularly in equatorial Africa, where plasma control is predominant. Figure 2.1 is the flow chart for the research framework, illustrating how solar and geomagnetic forces concurrently influence the thermosphere and ionosphere.

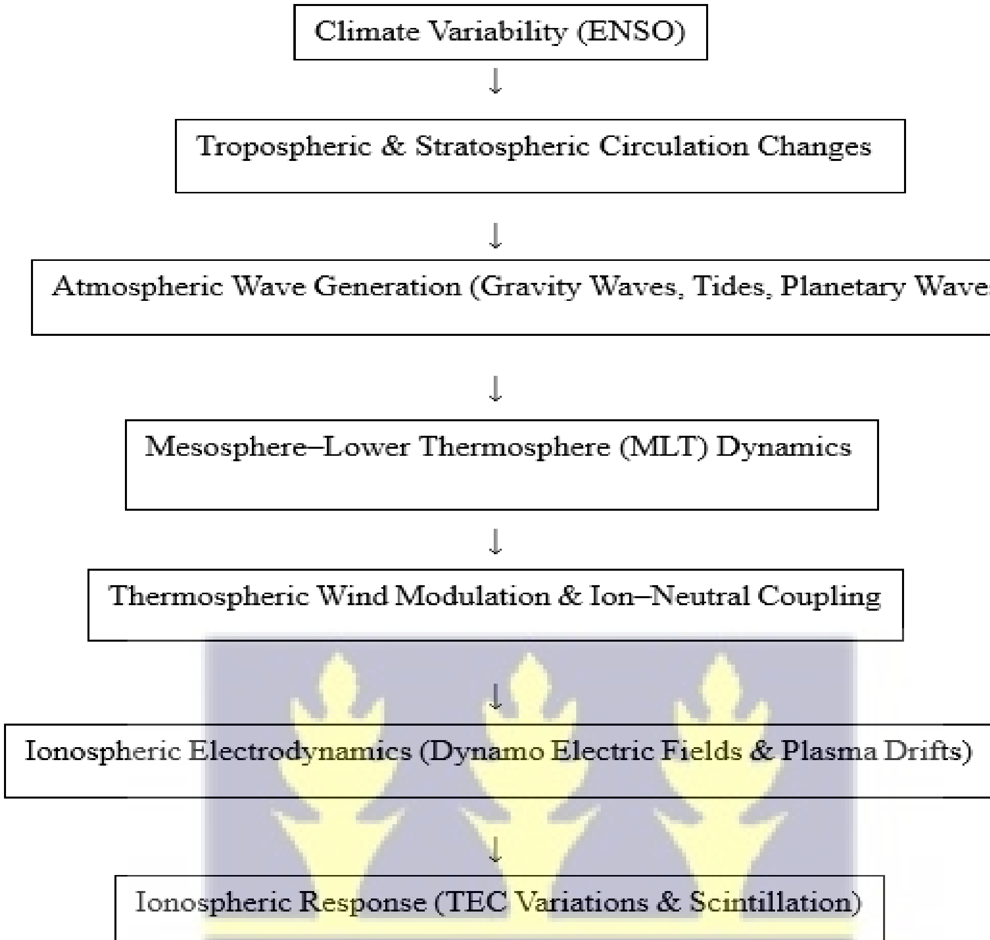

Figure 2.1: Schematic framework for climate-ionospheric coupling

2.2 The atmosphere

Andrews (2010) characterizes the Earth's atmosphere as a laboratory where numerous physical and chemical processes take place, while Salby (1996) describes it as a gaseous envelope that surrounds the globe. When researching the atmosphere, the Earth's atmosphere, like that of other planets, plays a crucial role in solar energy transfer between the sun and the planet's surface, thereby maintaining temperature equilibrium and influencing overall climatic trends.

Numerous gases, including nitrogen (N_2), oxygen (O_2), argon (Ar), carbon dioxide (CO_2), and others, make up the Earth's atmosphere. These gases are essential for life because they provide breathable air, protect the environment from dangerous radiations like ultraviolet (UV) radiation, retain heat, and prevent drastic temperature swings. Global average temperatures of around 59˚F (15˚C) would be exceeded in the absence of the atmosphere. Because it absorbs and traps radiation, carbon dioxide (CO_2(g)) is crucial for controlling temperature (Dhaka & Kumar, 2023; UCAR, 2021). As shown in Figure 2.2, the various gases that make up the earth's atmosphere are roughly 78% nitrogen, 20.95% oxygen, and 0.93% argon, with the remaining percentage being made up of other gases such as carbon dioxide, water vapor, methane, neon, etc. Other particles that are introduced into the atmosphere by human activities include dust, pollen and spores, salt from sea spray, smoke, volcanic ash, and other harmful pollutants (Allen & Cox, 2000; Dhaka & Kumar, 2023; UCAR, 2021). Aerosols are the name given to the solid or liquid particles in this list.

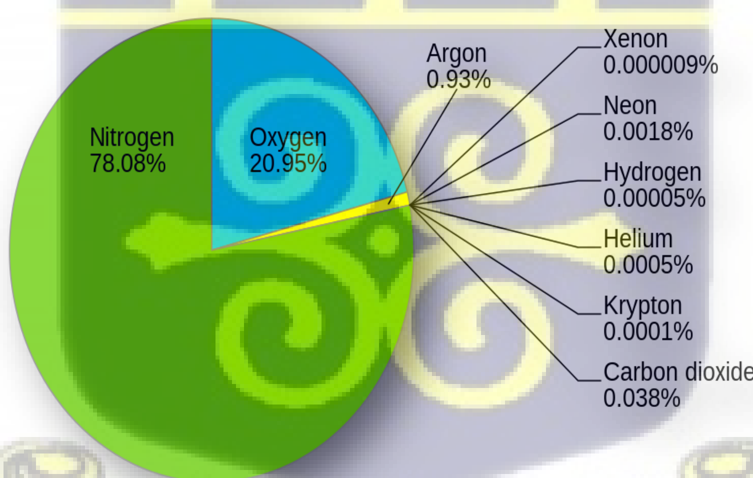

Figure 2.2: A pie chart showing the components of the Earth's atmospheric gases.
https://commons.wikimedia.org/wiki/File:Atmosphere3.svg

This layer of mixture of gases, called the atmosphere, extends from the surface of the earth to about 6,200 miles (10,000 km), and it is subdivided into five layers in a stratified manner. The commonest parameters used in dividing the atmosphere are temperature, gas composition, and the electron density or electron concentration (Knížová et al., 2021). The atmosphere's several divisions, each having unique properties and functions, are related to one another and occasionally overlap to demonstrate the atmosphere's complexity and dynamic nature. The atmosphere is categorized into the homosphere and heterosphere based on gas composition. The homosphere features a uniform gas mixture, predominantly nitrogen and oxygen, due to turbulent mixing at lower altitudes. Conversely, the heterosphere, found at higher altitudes, exhibits non-uniform gas composition influenced by molecular diffusion and ionization, resulting in increased ionized particle concentration. The ionosphere, situated within this region, is characterized by free electron concentration and significantly affected by solar radiation and Earth's magnetic and electric fields, leading to pronounced variability in electron density.

Thermally, the atmosphere is organized into distinct vertical layers that vary with altitude. According to Chamberlin et al. (1987), the vertical atmospheric structure manifests systematic alterations in temperature, pressure, density, and composition, influenced by radiative equilibrium, hydrostatic balance, and convection in the troposphere. The selective absorption of solar radiation at various wavelengths creates temperature gradients with altitude, resulting in five primary layers: the troposphere, stratosphere, mesosphere, thermosphere, and exosphere, the latter representing the boundary to outer space where gravitational influence diminishes. These layers are interspersed with boundary regions known as the tropopause, stratopause, and mesopause, which indicate transitions in thermal structure and atmospheric dynamics. Figure 2.3 depicts the vertical structure of the atmosphere, based on Microwave Limb Sounder (MLS) satellite data from 2007 to 2011 (Schwartz et al., 2008).

We can make some declarations from Figure 2.3 on the various layers of the atmosphere as a function of temperature. In the troposphere, temperature (tropospheric temperature) decreases with altitude, and this is influenced by both radiative and convective processes; all daily weather activities are carried out in the troposphere. The height of the troposphere region is approximated to be 10 km. Observing from Figure 2.3, we can see the direct opposite of the temperature – height relation (temperature inversion) in the troposphere happening in the stratosphere. Temperature is directly proportional to height in the stratosphere, and this is because the rising and sinking tropospheric air must be stopped from mixing with stratospheric air. In the mesosphere, where the atmospheric pressures are low with low density, air molecules are not likely to be seen in this atmospheric layer; that is, about ~99% of gas molecules are seen below the mesosphere, making temperatures very hot in the region. Temperatures are high in a decreasing altitude as seen in Figure 2.3, and this is because there is no ozone to absorb the ultraviolet radiation.

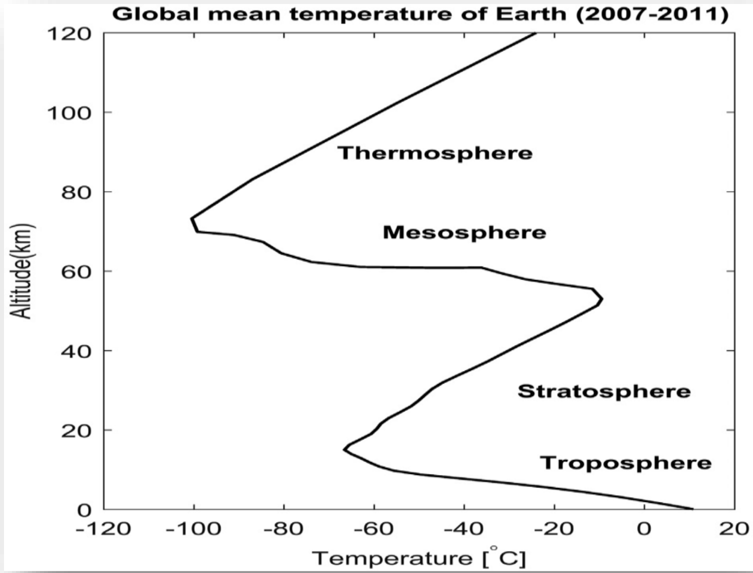

Figure 2.3: Global mean temperature profile of the Earth's atmosphere using data from 2007 to 2011. (COSMIC and MLS satellite data are used to show the mean temperature profile)

The few molecules of air that can stay in the mesosphere tend to lose more energy than they absorb. In the thermosphere, little absorption of energy can cause a great increase in temperature, and this is because of the very low air density experienced in this atmospheric layer. Combining the mesosphere with the thermosphere is what we call the ionospheric layer.

In the atmosphere, there are certain interactions that go on between the atmosphere and some electromagnetic radiations, which have different wavelengths and frequencies. Actually, the earth's atmosphere cannot be classified as an electromagnetic wave, so it does not have a definite frequency assigned to it, but rather its daily interactions with electromagnetic radiations give the layer of the atmosphere a frequency range, wavelength, forces acting there in the region, with its energies found or acting in the said region. For example, the ionosphere has a frequency range of

0.1 MHz to about 20 MHz; even with that, it's dependent on which layer of the ionosphere (D, E, F1, or F2) the radiation or particle is transmitting (Nykiel et al., 2019; Kalita & Bhuyan, 2017; Radicella & Migoya-Orué, 2021). With the atmosphere as a protective coat helping in reducing the amount of solar radiation from the sun to the earth, other forces and energies act in the atmosphere apart from the different types of waves (radio waves, microwave radiation, infrared radiation, visible light, ultraviolet radiation, X – rays and gamma rays, etc.) that exist in the atmosphere with their respective wavelengths and frequencies and these energies and forces are, gravity, coriolis force, centrifugal force, friction, pressure gradient force, all examples of active forces in the atmosphere, and examples of energies in the atmosphere are thermal energy, kinetic energy, potential energy (stored energy due to atmospheric pressure and density gradients), chemical energy (stored in atmospheric gases and aerosols), latent energy (associated with phase changes, e.g., evaporation and condensation), etc. These three parameters or factors, namely frequencies, energies, and forces, interact with each other and influence one another, shaping the atmosphere and its behaviors (Electromagnetic Spectrum - Introduction, 2023). This work is to investigate the ionospheric patterns and to know whether the disturbances in the ionosphere are as a result of climate variability, especially the temperature profile between the troposphere and the ionosphere, and for that, we shall concentrate on the ionosphere (upper mesosphere and the thermosphere).

2.3 The ionosphere

Kennelly and Heavisine hypothesized that the Earth is surrounded by an ionized atmospheric layer that acts as a reflector, preventing radio waves from escaping into space. Appleton and Barnett

(1925) proved their idea with the first direct experiment on frequency modification using the BBC transmitter in Bournemouth. The experiment demonstrated that radio waves arrived at an elevated angle, with reflection heights of 100 km to 200 km above the earth's surface (Seemala, 2023). Before Kennelly and Heaviside's idea and Appleton and Barnett's experiment, early mathematical physicists hypothesized that diffractive attenuation would prevent radio signals from being received at large distances beyond the curvature of the Earth.

This was demonstrated in 1882 when Balfour Stewart, who was researching the behavior of the Earth's magnetic field, found that the currents in the upper atmosphere could account for the daily variations in the Earth's magnetic field. The possibility of atmospheric effects on long-distance radio transmission was suggested by his reflection (Martyn, 1947). The ability to receive long-distance radio transmissions over the Atlantic Ocean was proved by Italian physicist Guglielmo Marconi nine years later in 1901 (Chamberlain & Hunten, 1987).

Following a number of atmospheric tests and investigations, it was shown that many unique ions are present in the upper atmosphere, which extends from a height of 50 km to around 1000 km. Watson and Watt coined the term "ionosphere" to describe the ionized zone, and it has since gained widespread acceptance (Seemala, 2023). Strong solar radiation dislodges electrons from molecules and atoms, forming ions with positive charges. The electron density is highly dependent on the interaction of solar activity and the Earth's geomagnetic field. The ionosphere, the upper layer of the atmosphere, is located approximately above 60 km in the Earth's atmospheric zone, as shown in fig. 2.3 (Layers of the Atmosphere, 2021).

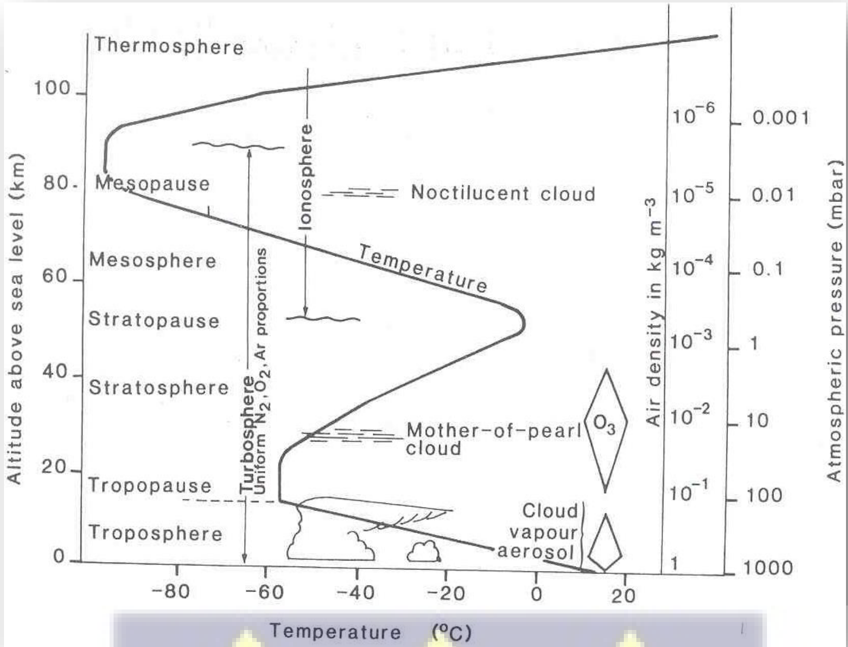

Figure 2.4: Vertical thermal structure of the atmosphere

The ionosphere is created by a process known as photo-ionization, in which neutral atoms and air gas molecules interact with solar radiation such as ultraviolet (UV) and X-rays. According to Bradbury (1938), while the E-region and F1-region are formed as a result of the absorption of specific bands of solar radiation, negative-ion formation is the predominant process in these regions, which have an abundance of electrons that cause electromagnetic waves to be reflected. He also believes that linear or beta (β) recombination does occur in some of the ionosphere's regions, particularly the D-region and the F2-region. Unlike other layers of the ionosphere, the creation of the F2-region, which is more important in the reflection of radio waves in the ionosphere, is not only ascribed to the absorption of a specific band of solar energy. The higher rate of electron-positive ion recombination, particularly during the day, increases the likelihood of the establishment of the F2-region (Chamberlain & Hunten, 1987).

Due to the flow of electrons in the ionosphere, it's capable of conducting electric currents and also serves as a medium of scattering, deflecting, and reflecting radio waves, which impact radio communication, radar, satellite systems, etc. The ionosphere, which has an upper and lower border, only has a limit for the lower barrier, which is around 50 km to 70 km above the earth's surface, whilst the upper boundary has no limit, but for the sake of experimentation and study, the upper boundary is set at 2000 km. The magnetosphere is located at higher elevations in the ionosphere and reaches up to tens of thousands of kilometers into space. Charged particles in the magnetosphere are impacted by the magnetic fields of the Earth and Sun.

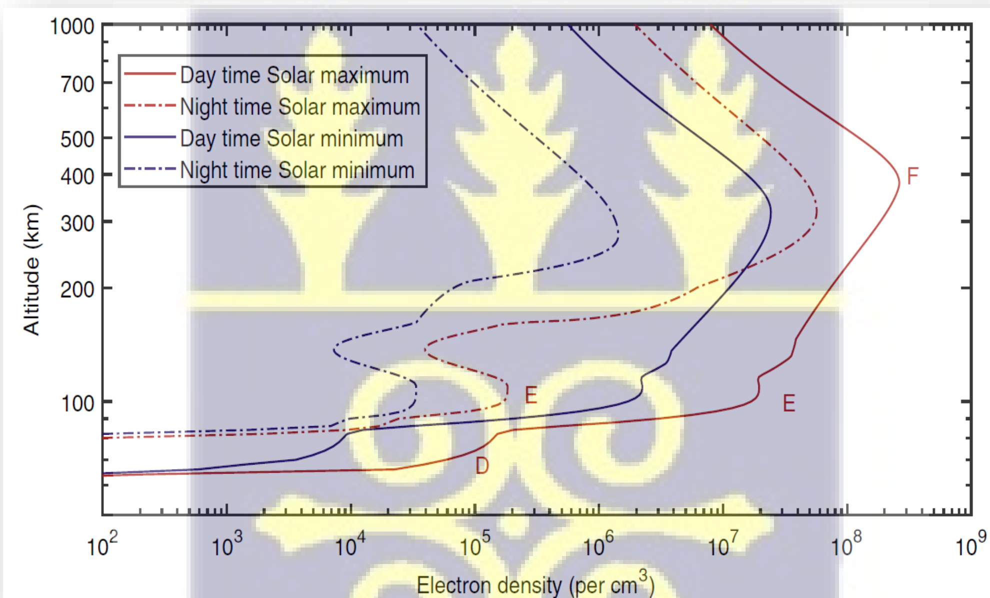

Figure 2.5: Typical variation of ionospheric density values, calculated using the IRI 2016 model, during high and low solar activity times. (Seemala, 2023)

The ionosphere's stratification, as depicted in Figure 2.5, was extensively explored by Sydney Chapman (1931) within early radio communication studies, emphasizing its significance for radio wave transmission (S. S. Rao & Singh, 2021; Chamberlain & Hunten, 1987; Seemala, 2023). It is categorized into low-, mid-, and high-latitude areas influenced by Earth's geomagnetic field and planetary rotation (Knížová et al., 2021). This intricate structure is attributed to various atmospheric gases—molecular and atomic oxygen (O_2, O), molecular and atomic nitrogen (N_2, N), hydrogen (H), and helium (He) ionizing at varying altitudes based on solar radiation wavelengths (Sankar, 2021). Ionization is predominantly through atomic oxygen above ~200 km and molecular oxygen below ~200 km, with hydrogen and helium playing a role primarily above ~600 km. The equilibrium between ionization and recombination/diffusion yields a distinct electron density profile with altitude, resulting in the formation of ionospheric layers.

These layers are traditionally categorized as the D, E, and F regions, with the F region further divided into F1 and F2 (Sankar, 2021; Seemala, 2023). The D region (approximately 50–90 km) is weakly ionized, primarily during the day due to solar radiation, while the E region (about 90–160 km) shows higher electron densities that rapidly decline after sunset. The F region, extending above ~160 km, possesses the highest electron concentrations; the F1 layer peaks near 200 km during the day and diminishes at night, whereas the F2 layer peaks around 300 km and remains the predominant ionospheric layer, increasing in altitude post-sunset. The ionosphere is highly reactive to both natural events, such as earthquakes and volcanic eruptions, and anthropogenic disturbances. Energy and momentum transfer through atmospheric coupling, facilitated by waves and electrodynamical processes like the global electric circuit, allows lower atmospheric disturbances to affect ionospheric dynamics. As evidenced by Seemala (2023), ionospheric electron density exhibits considerable variation with latitude and altitude, highlighting the necessity for ongoing investigation into the intricate electrodynamical coupling mechanisms that regulate this region. Additionally, as seen in Figure 2.6, the electron density exhibits a transient fluctuation with the time of day (diurnal variation), season (seasonal variation), and solar cycle (11-year variation).

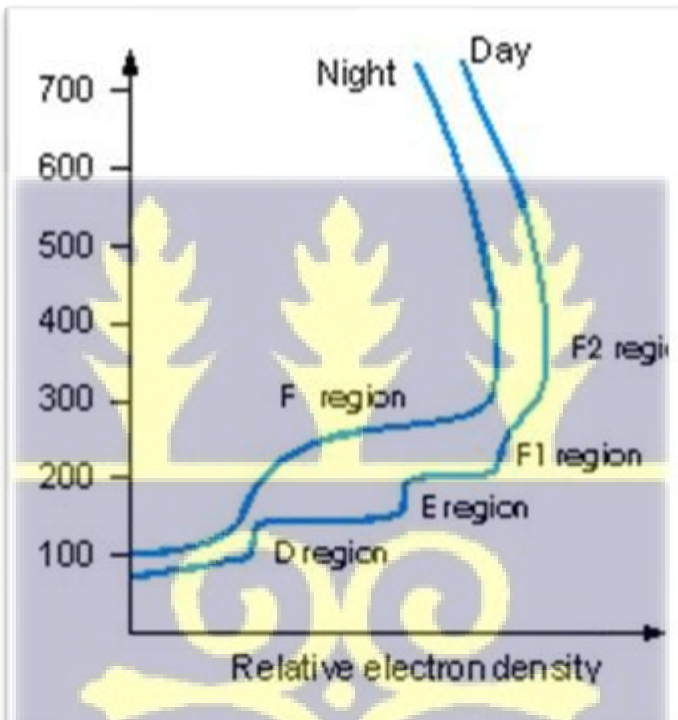

Figure 2.6: Variations of ionospheric structure during day and nighttime (Thabit et al., 2020)

Electrons in the ionosphere are affected by solar activity, which determines the total electron content (TEC) that influences electromagnetic wave refraction. Enhanced solar activity can cause particle eruptions that disrupt the ionospheric electron distribution. Such disruptions can complicate the accuracy of ionospheric models, especially during rapid electron and ion density changes. GNSS signals, traveling from satellites at approximately 20,000 km to receivers, traverse this variable plasma, where refraction impacts signal speed and travel time, potentially resulting in tracking losses (Langley et al., 2011).

The GNSS signal delay attributable to the ionosphere is mainly influenced by electron density, whereas lower atmospheric refraction depends on pressure, temperature, humidity, and other climatic factors (Langley et al., 2011). This differentiation underscores the importance of addressing both ionospheric and tropospheric influences in GNSS observation analyses. This study explores additional elements affecting GNSS signal propagation by estimating TEC and scintillation in the ionosphere and assessing the impact of climatic variability on satellite signal measurements.2.3.1 Temperature profile

Johnston et al. (2022) agreed that tropospheric annual variabilities are affected by climate variables like El Niño and La Niña, as they are connected to variations in tropical sea surface temperatures (SST), convection, atmospheric moisture, and circulation throughout the troposphere.

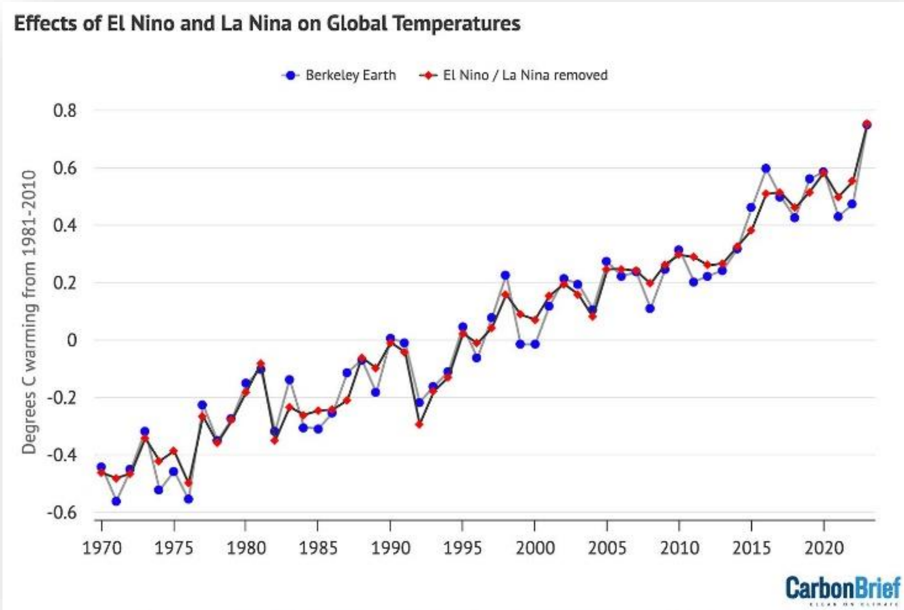

Figure 2.7: ENSO impact on global temperatures (Hausfather, 2024)

Before 2023 was recorded as the warmest year since the post-industrial era, 2016 had an annual average global temperature of 1.37˚C. With the annual global average temperature of 1.54˚C recorded in 2023, reported by the California-based research institute, Berkeley, in their Global Temperature Report of 2023 (Rohde, 2024), and making 2023 the warmest year ever in history, surpassing the normal 1.50˚C set by the Intergovernmental Panel on Climate Change (IPCC) in 2015.

From fig. 2.6, the red lines show global temperatures which had no effect of ENSO or when both El Nino or La Nina had been removed from the actual global temperatures measured by satellites under the Constellation Observing System for Meteorology, Ionosphere, and Climate (COSMIC) global navigation satellite systems (GNSSs) radio occultation (RO) FORMOSAT-2 which was launched in 2005. The blue dots describe temperatures with ENSO effects. According to Yulaeva and Wallace (1994), Fernández et al. (2004), tropical tropospheric temperatures have a positive direct relationship with ENSO, but the same cannot be said about temperatures at the stratosphere. Much studies have not been done at the stratospheric region but Scherllin-Pirscher et al. (2012), Randel and Wu (2015), Calvo et al. (2010) have concluded that moderate cooling is observed in the tropical lower stratosphere during El Nino events and the signals been propagated during ENSO activities into the stratosphere can modify the stratospheric mean meridional circulation especially at middle and high latitudes.

With several scientific institutions like the National Oceanic and Atmospheric Administration (NOAA), National Space Organization of Twain (NSPO), National Science Foundation (NFS), and University Cooperation for Atmospheric Research (UCAR) coming together to sponsor the first constellation observing system for meteorology, ionosphere, and climate (COSMIC-1) which was launched in 2006 and FORMOSAT – 7 or COSMIC – 2 GNSS Radio Occultation (GNSS-RO) also launched in 2019 (The COMET Program/MetEd, 2019) by America and Tiawan governments.

Scientific research, especially relating to space and atmospheric physics, has become quite easy after the launch of COSMIC – 1 and COSMIC – 2 GNSS – RO missions. Areas like ionosphere, climate, meteorology, geodesy, or gravity have seen much improvement in data acquisition and data analysis with both COSMIC – 1 and COSMIC – 2 data stored at the COSMIC Data Analysis and Archive Center (CDAAC). COSMIC – 1 mission data is grouped into reprocessed datasets and post-processed datasets, and each of these is divided into levels, and they are level 1a, level 1b, and level 2, with level 1b providing information on what is provided in Table 2.1.

Table 2.1: COSMIC - 1 / FORMOSAT - 3 data availability for level 1b

Dataset (reprocessed or post-processed)	Data format
Atmospheric excess phase	atmPhs format
Navigation bits used for processing open-loop data in the lower troposphere	gpsBit format
Ionospheric excess phase	ionPhs format
Clock offset values for each LEO satellite	leoClk format
LEO orbit specification file	leoOrb format
Absolute Total Electron Content and auxiliary data	podTec format
S4 scintillation index and auxiliary data	scnLv1 format

Level 2 dataset provides information on atmospheric profiles with or without moisture, ionospheric profiles, gradient–assisted ionospheric profiles, etc. Table 2.2 provides information on the FORMOSAT – 3 or COSMIC – 1 level 2 data with their respective data formats.

Table 2.2: COSMIC - 1 / FORMOSAT - 3 data availability for level 2

Dataset (reprocessed or post-processed)	Data format
Atmospheric profiles without moisture	atmPrf format
Atmospheric profiles with moisture	wetPrf format
Low-resolution, atmospheric profile in the BUFR format	bfrPrf format
ERA-40 Interim reanalysis data	eraPrf format
NCEP operational analysis data	gfsPrf format
Ionospheric profiles	ionPrf format
Gradient-assisted ionospheric profiles	igaPrf format

For level 1a of COSMIC – 1, it talks about space altitude, radio occultation antenna tracking data, and a data tracking antenna used to determine the precise orbit of the satellite. This information comes in different format. For example, the radio occultation antenna tracking data comes in opnGps format, while the precise orbit determination antenna tracking data also comes in the podCrx format or the receiver independence exchange two (RINEX2) format.

FORMOSAT – 7 or COSMIC – 2, which was launched in 2019 with the objectives of observing radio occultation of terrestrial and space weather for scientific and operational use, and to also provide ancillary space weather sensor data for operational and scientific use (Straus, 2023).

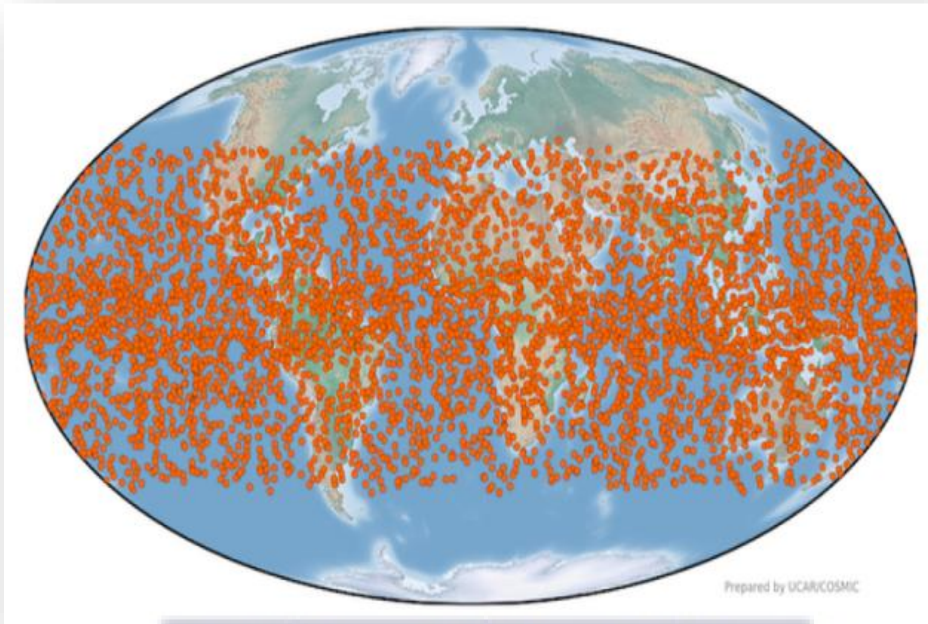

Figure 2.8: geographic coverage provided by COSMIC-2

Figure 2.9: COSMIC-2 orbit configuration

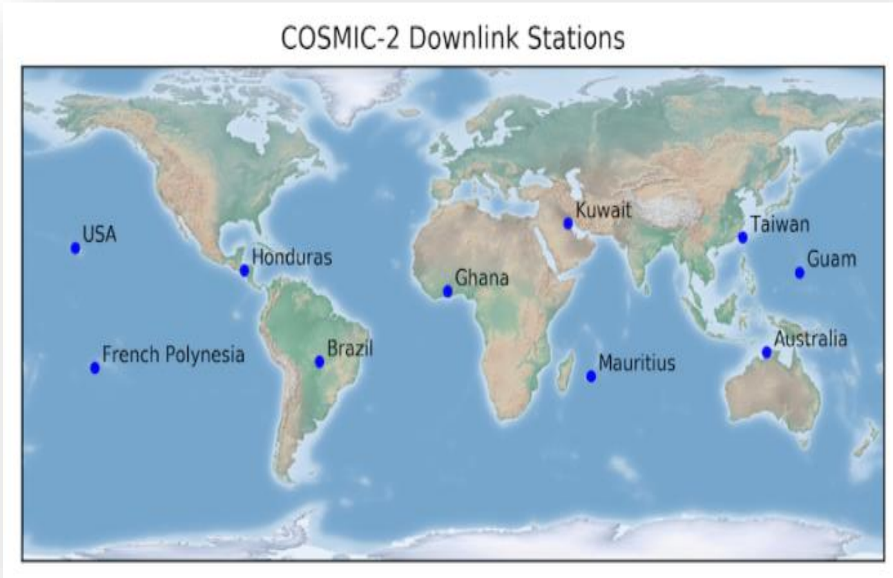

Figure 2.10: COSMIC-2 ground stations provide

Figure 2.8 shows the coverage range of COSMIC – 2 satellites with Figure. 2.10 gives us the various ground stations providing downlinks for data processing. Figure 2.9, which talks of the constellation of satellites, which is about six equatorial orbit satellites. COSMIC – 2 has provided a groundbreaking increase in the number of ionospheric and atmospheric observations, which has improved the research and operational communities of space science. With an initial inclination of 24° and an altitude of about 720 Km mean sea level (MSL), COSMIC – 2 satellites provide information on atmospheric profiles, which come in the form of .nc format. Both COSMIC – 1 and COSMIC – 1 do provide atmospheric temperature profiles. In this study, a temperature profile graph is plotted from the available temperature profile data recorded by the various satellites every minute. The temperature profile from the troposphere to the ionosphere can give us a clear indication of lower atmospheric temperatures on the ionospheric pattern, especially during the quiescent days of the sun.

2.3.2 Ionospheric scintillation and total electron content (TEC)

According to Bolaji et al. (2012), the Global Positioning System (GPS) is a satellite-based navigation system that was created by the United States Department of Defense (DoD) for military uses but was subsequently expanded for civilian use. It helps us find ourselves on Earth. The accuracy of GPS signals can be influenced by the Earth's atmosphere, with the ionosphere producing the most damage. During extreme space weather events, especially during periods of heightened solar activity, disturbances and turbulence in the ionosphere can have a negative impact on the efficacy of the Global Navigation Satellite Systems' activities. (Kumar, 2023). Goswami et al. (2018) investigated the relative performance of several satellite constellations, including the Global Positioning System (GPS) of the United States, the Globalnaya Navigatsionnaya Sputnikovaya Sistema (GLONASS) of Russia, and the Galileo Satellite developed by the European Space Agency (ESA) for the European Union (EU) under unfavorable ionospheric conditions relating to equatorial scintillations in the equinoctial months of 2014 and March 2016 at Calcutta (22.58°N 88.38°E geographic; 32°N magnetic dip), and September 2016 at Siliguri (26.72°N, 88.39°E; 39.49°N magnetic dip), which is close to the northern edge of the equatorial ionization anomaly in the Indian longitude sector. This study revealed that fluctuations in the carrier–to–noise ratio (C/No) ranged from 36.6% to 60% under constrained ionospheric conditions at both Calcutta and Siliguri stations (Kumar, 2023).

According to Seemala (2023), spatial irregularities in the phases of satellite signals are as a result of the variations in electron contents in the ionosphere. The interferences caused in signal phases can be constructive interference or destructive interference. In constructive interference, there is an increase in signal amplitude, while a decrease in signal amplitude is a result of destructive interference. These fluctuations in signal amplitude are termed ionospheric scintillation (Kintner et al., 2007) and can be seen in Figure 2.11. Ionospheric scintillation is not attributed to a space weather event according to NOAA, but it simply happens as a result of the day-night cycle of the equatorial ionosphere. Getting close to the Earth's magnetic equator are the electric field and current systems, which create instabilities in the ionosphere, which mostly peak after sunset, and this is according to the National Oceanic and Atmospheric Administration (NOAA), an institution that predicts space weather events.

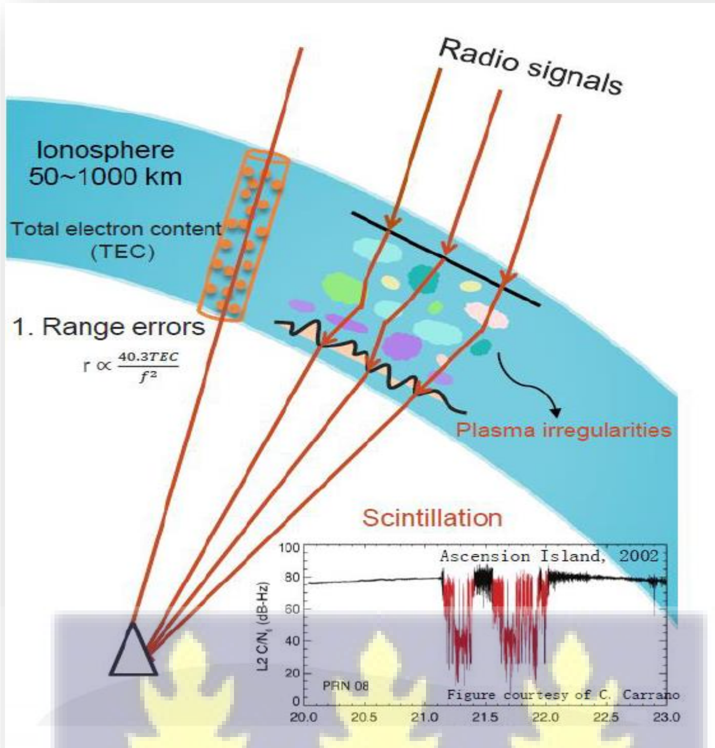

Figure 2.11: Signal delay in the ionosphere causing scintillation (Espejo et al., 2024)

Doppler shift, which occurs when there is a change in frequency due to the relative motion between the satellite and the receiver, also causes receivers to lose lock on signals from satellites (P. V. S. R. Rao et al., 2006a). During ionospheric scintillation, the destructive interference causes the power signal to be low, which affects the receiver in its ability to monitor signals from satellites. Discontinuity in TEC variations happens when there are several losses of phase lock loop (PLL) events between the receiver and the satellite, and this is known as cycle slip. Therefore, both Doppler shift and cycle slip affect ionospheric scintillation.

In calculating scintillation of the ionosphere, the total electron content (TEC) should be known since scintillation occurs when irregularities in the electron density of the ionosphere causes changes in the phase and amplitude of transmitted signals. In practice, satellite signals are lost or become very difficult to track during scintillation events. Scintillation and ionospheric activities cause difficulties in satellite-receiver signal readings. During geomagnetic storm events, the cycle slip in the polar regions is very high as TEC is affected hugely. In the day, especially at 10am, atmospheric scientists have proven that TEC increases and peaks around 2pm local time. In the ionosphere, delay of signals from satellites are being affected by geographic variability (Langley et al., 2011) in the electron content. In mid-latitude regions signals delay is typically within the range of 2m to 5m (Lu, 2006) even though the ionosphere is relatively stable as compared to the equatorial regions which has the highest electron density. The middle latitude is being affected by a larger variability correlated with auroral activity. Offenbacher and Thornstrom (2020) worked on satellite signals and found out that signals from satellites are refracted by the ionosphere and the degree of refraction is dependent on three main factors:

1. Degree of ionization (total electron content (TEC)).
2. Frequency of carrier signals.
3. Angle of incidence.

Equation 2.1 is used to calculate the degree of ionization (TEC):

$$\mathrm{TEC} = \int \mathrm{N_e}\,\mathrm{ds} \tag{2.1}$$

where N_e is the number of electrons present between the path of the satellite and receiver; ds is the path of the satellite signals. Total electron content (TEC) is normally measured in units defined by one total electron content unit (TECU) is equal to$10^{-16}m^{-2}$.

TEC values are derived from the global navigation satellite system and satellite-borne signals, but TEC values do not provide much information about the electron density profile structure of the ionosphere. To know much about the electron density profile structure of the ionosphere, a parameter known as “slab thickness” (τ) has been introduced. Slab thickness is calculated when the peak electron density (NmF_2) and the vertical total electron content (VTEC) values are known. With the combination of TEC and slab thickness, ionospheric phenomena can be easily comprehended and also, and we can determine their impact on radio wave propagation (Jayachandran et al., 2004). “The ionospheric slab thickness (τ) defined as a ratio of the total electron content (TEC) to the F-region peak electron density (NmF_2)” and has been examined during the solar maximum (1981) and minimum (1985) phases of an intense, the 21st solar cycle (Jayachandran et al., 2004). The research done by Jayachandran et al. (2004) in different latitudinal regions on the earth, Hawaii (low latitude), Boulder (mid-latitude), and Goosebay (high latitude) utilized the and concluded that ionization of F2 – layer peak electron density (NmF2) and TEC increase during the day time of magnetic quiet days of solar maximum and this results in a thicker ionosphere as compared to the night time at non-auroral latitudes. The daily peak-to-minimum values of slab thickness (Equation 2.2) varied from 1.3 to 3.75, with peak values often observed at pre-sunset hours and post-sunset hours. The day-to-day variability of slab thickness (τ) was found to vary from 10% during the day (equinox, high latitude) to 67%at night (summer, mid-latitude) during solar minimum, and from 10% during the day (winter and equinox, mid-latitude) to 56% at night (equinox, high latitude) during solar maximum.

$$\text{slab thickness}, \tau = \frac{\text{VTEC}}{\text{NmF}_2} \tag{2.2}$$

where VTEC is vertical electron density, and NmF_2 is peak electron density. Radicella and Migoya-Orué (2021) measured the signal scintillation of ionospheric irregularities; two indices used to characterize ionospheric scintillation are the phase scintillation index (σ_φ), which is represented by Equation 2.4, and the amplitude scintillation index (S_4) being seen in Equation 2.3, respectively.

$$\text{Amplitude Scintillation index}, S_4 = \sqrt{\frac{<S_i^2> - <S_i>^2}{<S_i>^2}} \tag{2.3}$$

where S_i is the carrier-to-noise ratio (C/NO) in the linear scale of the i^{th} - satellite.

$$\text{Phase Scintillation index}, \sigma_\varphi = \sqrt{< \varphi'^2 > - < \varphi' >^2} \tag{2.4}$$

where φ' is the detrended carrier phase. Pi et al. (1997) ionospheric irregularities are monitored by using the TEC change of rate (ROT), which is defined in Equation 2.5 as:

$$\text{ROT} = \frac{\text{TEC}_t^i - \text{TEC}_{t-1}^i}{t-1} \tag{2.5}$$

where i is the i^{th} - satellite; t is the time in epoch given in units of TECU. Cherniak et al. (2014) studied, processed, and analyzed the data that had been collected from three of their ground-based global navigation satellite networks in the Northern Hemisphere. In doing so, the rate of total electron content change (ROT) and the rate of total electron content change index (ROTI) parameters were used to study the occurrences of TEC fluctuations. The conclusion of the study showed that, during space weather events, the occurrences and magnitude of TEC fluctuations increase dramatically when using the GNSS network to measure. Basu et al. (1999) measurement of ROTI was able to predict the presence of scintillation causing irregularities when the Air Force Research Laboratory (AFRL) did a study to compare amplitude scintillation with fluctuations in TEC in 1998, from February to April at Ascension Islands (14.45˚ W, 7.95˚ S). The standard way of measuring the rate of TEC change (ROT) is by using the rate of TEC change index (ROTI), which is the standard deviation of ROT over a time interval (Offenbacher & Thornstrom, 2020; Radicella & Migoya-Orué, 2021) expressed in Equation 2.6:

$$\mathrm{ROTI} = \sqrt{< \mathrm{ROT}^2 > - < \mathrm{ROT} >^2} \quad (2.6)$$

Where $< ROT >$ indicates the ROT arithmetic average for the N epoch (Carmo et al., 2021). As GPS-based navigation applications grow in trans-ionospheric communications for spaceborne vehicles and surface transportation, measuring TEC has become increasingly important. According to the National Oceanic and Atmospheric Administration (NOAA), total electron content (TEC) is the total number of electrons present along a path between a radio transmitter and a receiver. The frequency of carriers can be calculated with the help of Equation 2.7:

$$\mathrm{C}_2 - \mathrm{C}_1 = \frac{40.3\,(\mathrm{f}_1^2 - \mathrm{f}_2^2) * \mathrm{TEC}_\mathrm{p}}{\mathrm{f}_1^2 \mathrm{f}_2^2} \quad (2.7)$$

where f_1 and f_2 are frequencies transmitted by satellites; C_1 and C_2 are pseudorange codes for the corresponding frequencies, f_1 and f_2 (Mannucci et al., 1998). Likewise, TEC can be calculated from phase measurements using Equation 2.8;

$$L_1 - L_2 = \frac{40.3\,(f_1^2 - f_2^2) * TEC_{\Phi}}{f_1^2 f_2^2} \quad (2.8)$$

where L_1 and L_2 are phase measurements corresponding to frequencies f_1 and f_2 (Takahashi et al., 2016). The frequencies f_1 and f_2 are constants 1575.42 MHz and 1227.6 MHz, respectively. TEC_{Φ} and TEC_p represent carrier phase TEC and pseudorange TEC, respectively. Carrano and Groves (2009), Seemala (2023) explain the differences between pseudorange TEC (TEC_p) and the carrier phase TEC (TEC_{Φ}). TEC_p measurements are being considered absolute, i.e., they provide a direct measurement of electron content along the path. In any case, the measurements tend to be noisy and are influenced by the differential code biases (DCBs), and the errors are described as systematic as a result of the differences between the satellite and the receiver. The carrier phase TEC (TEC_{Φ}) is more precise than the pseudorange TEC or code measurement TEC, but the phase TEC measurements are ambiguous. In resolving the limitations of each other, a combination of TEC_p and TEC_{Φ} is mostly used. Integrating both TECs, it is possible to improve the accuracy of TEC while minimizing phase ambiguity. Phase ambiguity is eliminated after using the code measurement TEC as a reference; the total electron content becomes more accurate and reliable.

The accuracy of ionospheric modelling depends on mapping functions, with the Klobuchar model being the most used (Langley et al., 2011). There have been improvements in ionospheric modeling in recent times, examples of such models are the Taiwan Ionosphere Model (TWIM), IGS Global Ionospheric Model (GIM), etc. (Macalalad et al., 2014), but local inhomogeneities (small–scale variations in TEC) remain a problem to be solved by scientists.

Model validation studies in African equatorial regions are notably limited. Despite some regional insights from Bolaji et al. (2012) and Skinner (1966), robust comparisons between model predictions and empirical data are lacking. This deficiency is critical, as the distinctive geomagnetic features of the African sector may yield ionospheric behaviors that diverge from those observed in other equatorial areas.

The selection of data sources warrants scrutiny. While IGS-derived TEC datasets offer extensive global coverage, they may lack the temporal resolution found in specialized GNSS scintillation monitors such as the GISTM utilized by Alfonsi et al. (2011). In the ionosphere, signals slow down when crossing, that is, the time of travel delay, and the phases of signals are advanced when crossing the ionosphere. The speed of propagation of a signal is proportional to the total electron content and is inversely proportional to the square of signal frequency, as shown in Equation 2.9:

$$\text{Ionospheric Delay}, I_f\,(m) = \frac{40.30}{cf^2}\,\text{TEC} \qquad (2.9)$$

where c is the speed of light in free space, and I_f is the time delay of a signal in the ionosphere at the L_1 band (Klobuchar, 1996). Rao et al. (2006), Adewale et al. (2012), and Bagiya et al. (2009) all generally accept that the GSV4004B receiver is the most extensively employed and deployed satellite for ionospheric research and studies. Twenty-two (22) of the total twenty-four (24) channels of the GSV4004B possess are designed to simultaneously capture L_1 and L_2 band signals from satellites. These channels are specifically engineered to record TEC and ionospheric scintillation on the L_1 frequency, which is 1575.42 MHz. The twenty–third (23^{rd}) channel is made to measure local background noise (C/No) and scintillation index S_4 correction factors. The last channel of the GSV4004B receiver is configured to monitor a satellite-based augmentation system

(SBAS), which detects phase, amplitude, and code/carrier divergence for each satellite tracked on L1 sampling rates of 50 Hz and 1 kHz, respectively (Kumar, 2023).

To enhance the accuracy of the final navigation solution, the previous reliance on a single frequency band (L_1) for total electron content (TEC) estimation has been upgraded to incorporate dual-frequency bands, namely L_1 and L_2 (Bolaji et al., 2012). The dispersive nature of the ionosphere refracts radio signals, causing time delay with Equation 2.9 (Ginzberg, 1970; Chen, 1984; Davies, 1989; and Hofmann-Wellenhof et al., 2001).

An advantage of using a dual-frequency receiver instead of a single-frequency receiver is that it can concurrently utilize 1575.42 MHz for L_1 and 1227.60 MHz for L_2 frequencies (Carrano and Groves, 2009; Kumar, 2023; Bolaji et al., 2012). This setup facilitates the measurement of the relative phase delay between the two signals, known as slant TEC (STEC) (Bolaji, 2012). Kumar (2023) defines Slant TEC (STEC) as "the electron column density along an oblique line of sight." This statement simply means that STEC measures the total number of electrons between the satellite and the receiver, but not necessarily in the path of the receiver's location. The global position satellite moves across different parts of the atmosphere, and the electron content of the ionosphere varies both spatially and temporally. STEC values can't be used to accurately describe the ionospheric conditions at a specific location, and the reason is that STEC is affected by the satellite's elevation angle and the varying electron density in the ionosphere. To have the exact ionospheric condition at a particular place, slant TEC should be converted to vertical total electron content (VTEC), and this is done by making some assumptions about the ionosphere and the plasmasphere as shown in Equation 2.10. Some of these assumptions are:

1. The ionosphere and the plasmasphere are horizontally stratified.
2. The stratification of the ionosphere and the plasmasphere is also considered to be spatially uniform.

The above assumptions allow us to use the ionospheric thin shell mapping function, and this mapping function enables us to convert slant TEC to vertical TEC at a specific location called the ionospheric piercing point (IPP), which is estimated to be an altitude of about 350 km (Alfonsi et al., 2011) above the earth's surface, as displayed by Figure 2.12

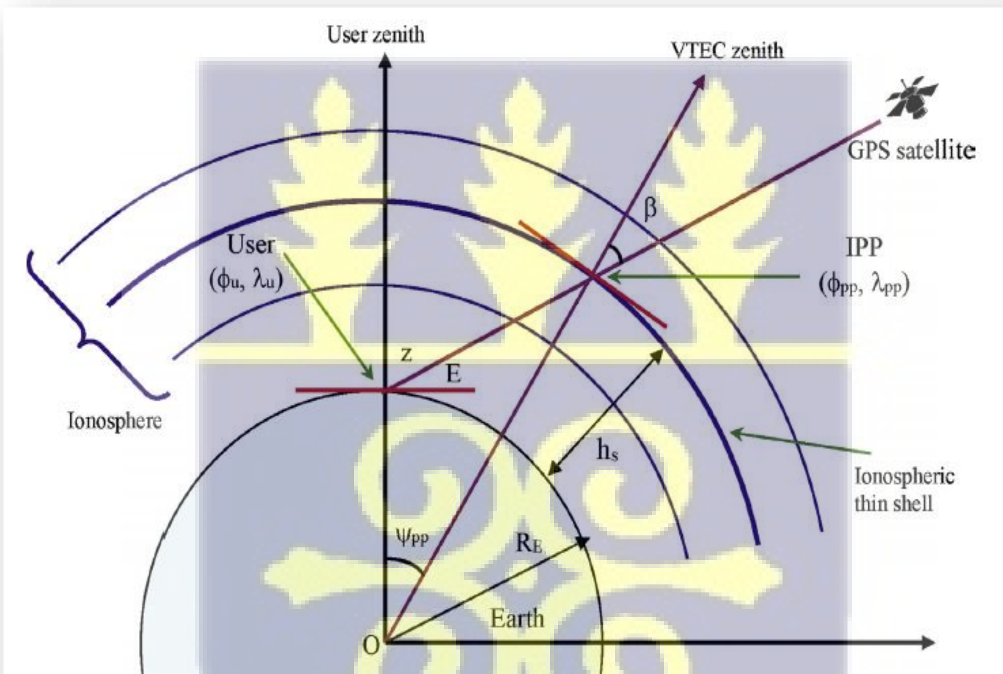

Figure 2.12: Schematic of Slant TEC to Vertical TEC conversion (Seemala, 2023)

$$VTEC = STEC - \frac{[b_R + b_s + b_{RX}]}{S(E)} \tag{2.10}$$

$$S(E) = \{1 - (\frac{R_E * Cos\,(E)}{R_E + h_s})^2\}^{-0.5} = \frac{1}{Cos\,(z)} \tag{2.11}$$

From Equations 2.10 and 2.11, STEC is uncorrected slant TEC measured by the receiver, S(E) is the obliquity factor shown in Equation 2.11, with zenith angle, z is the ionospheric piercing point (IPP), E is the elevation angle of the satellite in degrees, N_e is the electron density, ds is the path of the integration, R_E is the mean radius of the earth measured in Km, h_s is the height of the ionosphere from the surface of the earth, b_s is the satellite differential delay, b_r is the receiver differential delay, and b_{RX} is the receiver inter-channel bias (Alfonsi et al., 2011).

Various IGS associate analysis centers (IAAC) provide VTEC values, which can be used in different applications like climate modelling that stimulate the ionosphere's electron density. Assimilating these vertical total electron content values into climate models involves combining them with the model's prediction using data assimilation techniques, and this allows the model to incorporate real-world data and improve its accuracy. The outcome of this assimilation process is a weather-like representation of the ionosphere's electron content in all time ranges, including past conditions, current conditions, and forecasting or future conditions (Radicella & Migoya-Orué, 2021).

2.4 Climate variables and their impact on ionospheric scintillation

Macalalad et al. (2014), Seemala (2023) agreed that, ionospheric disturbances (scintillation) that cause delay in travelling signals from the satellite to the receiver on earth is been affected by many factors such as location of receiver, time of day, solar activity, earth's magnetic field, etc. After the emergence of upper atmospheric physics and space research, many of the upper atmospheric scientists have come to agree that latitudinal change have a great effect on the measurement of TEC. Langley et al. (2011) said, the refraction of signals in the troposphere and stratosphere is a function of atmospheric pressure, temperature, etc. but are the refraction of these signals able to cause loss of lock of the signals by the receivers on earth? The latitude has been subdivided into three main regions namely, high latitude, mid-latitude, and low latitude.

Most scientific researches have been done at the mid-latitude because the mid-latitude exhibits clearly daily and seasonal variations. The low latitude has a dynamic ionosphere and its very sensitive to plasma instabilities as a result of the magnetospheric ring currents. In general, the ionospheric disturbances are linked to the activities of the sun like sunspot activity (P. V. S. Rao et al., 2006), geomagnetic storms (Prikryl et al., 2015), low solar activity (Bolaji et al., 2012) etc. and they are either direct or indirect. These different regions have different weather and climate characteristics.

In equatorial (< 10˚) and low latitude (10˚ to 30˚) regions , there is the highest electron density (Langley et al., 2011) and many researches who have studied the lower latitude like Davies & Hartmann (1997), Liu and Chen (2009), P. V. S. R. Rao et al. (2006b), Zhao et al. (2005), Essien et al. (2018) have all confirmed that TEC values significantly vary during certain times of the day which the strongest TEC sensitivity happens during pre-sunrise periods and that of great magnitude during the day and this is as a result of both extreme solar ultraviolet ionization and the upward vertical drift (E x B). Bagiya et al. (2009) concluded that the severity of the equatorial ionization anomaly has a significant impact on the maximum daytime peak TEC values in low latitude locations. Their study analyzed GPS satellite signals at Rajkot, India, to study ionospheric variations in Total Electron Content (TEC) during low solar activity periods from 2005 to 2007. The results show maximum TEC during Equinoctial months (March, April, September, October), minimum during Winter months (November, December, January, February), and semi-annual variation during Summer (May, June, July, August). The ionospheric total electron content (TEC) variations over the low-latitude regions are tough to model and predict this is because of the equatorial ionization anomaly (EIA) present (Shenvi & Virani, 2023).

The ionospheric scintillation effect principally occurs in these three regions, equatorial region, auroral region, and the polar regions and these three regions have and in these various regions, there exist different physical processes leading to the formation of electron density irregularities (Tiwari et al., 2010). Jiao and Morton (2015) confirmed what Tiwari et al. (2010) said by juxtaposing scintillation effect at high-latitude and at equatorial region on GPS signals during the maximum of solar cycle 24. Jiao and Morton (2015) concluded that scintillation at the equatorial zone is much severe and last longer as compared to scintillation effects at high latitudes which has a more moderate effect and this is characterized by phase fluctuations rather than amplitude fluctuations. The study which was conducted at Alaska, Ascension Islands, Jicamarca, Peru, and Gakona showed that effect of scintillation is dependent on geographic location during geomagnetic activities, solar activities, and seasonal changes. Jiao et al. (2013) in their earlier publication titled "Characterization of high-latitude ionospheric scintillation of GPS signals" showed that, at high latitudes, scintillation is mostly characterized by phase scintillation and not amplitude scintillation. According to Basu et al. (2002), irregularities in the ionosphere especially during solar maximum happen in the equatorial regions and the high latitudes.

Scintillation, which is been affected by latitude is also affected by activities of the sun. These activities are geomagnetic storms, solar flares, sunspots, etc. The tropospheric climate may not have a direct influence on ionospheric scintillation but we can use the climate variables like ENSO (El Nino – Southern Oscillation) levels at different regions of the equator to examine the temperature profile from the troposphere to the ionosphere and its influence on ionospheric patterns. Studies have shown that, it is difficult and challenging to see a direct impact of El Nino and La Nina on the ionosphere and this is because of the complexity of the atmosphere's ionospheric system (Pedatella & Forbes, 2009; Chang et al., 2018). According to the World Health Organization (2023) countries in the tropics (Africa, Latin America, South and South- East Asia) are mostly affected by La Nina and El Nino. Since ENSO causes a shift in the global climate and thus disrupts the atmospheric circulation pattern which connects the tropics to the mid-latitude jet streams. La Nina which is the cold part of ENSO, and El Nino, which is the warm part of ENSO become one of the major sources of annual global climate variability, which is second to the sun's influence on earth's climate. Even though, it is difficult to monitor the signature of ENSO on the ionosphere, scientist have been able to prove that, ENSO has a link with the distribution of electrons and ions in the atmosphere. Sun et al. (2019) confirmed that ENSO's La Niña phase, influenced the thermospheric wind diurnal eastward 3 (DE-3) and stationary planetary wave 4 (SPW-4) in the northern hemisphere during a period of low solar activity (2007-2011). The influence of La Nina (strong Lanina years of 2010/2011) in the ionosphere's DE-3 and SPW-4 had an impact on the distribution of electrons in the ionosphere which directly had an impact on the total electron content (TEC). They used data collected by the FORMOSAT - 3/COSMIC satellites to measure electron density. Before Sun et al. (2019) conclusion, Chang et al. (2018) had made a prediction on La Nina and El Nino having an indirect influence on the ionosphere's E layer. They said, the dense sporadic E (Es) of the ionosphere's E – layer contains ionized metals which can disrupt radio signals as a result of scintillation. The phase fluctuations (S_4) index in the mid-latitude E-layer showed an unknown connection to ENSO variations in the troposphere. These tides influence wind shear convergence, affecting metallic ion accumulation in the lower thermosphere (above the E-region). The modulated wind shears then affect the formation of sporadic E (Es) layers, leading to variations in the extreme scintillation based on the ENSO cycle.

During ENSO phases, tidal modulation influences the zonal electric field E_x, impacting:

1. Pre-reversal enhancement (PRE) strength
2. Equatorial ionization anomaly (EIA) intensity
3. Growth rate of equatorial plasma bubbles
4. Scintillation onset timing and spatial coverage

ENSO-related ionospheric responses exhibit significant longitude dependence, with studies primarily in the Asian, Pacific, and American sectors due to available GNSS and satellite networks. Findings indicate ENSO does not yield uniform global responses; rather, they are influenced by background winds, geomagnetic configurations, and regional conductivity.

Chang et al. (2018) concluded by saying "results indicate that ENSO signatures can be transmitted to Es formation mechanisms, potentially through modulation of vertically propagating atmospheric tides that alter lower thermospheric wind shears".

The African longitude sector is underexplored despite its significant electrodynamic forcing and susceptibility to scintillation. Furthermore, most research concentrates on moderate ENSO events, inadequately quantifying responses to extreme El Niño and La Niña episodes. Different ENSO event strengths yield distinct tidal and electrodynamic responses, resulting in plasma instability variations, TEC crest location shifts, and scintillation changes.

The scarcity of African-focused, multi-ENSO-cycle analyses signifies a critical gap in space-climate coupling research. This study aims to fill this gap by investigating ENSO-phase-dependent TEC and atmospheric temperature variations in equatorial Africa under controlled solar and geomagnetic conditions.

Baldwin et al. (2001) and Lieberman et al. (2007) have found that the variability of tides in the mesosphere and lower thermosphere (MLT) is influenced by seasonal and interannual variations in these tidal sources, as well as the background wind fields of the middle atmosphere. Of particular interest are changes related to the quasi-biennial oscillation (QBO) of the middle atmosphere. The atmospheric tides that dominate the mesosphere and lower thermosphere (MLT) wind fields are excited by water vapor heating and latent heat release in the troposphere, as well as ozone heating in the stratosphere. Additionally, the El Niño–Southern Oscillation (ENSO) modifies tropospheric convective activity.

Sun et al. (2013), Liu et al. (2006), Liu et al. (2011), and Chou et al. (2017) all studied the ionosphere's reaction towards natural events like solar storms, eclipses, earthquakes, typhoons, etc. by using the dense ground-based global navigation satellite systems (GNSS), which have seen technological improvements and also improvements in numbers. The reactions of the ionosphere towards the events mentioned above are a result of the high resolution of the GNSS, both in space (less than 1˚ in both latitude and longitude) and in time (30s). GNSS TEC observation data have been compiled into a Global Ionospheric Map (GIM) to monitor global ionospheric weather and climate (Sun, 2019). Das and Pan (2016), Sun et al. (2018) soundings of Radio Occultation (RO) were used to record the changes in stratospheric temperature during the 2009 July 29 total eclipse, the El Niño Southern Oscillation effect on the quasi-biennial oscillation (QBO) from the stratosphere to the ionosphere. Sun et al. (2019) agree that severe weather or climate activities cannot only influence the troposphere but may also modulate the upper atmosphere, especially when Nishioka et al. (2013) showed that an enhanced Fujita scale 5 tornado happened in Moore, Oklahoma, on May 20, 2013 affected the concentric waves and short-period oscillations in North America. Apart from Nishioka, Song et al. (2017) also reported that typhoons Rammasum and Matmo in southern China caused ionospheric disturbances, which were detected by the ground-based GNSS TEC detection.

Newman et al. (2016) reported an anomalous upward displacement of the westerly phase, when normally, the quasi-biennial oscillation shows a downward displacement of the westerly phase. The phase moved from 30 hPa to 15 hPa pressure levels during the 2015/2016 El Niño Southern Oscillation warm phase. During ENSO 2015/2016, the F3/C RO temperature recorded the sudden disturbances in the QBO, which is averaged ±5˚ N latitude at each pressure level. Das and Pan (2016), Sun et al. (2018) have shown that during ENSO warm phases, the QBO period can be shortened not only in the stratosphere but can be done in the mesosphere and lower thermosphere (MLT) region. This happens due to the interaction between the broadband atmospheric waves, tides, and the background wind field. In this work, we are to investigate the potential trends in the ionosphere due ENSO effect, as the story of ENSO's effect on ionospheric scintillation isn't that clear.

Despite Africa's pivotal geographical positioning along the magnetic equator and within the Equatorial Ionization Anomaly, the corpus of ionospheric research conducted across the continent remains markedly deficient, with a mere handful of seminal and contemporary studies accessible. Pioneering investigations conducted by Skinner (1966) in Ibadan and Olatunji (1967) in Zaria delineated foundational Total Electron Content (TEC) characteristics pertinent to West Africa, whereas subsequent inquiries by Bolaji et al. (2012) and Essien et al. (2018) have enhanced the comprehension of regional scintillation phenomena. Nonetheless, comprehensive examinations addressing climate–ionosphere interactions within African longitudinal sectors remain predominantly absent, notwithstanding the continent's distinctive convective dynamics, land–ocean thermal disparities, and singular geomagnetic conditions shaped by the South Atlantic Anomaly. This deficiency is becoming increasingly pressing as Africa's reliance on satellite-dependent systems for aviation, telecommunications, and precision agriculture escalates, thereby rendering a deeper understanding of regional ionospheric variability imperative for both scientific inquiry and practical implementation.

2.5 Greenhouse Gas Trends and Upper Atmospheric Cooling

Literature suggests that elevated greenhouse gas concentrations notably influence the thermal dynamics of the upper atmosphere via thermospheric radiative cooling. In contrast to their warming effects in the troposphere, these gases facilitate infrared emission in the thermosphere, resulting in augmented heat dissipation into space and a sustained decrease in neutral temperature and density at ionospheric altitudes (Qian et al., 2011).

Thermospheric cooling has a direct impact on ionospheric behavior through alterations in:

1. Neutral scale height,
2. Molecular diffusion rates,
3. Ion–neutral collision frequencies,
4. Recombination coefficients.

The dynamics of ionospheric plasma are significantly governed by ion–neutral interactions, which can be articulated through the ion momentum equation described by Equation 2.12:

$$m_i \frac{dv_i}{dt} = q(E + v_i \times B) - m_i \nu_{in}(v_i - v_n) \qquad (2.12)$$

where

$\vec{v}_i$= ion velocity,

$\vec{v}_n$= neutral wind velocity,

ν_{in}= ion–neutral collision frequency,

$\vec{E}$= electric field,

$\vec{B}$= geomagnetic field.

A decrease in thermospheric temperature from greenhouse gases results in reduced scale height and altered neutral wind patterns, affecting dynamo electric fields and plasma transport. Long-term modeling indicates that increased CO_2 levels consistently lower the F-region peak height and electron density under stable solar conditions, leading to a gradual, climate-induced modulation of ionospheric TEC independent of short-term solar and geomagnetic changes (Jarvis et al., 1998).

This mechanism is under-researched in Africa and tropical areas due to limited long-term upper-atmospheric data. Africa's location near the geomagnetic equator suggests that thermospheric cooling may intensify due to variations in equatorial plasma drifts and recombination rates. This underscores the necessity of integrating greenhouse gas influences into climate-ionosphere coupling research in the African context.

CHAPTER THREE

3. METHODOLOGY

3.1 Study area

Shenvi and Virani (2023), in their research, divided the latitude into three main regions using the geographical coordinates. These divisions are: higher latitude (any angle above 60˚ either in the northern or southern hemispheres), mid-latitude, ranging from x: 30˚ < x < 60˚ in the northern or southern hemispheres, and the lower latitude, which can also be called the equatorial region, ranges from 0˚ to 30˚, as Figure 3.1 illustrates.

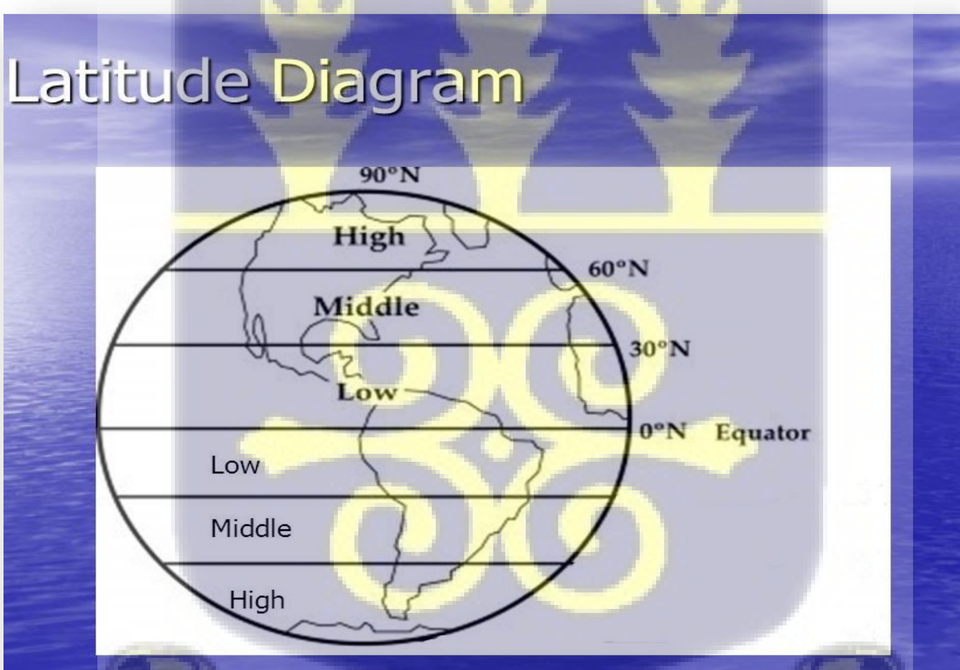

Figure 3.1: Latitudinal Zones (https://slideplayer.com/slide/4183329)

The three-station configuration facilitates significant latitudinal comparisons, allowing for the differentiation of location-specific effects from global influences. This differentiation is crucial due to the variability of ENSO impacts and ionospheric responses across latitudes. Thus, the study examines the influence of tropospheric climate conditions on ionospheric scintillation by analyzing data from three globally situated stations, each monitored by 32 GNSS satellites. Figure 3.2 illustrates their geographical distribution, while Table 3.1 presents their respective latitudinal coordinates and regional classifications.

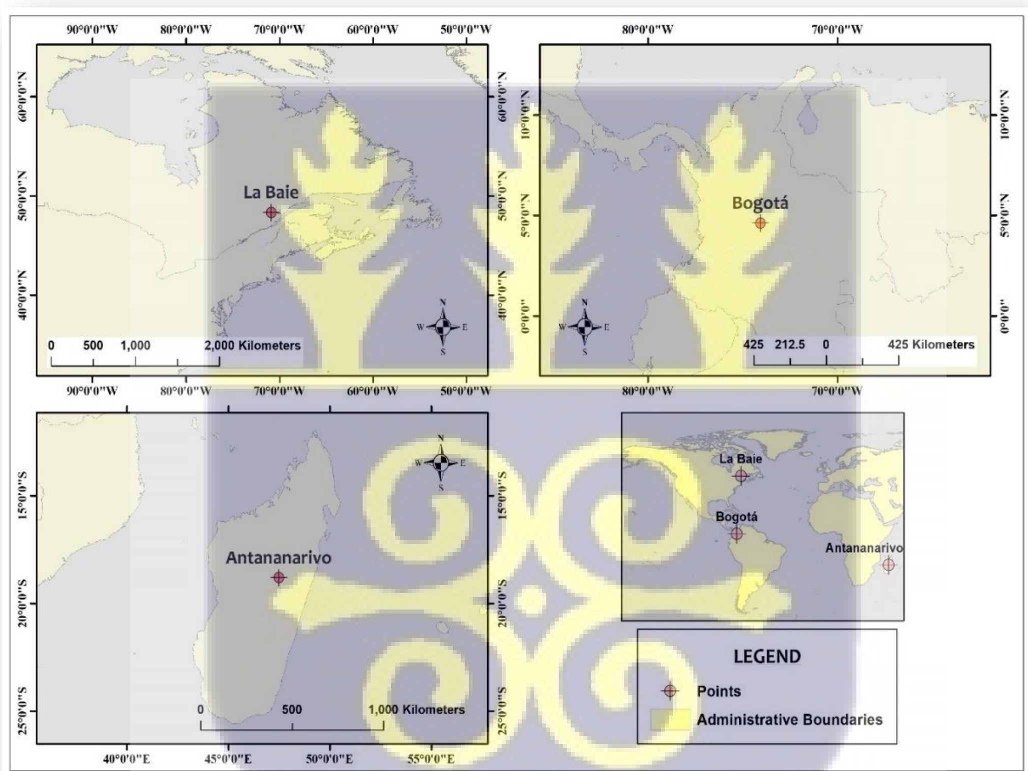

Figure 3.2: Geographical boundaries of the regions of study

Table 3.1: Study areas and their latitudes

Location of GNSS Satellites	Geographic Latitude / (˚)	Geomagnetic Latitude / (˚)	Latitude Region
Antananarivo (Madagascar)	18.91 ˚ S	15.42 ˚S	Lower-latitude
Baie-Comeau (Canada)	49.367 ˚ N	51.23 ˚N	Mid-latitude
Bogota (Colombia)	4.711 ˚ N	7.61 ˚N	Lower-latitude

Canada is predominantly a high-latitude region, with certain areas like Baie-Comeau situated in the mid-latitudes. The three selected stations for this study were determined based on data access, geographical representation, and unique climatic traits. While Africa's climate is generally characterized by a dichotomy of rainy and dry seasons, most continents observe a quadripartite seasonal cycle: summer, autumn, winter, and spring. Antananarivo in Madagascar exemplifies this, featuring a cool, dry period from May to October and a warm, rainy period from November to April (World Bank Climate Change Knowledge Portal, 2021).

Romero-Hernandez et al. (2020) assert that the Earth's magnetic field exhibits reduced intensity at the equator compared to the poles. An exception is the South Atlantic Anomaly (SAA), where the geomagnetic field approaches the Earth's surface, leading to increased ionospheric variability. These areas are subject to frequent fluctuations in electron density due to ENSO-induced temperature changes, solar activity, and geomagnetic anomalies. Rohde (2024) indicates that ENSO events can temporarily influence global climatic patterns, as evidenced by the significant La Niña of 2011 and the pronounced El Niño of 2015–2016, both of which resulted in considerable global temperature deviations (The Global Climate 2011–2015 Report, 2016).

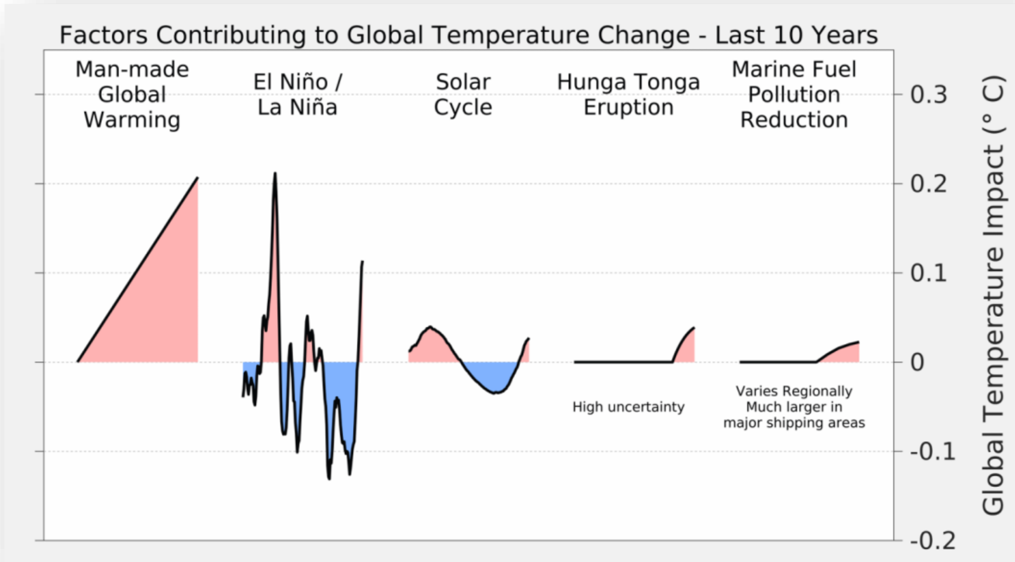

Figure 3.3: ENSO's contribution to global temperature average (Berkeley Earth)

During ENSO seasons, strong warmth anomalies are visible, especially in the tropical Pacific, and according to the National Oceanic and Atmospheric Administration's (NOAA) monthly global report for 2011, average global temperatures in 2011 were 14.52˚C or 58.14˚F, and it's seen as the warmest La Niña year ever in history. Figure 3.3 shows clearly that ENSO contributes an average of 0.2˚C during ENSO years.

The selected locations, which have different latitudinal locations, may have differences in TEC values as scintillation and TEC values are affected by geographical and geomagnetic latitudes, as agreed by Romero-Hernandez et al (2020). Low-latitude atmospheric scintillation and TEC studies have been done in different countries in Africa, like Skinner in 1966 at Ibadan and Olatunji in 1967 at Zaria, using the data of 1962–1963 and 1964–1965, respectively (Bolaji et al., 2012). Also in

South America, the city of Huancayo, with latitude and longitude coordinates 11.21°S, 75.41°W in Peru, had its TEC variation study done by Ross in 1966, and it was seen that the semiannual variation happens during the daytime. India, in the Asian continent and a lower-latitude country, had their TEC research conducted, and the conclusion was not far from what had earlier been seen by other atmospheric researchers in the other continents, that is, TEC values peak during daytime and minimize during the early minutes of sunrise. This research is to confirm if TEC values are latitudinally dependent and, for that matter, climate characteristics are important in the variation of ionospheric electron density.

3.2 Data sources

3.2.1 El Niño Southern Oscillation (ENSO) data

La Niña and El Niño cause weather and climate pattern anomalies worldwide, especially during the strong ENSO activities. Predicting the outcome and impact of ENSO activities is mostly not easy due to the dynamic and intricate nature of the Earth's atmosphere. To measure the ENSO index, the National Oceanic and Atmospheric Administration has developed a system known as the Oceanic Niño Index (ONI), which helps in classifying the various types of La Niña and El Niño events.

The Oceanic Niño Index (ONI) records the differences between the average sea surface temperature and the current sea surface temperature, which we normally call it sea surface temperature (SST) anomalies, which mostly happen in the eastern tropical Pacific (Niño 3.4 region). The measurement is done by using a three-month running average SST anomaly for the current month to the previous two months (Jan, 2024). According to Becker (2023), the winter of

2020/21 El Niño event is recorded as the strongest in history with an ONI anomaly of 2.6˚C as compared to other strong events like 1997/98, which had an ONI anomaly of 2.4˚C, and the 1982/83 winter El Niño ONI anomaly was 2.2˚C.

Jan (2024) groups the various ENSO activities into weak, moderate, strong, and very strong, especially El Niño events. These are as follows for El Niño events:

- Weak: +0.5°C to + 0.9°C anomaly
- Moderate: +1.0°C to +1.4°C anomaly
- Strong: +1.5°C to +1.9°C anomaly
- Very Strong: +2.0°C or higher anomaly

For La Niña events:

- Weak: anything below -1.0°C anomaly
- Moderate: -1.0°C to -1.49°C anomaly
- Strong: -1.5°C to -2.0˚C anomaly

The years chosen for the research are the 2020/21 La Niña year and 2023/24 El Niño year, which fall under strong ENSO activity years.

3.2.2 The Global Position System (GPS) satellite data

The beginning of space physics gave birth to the invention of Global Navigation Satellite Systems (GNSS), which was purposed for positioning and navigation reasons. As technology improves, the functions of GNSS have been expanded to perform precise timing synchronization for many different applications, creating of maps and providing geographical data, performing surveillance duties for public and private safety purposes, weather forecasting and monitoring atmospheric conditions, climate and environmental pattern studies, researching and studying the earth's atmosphere and ionosphere from a distance, etc. (Kumar, 2023). The emergence of smartphones has led to the insertion or installation of GNSS capabilities, making these smartphones perform the activities mentioned above. The GNSS is the mother of all satellite navigation systems (SNS) and their constellations like Galileo, Global Position System (GPS), or the NAVSTAR (NAVigation System Time and Ranging) developed by the Department of Defense in the United States in the year 1978, Russia's 'GLObalnaya NAvigatsionnaya Sputnikovaya Sistema' (GLONASS), etc. (Kumar et al., 2021). Officially, there are 195 countries in the world, but only a few of these countries (4) [United States, Russia, China, EU] host their own satellites through a specific satellite. The figure below shows the satellites hosted and the number of satellites available with the angle of inclination. The European Union (EU) hosts the Galileo satellite, while the Republic of China hosts the Beidou satellites.

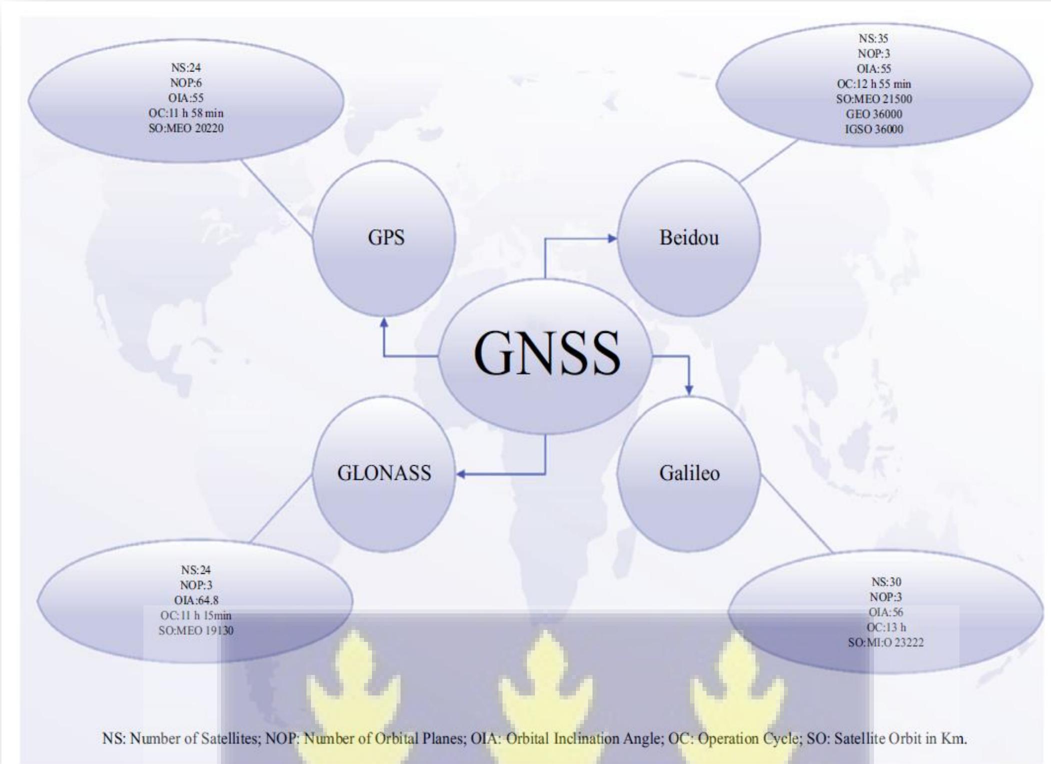

Figure 3.4: GNSS constellation systems. Adapted from Kumar, A., Kumar, S., Lal, P., Saikia, P., Srivastava, P. K., & Petropoulos, G. P. (2021). Introduction to GPS/GNSS technology. In Elsevier eBooks (pp. 11). https://doi.org/10.1016/b978-0-12-818617-6.00001-9

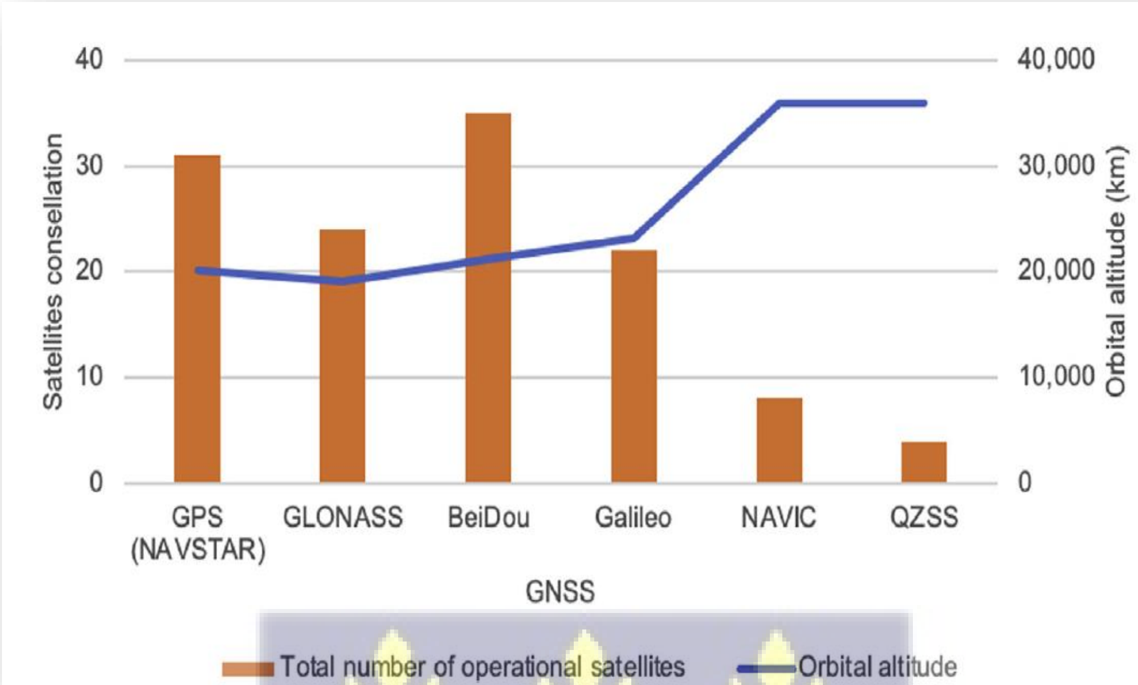

Figure 3.5: Satellite constellations and orbital altitude of major navigation systems. Adapted from Kumar, A., Kumar, S., Lal, P., Saikia, P., Srivastava, P. K., & Petropoulos, G. P. (2021). Introduction to GPS/GNSS technology. In Elsevier eBooks (pp. 11).

Figures 3.4 and 3.5 display the various satellites and their number of constellations, with the orbital altitude they can travel to. For example, taking the GPS which we worked with, it has about 32 constellations and can travel to about 30,000 km above the Earth's surface. It is therefore appropriate to use the GPS satellite to take our readings since the ionosphere has a height of 50 km to about 2000 Km above the surface of the earth.

This study uses data from the Global Position System (GPS) satellite positioned at various locations of our study of the ionosphere and takes readings from events that happen in the upper atmosphere. Some of the data taken are electron content (slant TEC), planetary disturbances (Kp or Dst), coronal mass ejections (CMEs), solar flares, sunspots, solar storms, etc. Kaplan and Hegarty (2017) said the global positioning system (GPS) satellite mainly comprises of three different segments, and these are: satellite constellation, ground control stations, and receivers. There is a receiver that all groups of institutions use to process the signals received from the satellite to determine the position, velocity, and time (PVT) anywhere in the world (El-Rabbany, 2006). According to Bolaji et al. (2012), GPS data provide an efficient way to estimate total electron content (TEC) with greater spacetime coverage. Before the GPS can transmit information or data, there are some basic binary codes, namely, pseudorandom noise (PRN) code, the precision (P) code, navigation code, and the coarse Acquisition (C/A) code, which it needs to employ (Wells & Beck, 1986). The GPS satellites broadcast two carrier waves, L1 and L2, at frequencies of 1575.42 MHz and 1227.60 MHz, respectively. L1 and L2 are modulated by the code information signal, which enables communication between the satellites and the receivers (Kumar et al., 2021). The dual frequency ($f_1 f_2$) GPS receiver system offers a means of measuring and knowing the effect of the ionosphere on GPS signals.

Ionospheric parameters display significant seasonal fluctuations influenced by solar zenith angle, atmospheric composition, and thermospheric dynamics. Therefore, the analysis employs equivalent seasonal periods (e.g., December-January-February in both La Niña and El Niño) instead of annual averages. This methodology differentiates ENSO-related variations from typical seasonal patterns. In our study to know the patterns of the ionosphere and whether the tropospheric climate variables like El Niño and La Niña do impact it, we need scintillation data (VTEC), planetary index data (Kp), solar flare effect (SFE) data, disturbance storm time (Dst) data, and temperature profile data from the troposphere to the ionosphere. These data will enable us to know whether the patterns of the ionosphere are especially during the ENSO events. Solar activities like solar substorms, geomagnetic storms, solar flares, CMEs, etc., affect the electron content of the ionosphere, and to have a firm conclusion of climate variables' influence on the ionosphere, the ionosphere should be free from solar activities or should be at a minimum level.

In this study, the main parameter we are considering is climate and how climate variability impacts the ionosphere. Solar activities also affect the patterns of the ionosphere, and for that matter, solar activities were considered in this research. Geomagnetic storm data, like planetary geomagnetic index, Kp, and disturbance storm time, Dst, were considered in addition to the effect of solar flare on the ionosphere. All this available data is received through the readings and recordings of the GPS satellites positioned in the various locations of study.

3.2.2.1 Solar activity indices

The sun's non-static magnetic field, which is very powerful and protects the atmosphere from solar activities like solar flares, sunspots, coronal mass ejections, solar storms, etc. (Tal, 2024). Studying and analyzing these solar activity events enables upper atmospheric and cosmological scientists to know the rate at which these activities impact our planet, Earth, and other communication and navigational objects in space. Gulyaeva (1999), Jakowski et al. (2006), and Shenvi and Virani (2023) agree that local time, seasons, and solar cycles, as well as geomagnetic activities, are key parameters that influence the arrangement and concentration of the electron density in the ionosphere. The solar factors are solar radio flux [F10.7] and sunspot number [SSN], and solar flare effect [SFE], while the geomagnetic activity parameters are the planetary index [Kp and Ap] and the disturbance storm time [Dst] index.

In this research, we used the solar flare effect, the Kp, and Dst to study the variations of the ionosphere in 2020/21 and 2023/24 ENSO years. Mendillo (2006), Bagiya et al. (2009) have proven that at high solar activities, TEC values increase whiles at low solar activities, TEC values decrease using the examples of sunspots, and magnetic storms like the geomagnetic storm. Gonzalez et al. (1999) also showed that when solar storms weaken the Earth's magnetic field, the consequences are that Dst values become negative. Shenvi and Virani (2023) also confirmed with their long short-term memory (LSTM) model that before solar storm events, the rate of increase in the total electron content (TEC) was gradual, but during the main event of a solar storm, there was a sudden decrease in the rate of TEC growth. The disturbance storm time (Dst) index, which is one of the parameters we used to determine the quiet and stormy days of 2020/21 and 2023/24. Dst index compares the magnetic field of the Earth during storm days against its normal daily variation on a quiet day. Based on Gonzalez et al. (1994) and Saba et al. (1994), the disturbance storm time (Dst) index is a good indicator and can categorize geomagnetic storms into:

- Dst > -30nT shows a quiet day.
- -50 nT < Dst ≤ -30 nT shows a weak storm.
- -100 nT < Dst ≤ -50 nT shows a moderate storm.
- -250 nT < Dst ≤ -100 nT indicates an intense storm.
- Dst ≤ -250nT indicates a very intense storm.

The data for the disturbance storm time for the 2020/2021 and 2023/2024 ENSO years were downloaded from the website of the World Data Center (WDC) for Geomagnetism (Kyoto) website (https://wdc.kugi.kyoto-u.ac.jp/dstae/index.html). The data set has been converted to the format of the International Service of Geomagnetic Indices 2002 (ISGI – 2002) with a station name as Equatorial Dst Index. The International Association of Geomagnetism and Aeronomy (IAGA) code is Dst, with a time interval of 1 hour. The WDC Dst data contains the date of the event, time of measurement, day of the year (d.o.y), and Dst index, and these can be seen in Figure 3.6.

```
 Format                 IAGA-2002
 Source of Data         WDC for Geomagnetism, Kyoto, Japan
 Station Name           Equatorial Dst index
 IAGA CODE              Dst
 Geodetic Latitude
 Geodetic Longitude
 Elevation
 Reported               Dst
 Sensor Orientation
 Digital Sampling
 Data Interval Type     1-hour
 Data Type              Definitive
 # Converted to IAGA2002 format by the International Service of
 #  Geomagnetic indices (ISGI, https://isgi.unistra.fr).
 # The values in the raw of 00:00:00.000 are the mean values
 #  between 00:00UT and 01:00UT, etc.
 # Missing values are indicated by value 9999
 # Dst: Disturbed Storm Time, unit 1 nT
 #
 # DOI citation:  https://dx.doi.org/10.17593/14515-74000
 #
 # For more information on Dst index, please visit
 #  World Data Center for Geomagnetism (Kyoto) website:
 #  https://wdc.kugi.kyoto-u.ac.jp/dstdir/
DATE       TIME         DOY     Dst
2015-01-01 00:00:00.000 001     -18
2015-01-01 01:00:00.000 001     -18
2015-01-01 02:00:00.000 001     -20
2015-01-01 03:00:00.000 001     -20
2015-01-01 04:00:00.000 001     -19
2015-01-01 05:00:00.000 001     -20
2015-01-01 06:00:00.000 001     -19
2015-01-01 07:00:00.000 001     -16
2015-01-01 08:00:00.000 001     -15
2015-01-01 09:00:00.000 001     -13
2015-01-01 10:00:00.000 001     -11
2015-01-01 11:00:00.000 001      -9
2015-01-01 12:00:00.000 001      -4
2015-01-01 13:00:00.000 001       0
2015-01-01 14:00:00.000 001       2
2015-01-01 15:00:00.000 001       1
2015-01-01 16:00:00.000 001      -2
2015-01-01 17:00:00.000 001      -3
2015-01-01 18:00:00.000 001      -4
```

Figure 3.6: Screenshot of Dst readings

Another solar storm parameter used in this work is the planetary index, Kp, which was also derived from the International GNSS Service (IGS) satellite. The National Oceanic and Atmospheric Administration (NOAA) Space Weather Prediction Center (SWPC) website, planetary index (Kp), is an indicator of geomagnetic activity, and it is derived by calculating a weighted average of the planetary (k) indices from an already determined network of geomagnetic observatories. The highest fluctuations observed on a magnetometer in relation to a quiet day, over a three-hour interval, are what we call the Kp. According to Tal (2024), the Kp index quantifies the disturbances in the horizontal component of Earth. Table 3.2 shows the Kp index and its effect on the ionosphere.

Table 3.1: Planetary Index (Kp) and its impact on the ionosphere.

Planetary index (Kp)	**Kp effect**	**Description**
0	Quiet	Aurora oval mostly to the north of Iceland. Faint aurorae visible in photographs, low in the northern sky.
1	Quiet	Aurora oval over Iceland, faint and quiet aurorae observable to the unassisted eye, low in the northern sky.
2	Quiet	There is dynamism in the aurora, visible and bright.
3	Unsettled	Bright auroras are visible at zenith. Pale green color is more noticeable.
4	Active	Bright, constant, and dynamic northern lights are visible. More colors start to appear.

5	Minor storm	Bright, constant, and colorful aurora display, with red and purple colors appearing. Aurora coronae likely.
6	Moderate storm	Bright, dynamic, and colorful aurora display. Aurora coronae likely. Memorable to those who witness them.
7	Strong storm	Bright, dynamic, and colorful aurorae. Visible in the southern sky. Aurora coronae is very likely.
8	Severe storm	Bright, dynamic, and colorful aurorae. Aurora is seen around 50° latitude.
9	Intense storm	Aurorae are seen around 40° latitude. Red aurorae and coronae are very likely. Most often caused by powerful coronal mass ejections.

The planetary index (Kp) data for the 2020/2021 and 2023/2024 ENSO years were taken from the website of the World Data Center (WDC) for Geomagnetism (Kyoto) website (https://wdc.kugi.kyoto-u.ac.jp/dstae/index.html). The data set has been converted to the format of the International Service of Geomagnetic Indices (ISGI, https://isgi.unistra.fr) with a station name as the Kp Index. IAGA code is Kp with a data time interval of 3-hour readings. The WDC Kp data contains the date of the event, time of reading, day of the year (d.o.y), Kp, Ap, ap, Cp, C9, BSRN, and NdB. Explanations to these indices are shown below, and a screenshot of the readings is shown in Figure 3.7.

- Kp: Planetary three-hour-range index expressed in a scale of thirds; it ranges from Oo to 9o.
- ap: represents a Kp-value converted back to a linear scale in nT. It ranges from 0 to 400 nT.
- Ap: arithmetic mean of the day's eight Ap values, unit 1 nT.
- Cp: Planetary daily character figure It ranges from 0(quiet) to 2.5 (disturbed) in steps of 0.1.
- C9: Conversion of the 0 to 2.5 range of Cp index to one digit between 0 and 9. BSRN: Bartels solar rotation number - a sequence of 27-day intervals counted continuously from February 8, 1832
- NdB: Number of days within the Bartels 27-day cycle.

```
Format                      IAGA-2002
Source of Data              GFZ, Helmholtz-Zentrum Postdam, Germany
Station Name                Kp index
IAGA CODE                   Kp
Geodetic Latitude
Geodetic Longitude
Elevation
Reported                    Kp, ap, Ap, Cp, C9 and related values
Sensor Orientation
Digital Sampling
Data Interval Type          3-hours
Data Type                   Definitive
# Converted to IAGA2002 format by the International Service of
#  Geomagnetic indices (ISGI, https://isgi.unistra.fr).
# The values in the raw of 00:00:00.000 are the mean values
#  between 00:00UT and 03:00UT, etc.
# Kp: Planetary three-hour-range index
#     Expressed in a scale of thirds, it ranges from 0o to 9o
# ap: represents a Kp-value converted back to a linear scale in nT
#     It ranges from 0 to 400 nT
# Ap: arithmetic mean of the day's eight ap values, unit 1 nT
# Cp: Planetary daily character figure
#     It ranges from 0(quiet) to 2.5 (disturbed) in steps of 0.1
# C9: Conversion of the 0 to 2.5 range of Cp index to one digit
#     between 0 and 9
# BSRN: Bartels solar rotation number - a sequence of 27-day
#     intervals counted continuously from February 8, 1832
# NdB: Number of day within the Bartels 27-day cycle
#
# DOI citation:  https://doi.org/10.5880/Kp.0001
# License: CC BY
#          https://creativecommons.org/licenses/by/4.0/
#
# For more information on Kp and related indices, please visit
#  GFZ "Indices of Global Geomagnetic Activity" service website:
#  https://www.gfz-potsdam.de/Kp-index/
DATE       TIME         DOY Kp  ap    Ap  Cp  C9  BSRN  NdB
2023-06-01 00:00:00.000 152 4-  22    12 0.7  3   2588   27
2023-06-01 03:00:00.000 152 2+   9    12 0.7  3   2588   27
2023-06-01 06:00:00.000 152 4-  22    12 0.7  3   2588   27
2023-06-01 09:00:00.000 152 2o   7    12 0.7  3   2588   27
2023-06-01 12:00:00.000 152 3o  15    12 0.7  3   2588   27
```

Figure 3.7: Screenshot of 2023/24 Kp index readings

Concluding on the last parameter, which impacts the ionosphere and TEC concentration in relation to the study, is the solar flare effect (SFE). Buzás et al. (2023) in their study of the effect of solar flares used the amplitude or sales-absorption method, the f_{min} method, and the signal-to-noise (SNR) ratio, which was calculated from the amplitude data received. Sumod and Pant (2019) experimental research at Trivandrum, India, of magnetic latitude 8.5° N, 77° E, 0.5° N used 1 min high cadence data of thermospheric OI 630.0 nm dayglow, which was obtained from the multiwavelength dayglow photometer (MWDPM). Their conclusion confirmed earlier studies on solar flares having a much greater impact on the ionosphere and the electron content in this region of the atmosphere.

With this evidence of the important role of solar flare effect on the ionosphere, it is imperative to know the SFE of the years chosen for our study. The solar flare data were taken from the website of the International Service of Geomagnetic Indices (https://isgi.unistra.fr/events_sfe.php).

Buzás et al. (2023) grouped the levels of solar flare effect into X, M, and C, where X is considered to be the most intense effect of solar flare, ranging from X > 10^{-4} W/m^2. M means medium effect, which is within a range of ~10^{-5} W/m^2 to 10^{-4} W/m^{2,} and the smaller effect or less effect, C has a range of ~10^{-6} W/m^2 to 10^{-5} W/m^2. All these are based on the level of the 0.1 nm – 0.8 nm X-rays released by the flux and measured by the Geostationary Operational Environmental Satellite (GOES) which the flare mostly happens for just 1 h or below. With the ISGI data, the flare is classified into three different levels, and they are 1, 2, and 3. These numbers have their meaning concerning the effect of solar flares, and they are as follows:

- 1: Doubtful solar flare effect (SFE).
- 2: The shape and extension of the phenomenon correspond to an SFE.
- 3: The shape and extension of the phenomenon correspond to a notable SFE.

The ISGI used the International Association of Geomagnetic and Aeronomy format (IAGA) 2002. The source of the ISGI data is the Ebre Observatory, Spain, with the station name being solar flare effect (SFE) and the IAGA code as SFE. The data were converted to the IAGA 2002 format by the International Service of Geomagnetic Indices (ISGI, https://isgi.unistra.fr). Figure 3.8 displays a screenshot of ISGI SFE readings with other attributes of the data.

```
Format                      IAGA-2002
Source of Data              Ebre Observatory (Spain)
Station Name                Solar Flare Effects
IAGA CODE                   SFE
Geodetic Latitude
Geodetic Longitude
Elevation
Reported                    various informations about SFE events
Sensor Orientation
Digital Sampling
Data Interval Type          depending of the number of events
Data Type                   Definitive
# Converted to IAGA2002 format by the International Service of
#  Geomagnetic indices (ISGI, https://isgi.unistra.fr)
# QUA : SFE "qualification" meaning
#    1: Doubtful SFE
#    2: The shape and extension of the phenomenon
#       correspond to a SFE
#    3: The shape and extension of the phenomenon
#       correspond to a notable SFE
# OBSERVATORIES : Code of observatories reporting SFE
#
# License: CC BY-NC
#          https://creativecommons.org/licenses/by-nc/4.0/
#
# For more informations on SFE events, please visit the
#  International Service on Rapid Magnetic Variations of Ebre
#  Observatory :
#  https://www.obsebre.es/en/rapid
DATE       TIME         DOY  QUA  OBSERVATORIES
2011-01-28 00:44:00.000 028   2   MMB KAK KNY
2011-02-09 01:28:00.000 040   2   MMB KAK KNY GNA CNB
2011-02-15 01:48:00.000 046   3   MMB KAK KNY GNA
2011-02-16 14:22:00.000 047   2   LER ESK HAD
2011-02-28 12:43:00.000 059   2   LER ESK HAD GUI
2011-03-09 23:19:00.000 068   2   MMB KAK KNY
2011-06-07 06:18:00.000 158   1   MMB KAK KNY
2011-07-30 02:07:00.000 211   1   MMB KAK KNY
2011-08-03 04:30:00.000 215   2   MMB KAK KNY GNA CNB
2011-08-04 03:44:00.000 216   2   MMB KAK KNY GNA CNB
2011-08-09 08:01:00.000 221   3   BDV MMB EBR KAK KNY
2011-09-06 01:42:00.000 249   1   MMB KAK KNY
2011-09-06 22:16:00.000 249   3   MMB KAK KNY
2011-09-07 22:34:00.000 250   3   MMB KNY GNA CNB
```

Figure 3.8: Screenshot of SFE

3.2.2.2 Data Processing and Quality Control Procedures

Temporal Resolution and Data Availability: GNSS-TEC data were collected at 30-second intervals and averaged to 1-hour intervals to minimize noise while maintaining relevant variations for climate studies. The 1-hour resolution effectively balances smoothing with the detection of climate-driven variations occurring over days to weeks. Data availability varied by station due to outages and visibility constraints, with Antananarivo at 92%, Baie-Comeau at 88%, and Bogotá at 94%. Days with less than 75% data completeness were excluded to prevent sampling bias.

Handling Missing Data: Short gaps were filled via linear interpolation to ensure continuity in diurnal analysis, while longer gaps were excluded from analyses requiring full coverage to avoid bias from artificial patterns during rapidly changing ionospheric conditions.

Bias Correction and Calibration: Systematic offsets from DCBs were corrected using monthly values from CODE, following the standard procedure, which adjusts observed STEC by subtracting satellite and receiver biases before VTEC conversion. The accuracy of corrected TEC is estimated at ±2 TECU, aligning with independent ionosonde measurements and sufficient for observing ENSO-related variations typically between 5-10 TECU in equatorial regions.

Latitudinal Variation Handling: Unique ionospheric phenomena at equatorial stations necessitate the use of geomagnetic coordinates for TEC analysis, as they better represent ionospheric physics. For example, Antananarivo's geomagnetic latitude of 15.42°S is more relevant than its geographic latitude.

The VTEC conversion utilizes a 350 km ionospheric shell height, appropriate for the F2-layer, with sensitivity analyses indicating that variations in shell height contribute less than ±1 TECU to final VTEC values, remaining within acceptable error margins for this study.

3.3 Extraction of solar activity data

These described data (Kp, Dst, and SFE), which cause scintillation in the ionosphere, are being extracted from the World Data Center for Geomagnetism, Kyoto (WDC) websites https://wdc.kugi.kyoto-u.ac.jp/wdc/Sec3.html and the International Service of Geomagnetic Indices (ISGI) website, https://isgi.unistra.fr/data_download.php. The WDC and ISGI combined provide a dataset for most of the solar activities, especially the data needed for this research. Some of the available datasets that can be downloaded or extracted from these websites, apart from what had been earlier mentioned are Auroral Electrojet (AE) index, Longitudinally Asymmetric (ASY) and Symmetric (SYM) disturbance index, International Quiet (Q) and Disturbed (D) days index, Sudden Commencement (SC), Polar Cap (PC), etc. These websites provide maps and graphs for the various datasets, which we shall use in our next chapter as we discuss the results of the processed data. The following procedures were used in the extraction of any of the datasets we have discussed in this chapter.

1. For the ISGI website, click on "data download" on the geomagnetic icon.
2. Select from the lists of available data types provided the type of data (Dst, Kp, etc.) you want to extract or download for the work.
3. On the same page, fill the spaces provided under the data range. The data range gives you the opportunity to select a period of data from the dataset that you need for the research.
4. Input your email in the space provided below and click on the "download data" icon.
5. A zip file will be downloaded. Extract the information from the zip file and open it with an appropriate software application like Notepad, Notepad++, etc.

The procedures involved in the extraction of information from the website of the World Data Center for Geomagnetism are simple. The disadvantage of this site is that it doesn't have the dataset for Solar Flare Effect (SFE). The processes are listed below:

1. On the homepage of the WDC website, click on the data service option and select the type of data you want.

2. Fill the portion labelled “start year” and “end year”. A maximum duration of 25 years is allowed.
3. On the same page, an option of data format is given for selection. The International Association of Geomagnetism and Aeronomy format is mostly used as it is the standard for geomagnetic activity indices.
4. Click on submit to be able to read your output information.

3.4 Extraction and analysis of GPS Total Electron Content (TEC) data

Nishioka et al. (2021) derived their TEC data from the GNSS Earth Observation Network (GEONET) satellite, which had been archived by the National Institute of Information and Communications Technology (NICT) in the year 1997. Among the specific information the data took are the slant TEC (STEC) from the pseudo-range and carrier-phase measurements, which were done by a dual frequency GEONET satellite. The GPS receiver and the Canadian Advanced Digital Ionosonde (CADI) deployed in Dibrugarh with geographic latitude 27.5˚ N, 95˚ E, 43˚dip recorded slant TEC (STEC) and ionogram information in the other ascendant and maximum circumstances (Kalita & Bhuyan, 2017). According to NOAA's National Weather Service, 2020, this was carried out during solar cycle 24, which began in January 2008 and finished in December 2019. To study the ionospheric phenomena in the low- and middle-latitude transition area near the crest of the longitudinal WN4 structure at 90˚ to 100˚ E, Kalita and Bhuyan (2017) collected TEC data and ionograms from ten (10) of the quietest days between July 2010 and October 2015.

The two GPS Ionospheric Scintillation TEC Monitor (GISTM) receivers utilized by Alfonsi et al. (2011) were situated in the Vietnamese cities of Hoc Mon, which lies near the magnetic equator, and Hue, which is close to the northern crest of the equatorial anomaly. The GISTM used NovAtel OEM4 to compute amplitude and phase scintillation data. The data was analyzed using the multi-instrument data analysis system (MIDAS). Jiao et al. (2013) used a dual-frequency GSV4004B ISM receiver from GPS Silicon Valley to capture scintillation data and create scintillation event outputs. The GSV4004B's L1 monitors 50 Hz phase and amplitude, while the L2 records 1 Hz phase, pseudo-range, and carrier-to-noise (C/No) data. Singh et al. (2019) employed dual-frequency satellite GPS NovAtel TEC data, with the receiver deployed at India Permanent Research Base "Maitri", Antarctica (70˚ 46' 00" S, 11˚ 43' 56" E).

The GPS receiver used recorded the slant TEC (STEC) data with a high resolution of 1 min and measured the TEC using the pseudo-range measurements on L1 and L2 frequencies. To calculate the phase scintillation index (σ_φ) and the amplitude scintillation index (S_4), the Canadian High Arctic Ionospheric Network (CHAIN) and the Canadian Advanced Digital Ionosondes (CADI) were placed on the polar cap and auroral oval using GISTM GSV4004B and NovAtel OEM4. The Madrigal database, located at MIT (Massachusetts Institute of Technology, USA), provided the TEC data that Prikryl et al. (2013) used in their study.

In this study, TEC data were taken from GNSS systems with dual frequency of NovAtel receivers situated at various stations and regions of the globe. The GNSS system provides an efficient way to estimate TEC values with spatial and temporal coverage (Bolaji et al., 2012). The estimation of the degree of ionization, which is also known as slant TEC or simply TEC, with the formula earlier stated in chapter two as Equation 2.1, is the integral of the electron density (N_e) along a path (slanted). Seemala (2011) estimated S4 (amplitude scintillation index) value, modified Julian date with fraction of day as time (Jdatet) records, the normal universal time (UT) records, the pseudo-random noise (PRN), a data for longitude and latitude with the azimuth angle of the satellite in degrees, and the vertical and slant TEC values recorded by the NovAtel receiver of the GPS satellites in the GPS-TEC analysis software application created by Dr. Gopi Krishna Seemala of the Indian Institute of Geomagnetism (IIG), Navi Mumbai, India. These datasets were recorded every 15.002 seconds and have been converted to one hour (1 h). The GPS–TEC application also has records on latitude and longitude, all in degrees, and the altitude is measured in units of meters. The ionospheric piercing point (IPP) is taken to be at an altitude of 350km. The STEC values must be converted to VTEC since the STEC values from the visible satellites are corrupted with satellite bias, also known as satellite differential delay (b_s), receiver differential delay or receiver bias (b_r), and then the receiver inter–channel bias (b_{rx}). The Gopi GPS – TEC analysis software has VTEC and STEC equations incorporated already into the TEC analysis application, which provide the STEC and VTEC information for a specific location and time. To reduce multipath effects, the program uses a minimum angle elevation of 20˚. The VTEC data is estimated and then related to a two sigma (2σ) iteration, giving a GPS point position accuracy of 95% confidence level, which is about 1.96 standard deviations. The outcome results are the average VTEC values over all pseudorandom numbers (PRNs) on a period of 24 hours (24 h) (Bolaji et al., 2015). The software produces about four different graphs, and they:

1. A graph of TEC units against time (UT) with biases (satellite and receiver) with a 20˚ elevation mask.

2. A graph of TEC units against time (UT) with biases (satellite and receiver) removed with an elevation mask of 20˚.
3. Individual graphs for the various pseudorandom noise (PRNs) with TEC units and amplitude scintillation (S4) index on both sides of the graphs against universal time (UT) on the horizontal axis.
4. A graph of TEC units against universal time (UT) with an elevation mask of 15˚.

These various outcomes will be discussed in the preceding chapter (results and discussions), where we looked at the various factors that affected the outcomes of the research. In this research, we want to study how climate variables affect the ionosphere, which directly affects traveling signals from the satellite in space to the receivers on the surface of the Earth. This can only be achieved when we know the state of the ionosphere, thus it has been an undisturbed or disturbed state (scintillation). To know this, we plotted a graph of VTEC values against universal time (UT). This graph will help us know the peak scintillation of the day. After plotting the VTEC against UT, we detrend the VTEC against UT graph to know whether the ionosphere was disturbed, and if it was disturbed, what may be the cause of the disturbance?

GNSS signals are affected by noise from other sources, and to measure scintillations effectively and accurately, a well-designed filter that can remove the unwanted trends and noise effectively should be used. These trends and variations or fluctuations may not be a contributing factor to ionospheric disturbances, and for that matter, we remove all the unwanted trends, seasonal variations, and daily fluctuations, which will help us to see the actual ionospheric disturbances (Osei-Poku et al., 2021). Detrending removes these unwanted trends, isolating the high–frequency fluctuations caused by diffractions, which is the true scintillation effect. To differentiate between small-scale and large-scale ionospheric irregularities, the Fresnel frequency (Ff) is used (Ghobadi et al., 2020). Any ionospheric irregularities higher or larger than the Fresnel scale cause a refractive effect on the ionospheric signal due to the ionosphere's varying refractive index. Ionospheric irregularities smaller than the Fresnel scale cause diffraction when crossed by a plane wave, creating an interference pattern received on the ground. To measure scintillation, scientists use phase scintillation indices based on the signal's phase variation. The Fresnel frequency scale (F_f) is described by Forte et al. (2017) as Equation 3.1:

$$\text{Fresnel frequency } (F_f) = \frac{V_{rel}}{\sqrt{2\lambda z}} \tag{3.1}$$

With Equation 3.1, V_{rel} is the relative velocity between the ionosphere and the GPS satellite, λ is the wavelength of the signal used, and z denotes the vertical distance between the ionosphere and the receiver, where z is mostly 350 km, which is the IPP. For z and V_{rel}, it changes with respect to location and periods of measurements, and for that matter, the Fresnel frequency has a cutoff of 0.1 Hz, which is a typical detrending method that uses this cutoff, such as the Butterworth filters (Prikryl et al., 2010).

There are other types of detrending methods, and these methods may change due to certain factors like the amount of solar activity present during the time of the research and the quality of TEC data available. Osei-Poku et al. (2021) listed two types of detrending methods, the Savitzky–Golay filter and polynomial filtering, which were evaluated during thunderstorm events in Hong Kong. Pradipta et al. (2015) also listed other methods of detrending, which are polynomial fit, moving average, and wavelet filtering in their work. Ghobadi et al. (2020) also said the Butterworth and the Cascaded High Pass Filters (CHPF) are based on classical time-frequency analysis, where they need a priori assumptions and the uncertainty principle being an obstacle, but there are other detrending techniques, such as the Ensemble Empirical Mode Decomposition (EEMD), Adaptive Local Iterative Filtering (ALIF), and fast iterative filtering (FIF). Gu and Zhou (2010) mentioned the detrended fluctuations analysis (DFA) as another type of detrending technique in addition to the already known detrending techniques such as moving average (MA) which later became detrended moving average (DMA) method is a classical method of time series decomposition which is simply implemented to evaluate the correlation properties of non-stationary series without any assumption, it is widely applied to the analysis of real-world time series and synthetic signals (Hyndman & Athanasopoulos, 2018; Şahbazoğlu, 2024; Gu & Zhou, 2010).

Essien et al. (2021) and Figueiredo et al. (2018) used the detrending moving average (DMA) formula, which helped in determining the fluctuations in TEC components. Although both DMA and wavelet analysis effectively distinguish ionospheric scintillation from background trends, this study favors DMA for its alignment to evaluate climate-driven ionospheric variability across ENSO phases. DMA offers a clear, single-scale detrended TEC series that is efficient, statistically compatible with climate analyses, and reproducible with a justified window length. In contrast to wavelet analysis, which involves subjective parameters and complex significance testing, DMA facilitates straightforward statistical comparison, robust quality control, and clear physical interpretation without sacrificing sensitivity. Given the minor differences found in comparative testing, DMA is deemed sufficient and more suitable for the study's aims.

Detrending TEC is calculated by subtracting a one-hour (1 h) running average from the original TEC time series (VTEC (t)), which is centered at ± 30 min. Mathematically, as described by Essien et al. (2021) in Equation 3.2;

$$dVTEC = vTEC - < vTEC\ (t \pm 30min) > \quad (3.2)$$

Equation 3.2 was deployed in calculating the abnormal trends in the propagation of signals from the satellites to their various receivers. These two graphs of VTEC against universal time (UT) and detrended VTEC (dVTEC) against universal time (UT) were analyzed and plotted by using a computer programming language called Python and its various libraries.

3.5 Temperature profile data

In chapter two, Figure 2.3 shows the temperature profile of the atmosphere, from the troposphere to the thermosphere and beyond. The temperature profile of the lower atmosphere is affected by tropospheric and stratospheric events. These events of the lower atmosphere also impact the temperature profile of the upper atmosphere due to the ubiquitous atmospheric gravity waves (AGWs), which influence traveling ionospheric disturbances (TIDs) (Tsuda, 2014; Nappo, 2012; Hines, 1960).

The temperature profile data were provided by the University Corporation for Atmospheric Research (UCAR) website (https://www.cosmic.ucar.edu/what-we-do/cosmic-2/data) and COSMIC Data Analysis and Archive Center (CDAAC), which has been available since 2019 October 1. Constellation Observing System for Meteorology, Ionosphere, and Climate (COSMIC) data has been grouped into two, thus COSMIC – 1 and COSMIC – 2 data, but our concentration will be on COSMIC – 2 data (https://www.cosmic.ucar.edu/what-we-do/cosmic-2/data). The COSMIC – 2 data contain the following files, which are grouped into levels, and they can be retrieved at (https://www.cosmic.ucar.edu/what-we-do/cosmic-2/data):

Level 0:

- Binary instrument data (https://data.cosmic.ucar.edu/gnss-ro/cosmic2/tools/).

Level 1a:

- Spacecraft attitude information, which is represented in leoAtt format.
- Precise orbit determination antenna tracking data in a podCrx/RINEX2 format.
- Radio occultation antenna tracking data, which comes in the opnGns format.

Level 1b:

- SP3 format of precise orbit determination solutions.
- Atmospheric excess phase, which is read in the conPhs format.
- Absolute total electron content (podTc2 format) (GLONASS from February 1, 2021 onwards)

Level 2:

- Atmospheric profiles as atmPrf (RO retrieval), wetPf2 (1D-var retrieval, same as wetPrf format), and BUFR formats.

The radio occultation (RO) atmospheric profile data, which is in the atmPrf format, is described by https://cdaac-www.cosmic.ucar.edu/cdaac/cgi_bin/fileFormats.cgi?type=atmPrf. The atmPrf format comes in the form:

PUB/MISSION/level2/atmPrf/YYYY.DDD/atmPrf_IIII.YYYY.DDD.HH.MM.GGG_SSSS.VVVV_nc. Explanation of this format is below:

- YYYY represents the year the reading was taken (e.g., 2022, 2023, 2019, etc.)
- DDD connotes exact day of the year (e.g., 007, 241, 364, etc.)
- HH, which represents the hour readings were taken.
- MM also represents minutes, which readings were done.
- GGG talks about the identification number of the GNSS satellite (e.g., G25 = GPS satellite 25)
- SSSS is an identification number that tells the command options used in generating this file, and this is called the subtype.
- VVVV talks about the version of the file in which this was generated.
- IIII represents the mission ID (CHAM, SACC, etc.)
- PUB is the base directory for the pub hierarchy.

The COSMIC – 2 data also contain additional descriptions, some of which are;

- reference_sat_id = GPS satellite ID for reference link
- smean = Mean difference between observational and standard climatology bending angles between 60-80 km

- stdv = Standard deviation of oscillations of the difference between observational and standard climatology bending angles between 60-80 km.
- Start time and stop time for occultation.
- Azimuth angle of the occultation plane at the tangent point with respect to the North direction, positive to the East from the North direction. The angle is measured between North and the GPS direction of the raypath.
- Dry temperature
- Refractivity Standard Deviation
- Latitude and longitude

COSMIC – 2 data profiles are distributed in a band between +40° and -40° latitude, and this data provides atmospheric (neutral) and ionospheric data (Ruston & Healy, 2020). To access COSMIC – 2 atmospheric profiles, the following steps were followed:

1. Visit the University Cooperation for Atmospheric Research (UCAR) website (https://cosmic.ucar.edu/).
2. Click on COSMIC – 2 and select COSMIC – 2 data webpage from the site (https://www.cosmic.ucar.edu/global-navigation-satellite-system-gnss background/cosmic-2).
3. On the website, click on the link (https://data.cosmic.ucar.edu/gnss-ro/cosmic2/nrt/) to open the "Index of /gnss-ro/cosmic2/nrt/", which has many files. Examples of such files are level 1a, level 1b, level 2, and others.
4. Select level 2 file, which will lead you to the years in which atmospheric data are available.

5. Click on the year to select the exact day of the year you want its atmospheric profile data.
6. Select the atmPrf_nrt.tar.gz to download the atmospheric data, which is a zip file.
7. Extract the zip file to access all the different satellites and the time at which readings were taken.

The COSMIC – 2 atmospheric profile data is a .nc file which can be opened by a Python programming code or any other computer programming language. In this research, a Python programming code was written to open and plot the atmospheric profile data. Below is a screenshot of the programming code that was used in plotting the data.

```
import netCDF4 as nc
import xarray as xr
import matplotlib.pyplot as plt
import numpy as np
import pandas as pd
data =
xr.open_dataset('C:\\Users\\pamevor\\Downloads\\atmPrf_C2E1.2023.341.00.00.G04_000
1.0001_nc')
data.variables.keys()
temp = data['Temp']+273.15


temp_anomaly = temp - temp.mean(dim='MSL_alt')

fig, ax = plt.subplots(figsize=(10, 6))
temp_anomaly.plot(y='MSL_alt', ax=ax)
plt.title('Temperature Perturbation vs Altitude')
plt.xlabel('Temperature Pertubation (K)')
plt.ylabel('Altitude (km)')
plt.show()
```

Figure 3.9: Screenshot of Python code for plotting atmospheric profile data

3.6 Statistical Analysis and Validation Techniques

This study utilizes confidence intervals and uncertainty quantification to evaluate the reliability of TEC and scintillation changes linked to climate variability, confirming that ENSO-related ionospheric responses are statistically significant and not primarily influenced by measurement noise, solar forcing, or natural variability.

Pearson Correlation Coefficient: This is used to quantify the linear relationship between ionospheric parameters like Vertical Total Electron Content (VTEC) and ENSO indices (ONI), which is described by Equation 3.3:

$$r = \frac{\Sigma[(x_i - \bar{x})(y_i - \bar{y})]}{\sqrt{[\Sigma(x_i - \bar{x})^2 \cdot \Sigma(y_i - \bar{y})^2]}} \qquad (3.3)$$

where x_i represents ONI values, y_i represents VTEC values, $\bar{x}$ and $\bar{y}$ are their respective means, and the summation is over all N observations. The statistical significance is assessed using the t-statistic described by Equation 3.4:

$$t = r\sqrt{[(N-2)/(1-r^2)]} \qquad (3.4)$$

which follows the t-distribution with $\nu = N - 2$ degrees of freedom under the null hypothesis of no correlation. The null hypothesis is rejected at the $\alpha = 0.05$ significance level if $|t| > t_{critical}(\nu, \alpha)$.

Spearman Rank Correlation: For non-linear monotonic relationships, Spearman's rank correlation coefficient is computed by Equation 3.5:

$$\rho_s = 1 - \frac{[6\Sigma d_i^2]}{[N(N^2-1)]} \tag{3.5}$$

Because ionospheric behavior is primarily driven by solar activity, climate-driven effects are often subtle. The study shows that ENSO-related TEC or scintillation fluctuations persist after accounting for solar and geomagnetic variability, thanks to confidence intervals (CI). Climate-ionosphere coupling claims become more credible as a result. Some of the CI used are as follows:

Bootstrap Resampling: Bootstrap resampling, described in Equation 3.6, is used to determine the 95% confidence intervals for the mean VTEC values. The confidence interval for B = 1000 bootstrap iterations is:

$$CI_{95\%} = [\hat{\theta}_{(\alpha/2)} * \hat{\theta}_{(1-\alpha/2)}] \tag{3.6}$$

where $\hat{\theta}_{(p)}$ is the pth percentile of the bootstrap distribution of the statistic $\hat{\theta}$ (e.g., mean VTEC), and $\alpha = 0.05$ for 95% confidence.

3.7 Plotting of vertical TEC (VTEC) and detrended vertical TEC (dTEC) against universal time

The next step of the methodology is the application of a Python programming code, thus written to analyze the various VTEC data from the GPS satellite and its receivers. The Python code was written to plot a graph of VTEC against time (universal time (UT)) to know the peak ionospheric scintillation during the day. The code, which is found in the appendix of this book, made use of Python libraries NumPy, Matplotlib, Pandas, etc., which enabled us to analyze the data and plot the VTEC values against time (UT). Parashar (2024) defined Python libraries as “A Python library is a collection of pre-written code modules that provide a set of functionalities to perform specific tasks," and Ramuglia (2023) explains libraries, especially Python libraries, as already-made toolkits made for computer programmers. Libraries contain functions and tools that are designed for specific purposes. The functions of these libraries used for the analysis and plotting of the graphs are as follows:

1. NumPy: This library is a basic computing library created specifically for advanced mathematical operations and numerical data processing. They effectively handle and store enormous numbers. When it comes to Fourier transforms, it is really helpful.
2. The second is Matplotlib, a data visualization framework that facilitates data analysis and exploration as well as graph charting (line, bar, histogram, scatter, 3D, etc.). Matplotlib works nicely with other Python libraries, such as Pandas and NumPy.
3. Pandas: This open-source library presents the two-dimensional labelled data with rows and columns (DataFrame) and the one-dimensional labelled array (series). It is utilized for managing missing values, organizing data (filtering, sorting, grouping, and merging datasets), and carrying out other data operations.

CHAPTER FOUR

4. RESULTS AND DISCUSSIONS

4.1 Results

In this section of the chapter, we present the results of the various methods used in Chapter Three in relation to the research work. In the previous chapter, we discussed three methods in our work, and these are:

I. Acquisition of the El Niño Southern Oscillation (ENSO) data.
II. Acquisition and plotting of the temperature profile (TP) data.
III. Acquisition and plotting of the total electron content (TEC) data.

The ENSO data and temperature profile data were examined to see whether they affected electron density in the ionosphere. El Niño and La Niña have a direct association with temperature profiles and atmospheric dynamics, particularly in the lower and middle atmospheres (Pedatella & Liu, 2013; García-Herrera et al., 2006).

4.1.1 ENSO data

Our ENSO data were taken from the National Oceanic and Atmospheric Administration (NOAA) and the Golden Gate Weather Services (GGWS). Table 4.1 shows the readings of the ENSO temperature anomalies recorded in their respective years of events. La Niña happened in the middle of 2020 and ended in July 2021, while El Niño started in June 2023 and ended in July 2024. These are the recent ENSO activities that have also impacted the global temperature.

Table 4.1: ENSO activities recorded data

THREE-MONTH MOVING AVERAGES	LA NINA 2020/2021 TEMPERATURE ANOMALY (˚C)	EL NIÑO 2023/2024 TEMPERATURE ANOMALY (˚C)
JJA	-0.40	+1.10
JAS	-0.60	+1.30
ASO	-0.90	+1.60
SON	-1.20	+1.80
OND	-1.30	+1.90
NDJ	-1.20	+2.00
DJF	-1.10	+1.80
JFM	-0.90	+1.50
FMA	-0.80	+1.10
MAM	-0.70	+0.70
AMJ	-0.50	+0.40
MJJ	-0.40	+0.2

The system used in measuring ENSO activities is the Oceanic Niño Index (ONI), and this metric is used to define ENSO as El Niño or La Niña events. According to the classifications done in 3.2.1 in chapter three, our La Niña results fall under a moderate event, which ranges from -1.0˚C to -1.49˚C temperature anomaly. The El Niño readings obtained in the 2023/24 ENSO season can be said to be a strong El Niño event, and this has a temperature anomaly of 2.0 °C or higher.

The Oceanic Niño Index (ONI) measures the Sea Surface Temperature (SST) deviations in a region from their long-term average. This average calculation is called a moving average or running average, and it's calculated as a running average of sea surface temperature anomalies over the past three months. This is done to reduce short-term variations and provide a steady indicator of overall trends. The ocean-atmosphere relations are monitored especially in regions of 5° N-5° S, 120° W-170° W, and this region is called the Niño 3.4 region.

The negative (-) temperature anomaly shows global temperatures reduced or became colder than expected, while the positive (+) temperature anomaly shows that average global temperatures became warmer than expected. From Table 4.1, we can see that during El Niño events, average global temperatures become warmer than expected temperatures, which may have been predicted by climate scientists with models like the Whole Atmosphere Community Climate Model (WACCM), European Centre for Medium-Range Weather Forecasts' (ECMWF) ECMWF reanalysis v5 (ERA5), etc. For La Niña periods, global average temperatures become colder than anticipated or predicted by climate or weather agencies. Johnston et al. (2022) agree that tropical tropospheric interannual climate variability is dominated by ENSO, which causes cooling in the tropical lower stratosphere. This cooling in the lower stratosphere mostly happens in the middle latitudes and high latitudes, where the mean meridional circulation of the stratosphere is modified by the travelled ENSO signals. In the next session, we will look at the temperature profile since it has a correlation to the ENSO activities.

4.1.2 Temperature perturbation profile graph

The atmospheric temperature profile is how the temperature of the atmosphere changes as a function of altitude. The temperature profile of the atmosphere makes it possible to differentiate the various levels of the atmosphere vertically and also describe the thermodynamic state of the atmosphere (Wang et al., 2023). The temperature data from the COSMIC global navigation satellite system (GNSS) radio occultation (RO) provides a near-global coverage for daily means spanning from 2019 – 2024. The data used in plotting the temperature profile, which was produced by COSMIC – 2 or FORMOSAT – 7 missions, has high precision and a high accuracy rate, vertical resolution is very high, and it is unresponsive to clouds and precipitation. The global coverage distribution is comparatively even in spacetime, which makes COSMIC or FORMOSAT data ideal for climate variability studies. Many researchers have used FORMOSAT data to study and understand atmospheric climate systems (Johnston et al., 2022), especially Scherllin-Pirscher et al. (2012), who analyze the vertical and spatial structure of temperatures during ENSO activities.

The data from the Constellation Observing System for Meteorology, Ionosphere, and Climate – 2 (COSMIC-2) mission have been said to be more precise and accurate, especially when it comes to the lower atmosphere. When Ho et al. (2020) compared the COSMIC-2 data to other satellite radio occultation (RO) data, such as the National Oceanic and Atmospheric Administration's (NOAA) Satellite Applications and Research's (STAR) data, they found that COSMIC-2 had a significantly higher signal-to-noise ratio (SNR) than earlier RO missions. As a result, Vaisala RS41 radiosonde measurements were deployed to assess the accuracy and uncertainty of COSMIC-2 neutral atmospheric profiles. In general, the COSMIC-2 data quality in terms of stability, precision, accuracy, and uncertainty is extremely consistent with that of COSMIC-1. Schreiner et al. (2020) also agreed to the affirmations of Ho et al. (2020) by saying that "initial data from the Formosat Satellite-7 / Constellation Observing System for Meteorology Ionosphere and Climate (FORMOSAT-7/COSMIC-2, hereafter C2), a recently launched equatorial constellation of six satellites carrying advanced radio occultation receivers, exhibit high signal-to-noise ratio, precision, and accuracy, and the ability to provide high vertical resolution profiles of bending angles and refractivity, which contain information on temperature and water vapor in the challenging tropical atmosphere." Zhang et al. (2022) in their research accepted that there were a few centimeter differences between the COSMIC – 2 mission data and the NOAA STAR data. Zhang et al. (2022) revealed that the excess phase difference between UCAR and STAR is less than a centimeter at high altitudes, but rises as one descends into the lower atmosphere. The mean relative bending angle (BA) discrepancies at impact heights ranging from 10 km to 30 km are less than 0.1% for GLONASS L2C signals and GPS L2C and L2P signals. In all these statements, we are right to use the COSMIC – 2 / FORMOSAT – 7 atmospheric temperature data for the research.

Figures 4.1a – 4.1l and 4.2A – 4.2L describe the graphs of temperature perturbation anomaly against altitude. The data provided us with a temperature profile of 0 to 60 km altitude. Figures 4.1a – 4.1l and 4.2A – 4.2L show the temperature perturbation profile of the globe at specific times of reading, thus 05:00 am, 10:00 am, 03:00 pm, and 08:00 pm. These times were used because our total electron content graphs (figs. 4.3 and 4.4) show that the ionosphere's satellite signals shift over these periods. The El Niño year 2023–2024 temperature profile is shown in Figure 4.1a to Figure 4.1l.

The days selected for both El Niño and La Niña are days the Earth witnessed low solar activity or no solar activity from the sun. That is to say, there was no massive ejection of particles or energy from the sun that could have caused a disturbance in the ionosphere, which would have affected satellite signals to their receivers. The temperature profile from the troposphere to the ionosphere can tell us the influence of climate variables on ionospheric scintillation. Below are the temperature perturbation profile graphs during the El Niño season in 2023/24.

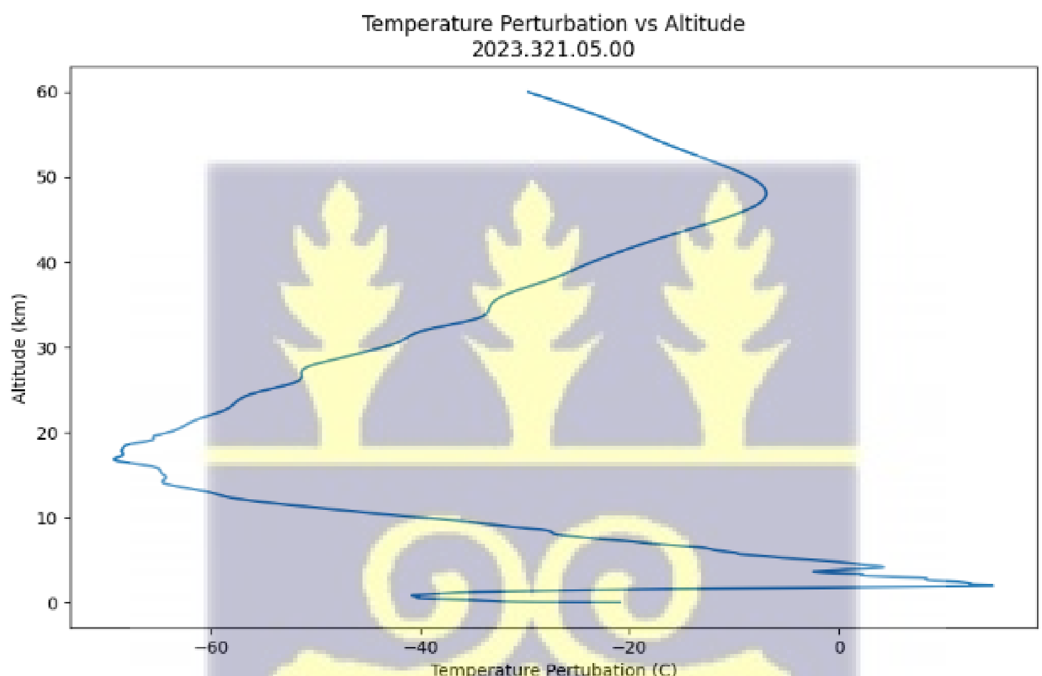

Figure 4.1a: Atmospheric temperature profile during El Niño (2023/24) day 321 at 5:00 UT

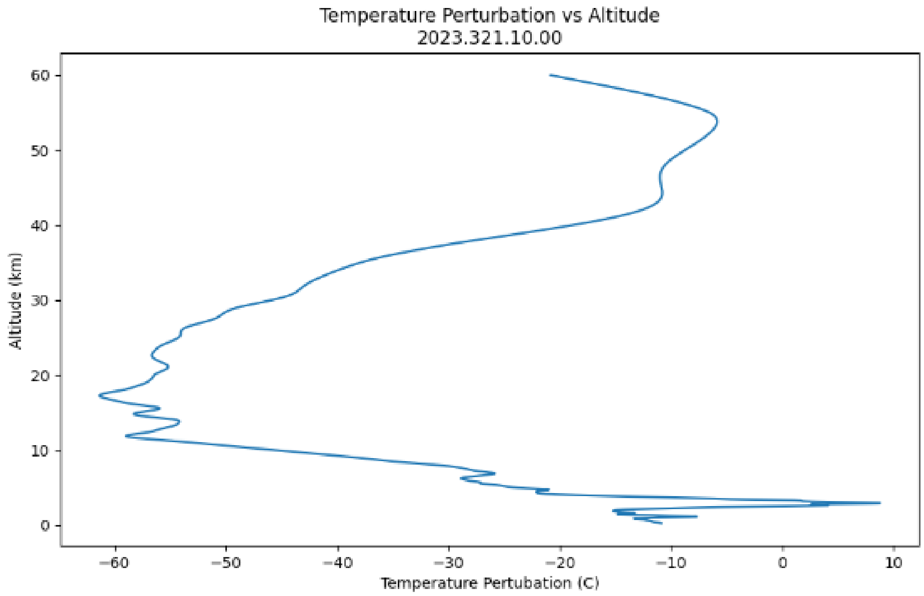

Figure 4.1b: Atmospheric temperature profile during El Niño (2023/24) day 321 at 10:00 UT

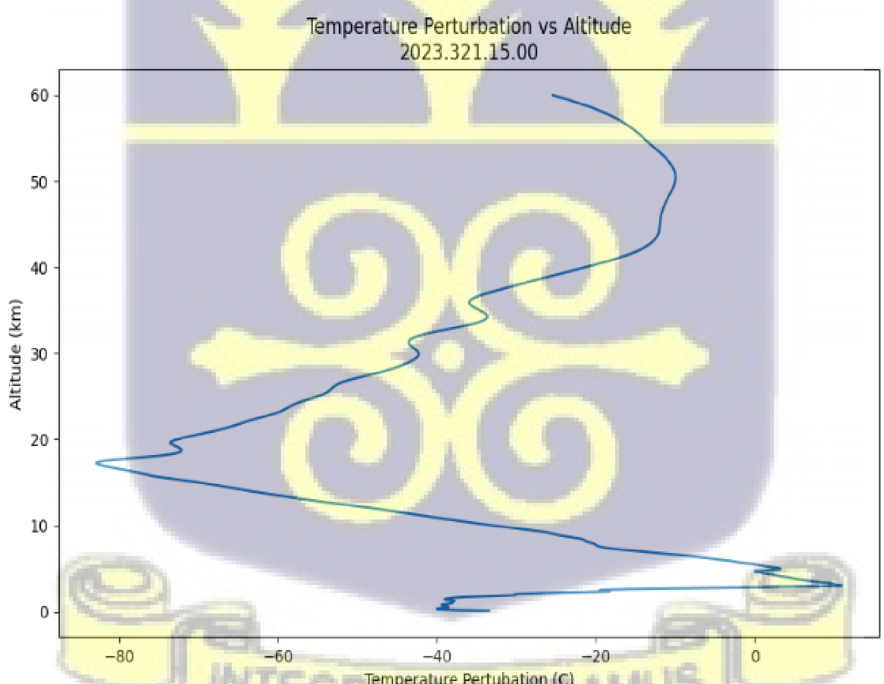

Figure 4.1c: Atmospheric temperature profile during El Niño (2023/24) day 321 at 15:00 UT

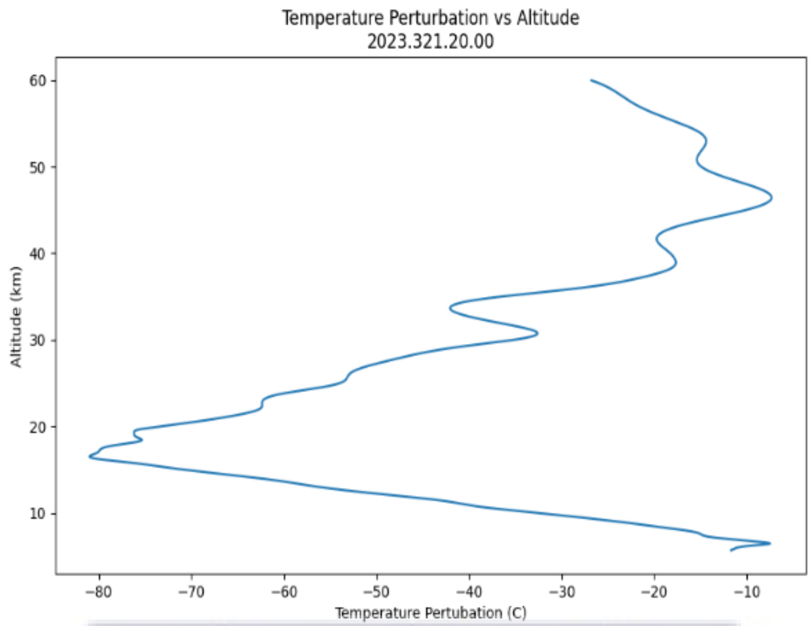

Figure 4.1d: Atmospheric temperature profile during El Niño (2023/24) day 321 at 20:00 UT

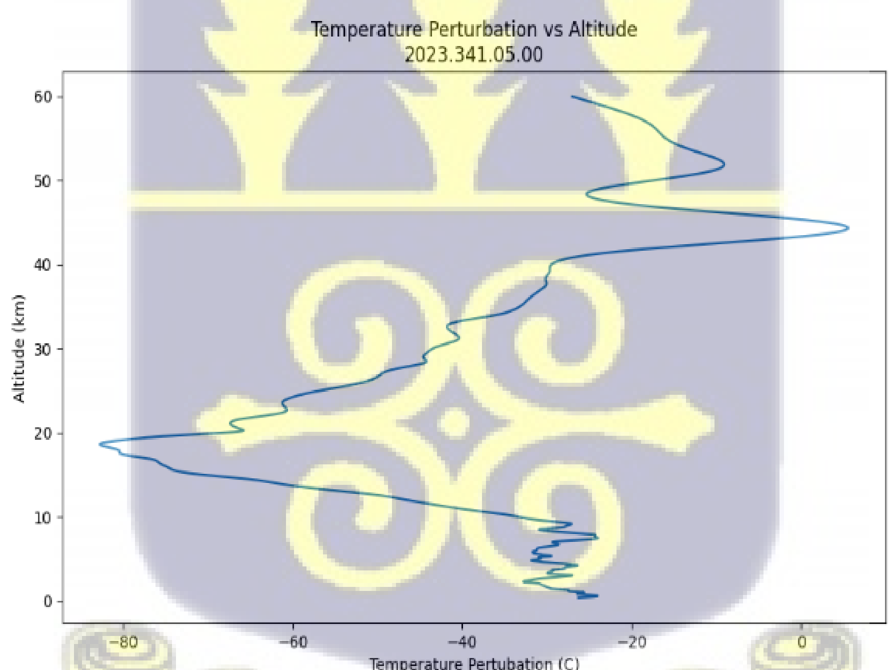

Figure 4.1e: Atmospheric temperature profile during El Niño (2023/24) day 341 at 05:00 UT

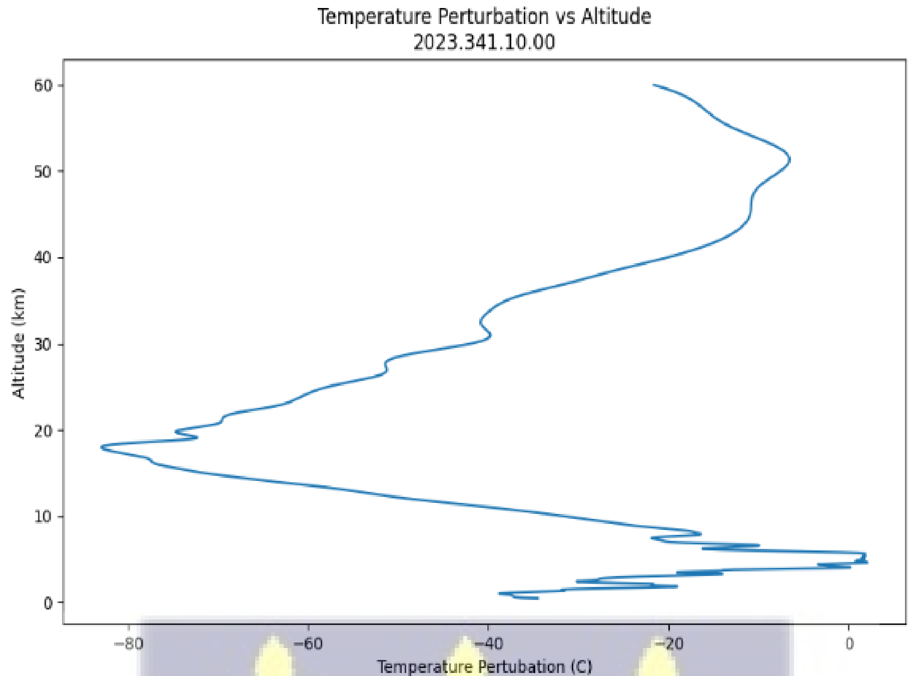

Figure 4.1f: Atmospheric temperature profile during El Niño (2023/24), day 341 at 10:00 UT

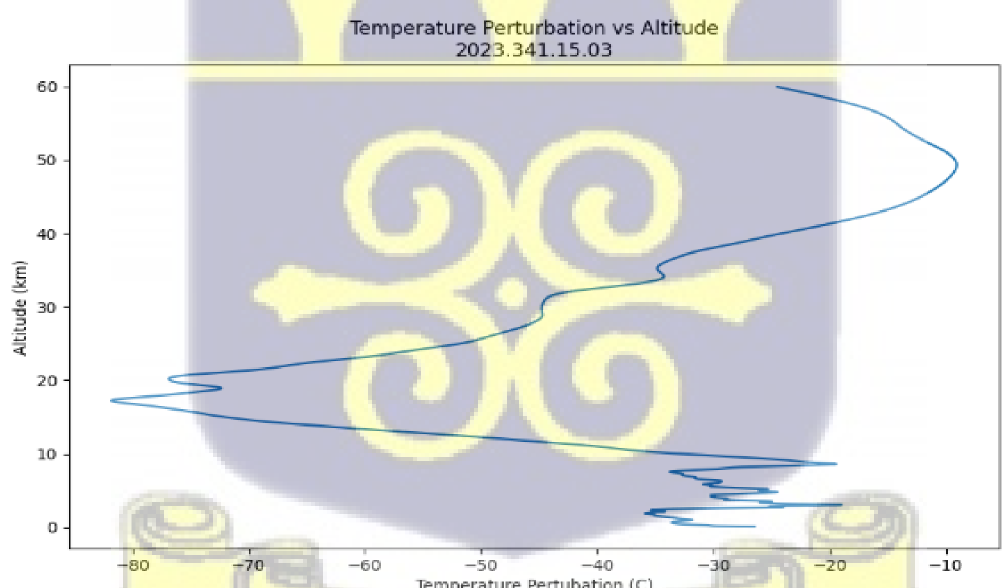

Figure 4.1g: Atmospheric temperature profile during El Niño (2023/24) day 341 at 15:03 UT

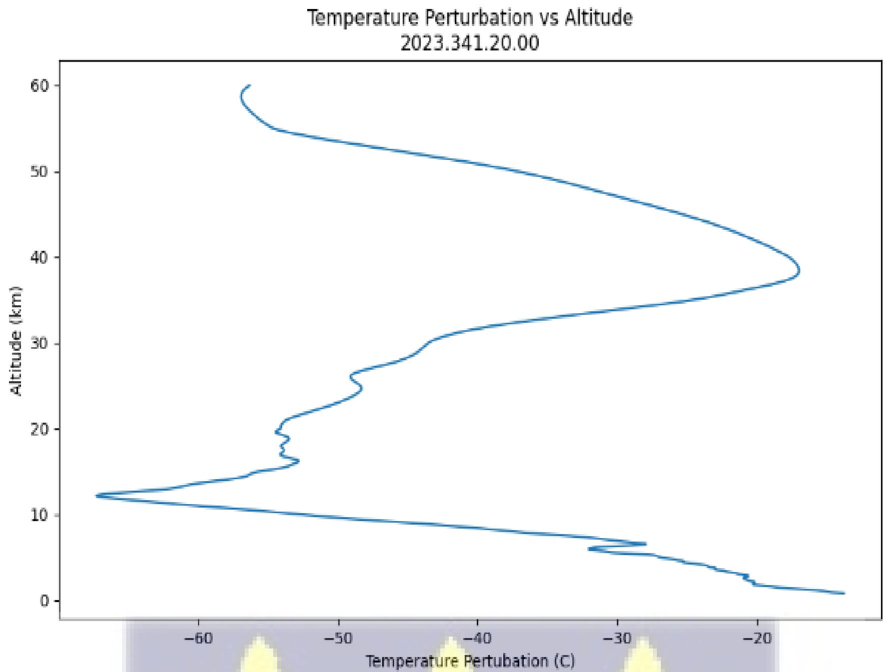

Figure 4.1h: Atmospheric temperature profile during El Niño (2023/24) day 341 at 20:00 UT

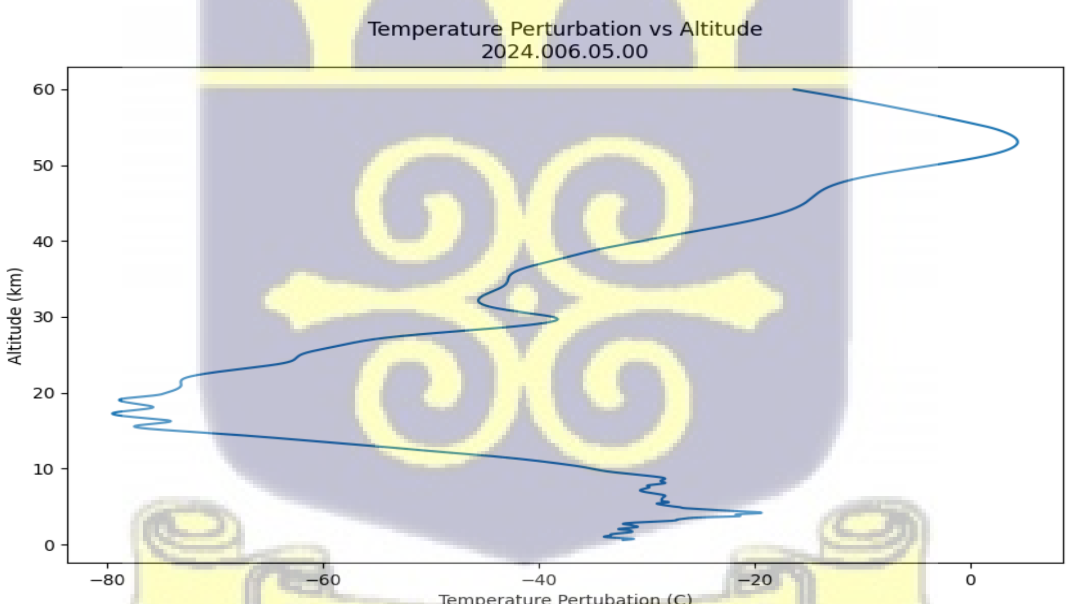

Figure 4.1i: Atmospheric temperature profile during El Niño (2023/24) day 006 at 05:00 UT

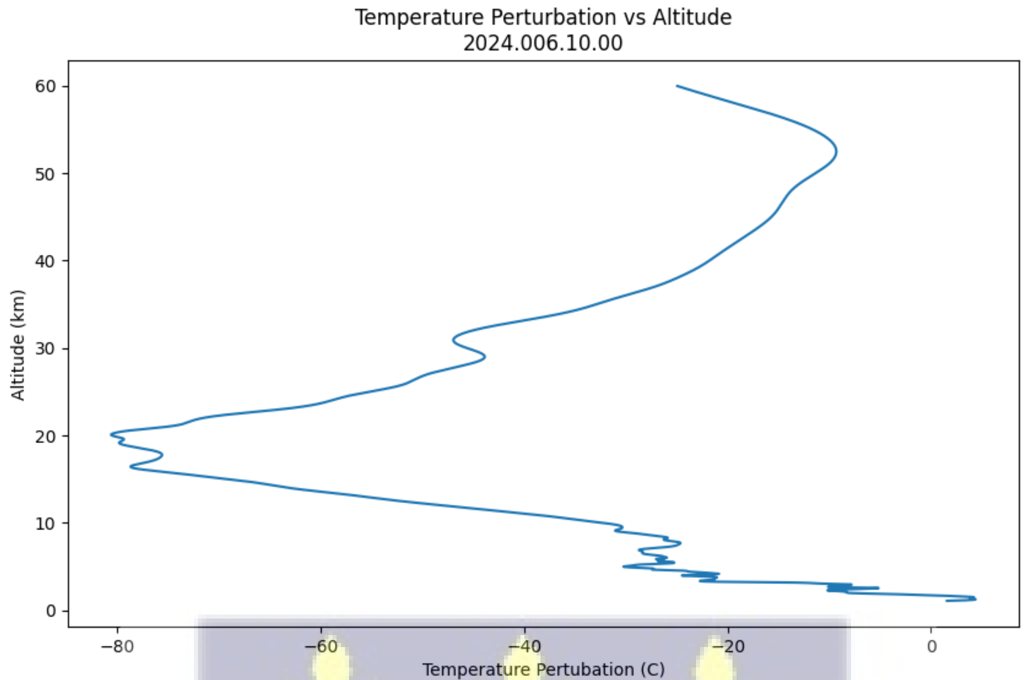

Figure 4.1j: Atmospheric temperature profile during El Niño (2023/24) day 006 at 10:00 UT

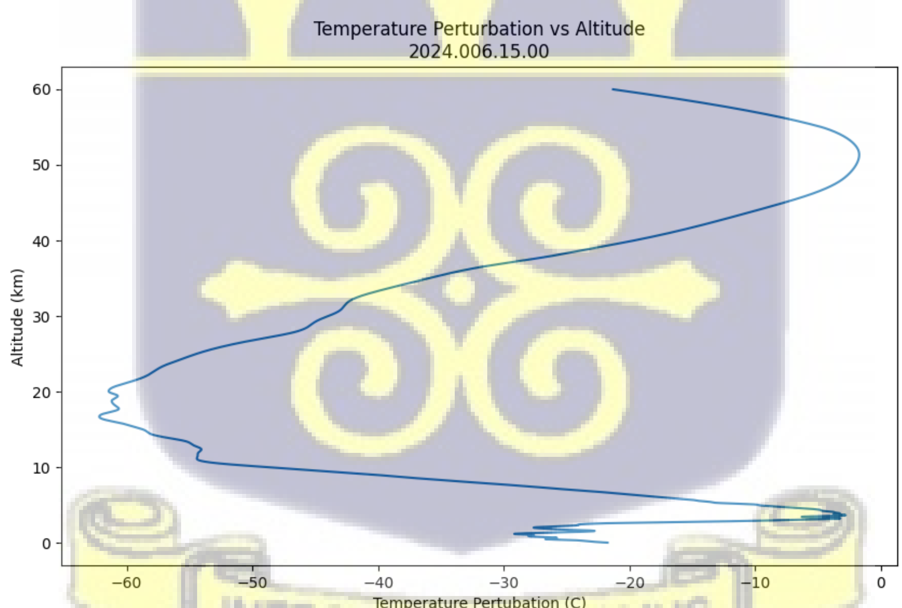

Figure 4.1k: Atmospheric temperature profile during El Niño (2023/24) day 006 at 15:00 UT

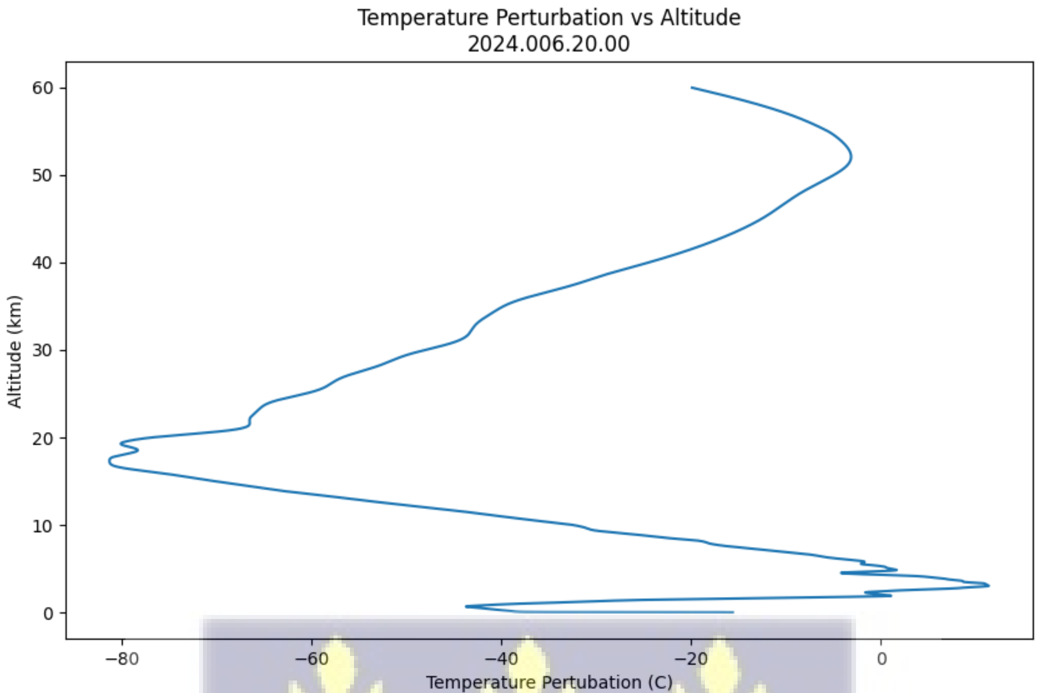

Figure 4.11: Atmospheric temperature profile during El Niño (2023/24) day 006 at 20:00 UT

The graphs below (Figures 4.2A to 4.2L) show the temperature perturbation profile of atmospheric altitude 0 to 60 km during the La Niña 2020/2021 event.

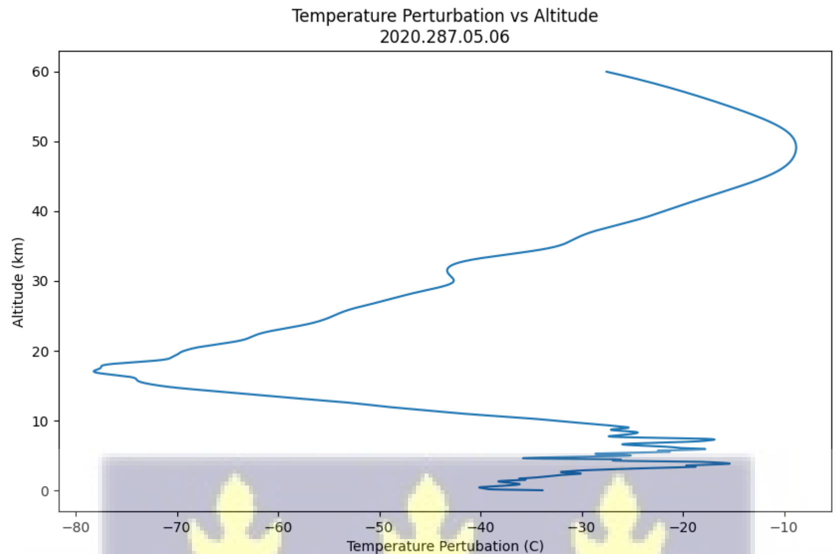

Figure 4.0.2A: La Niña 2020/21 atmospheric temperature profile on day 287 at 05:06 UT

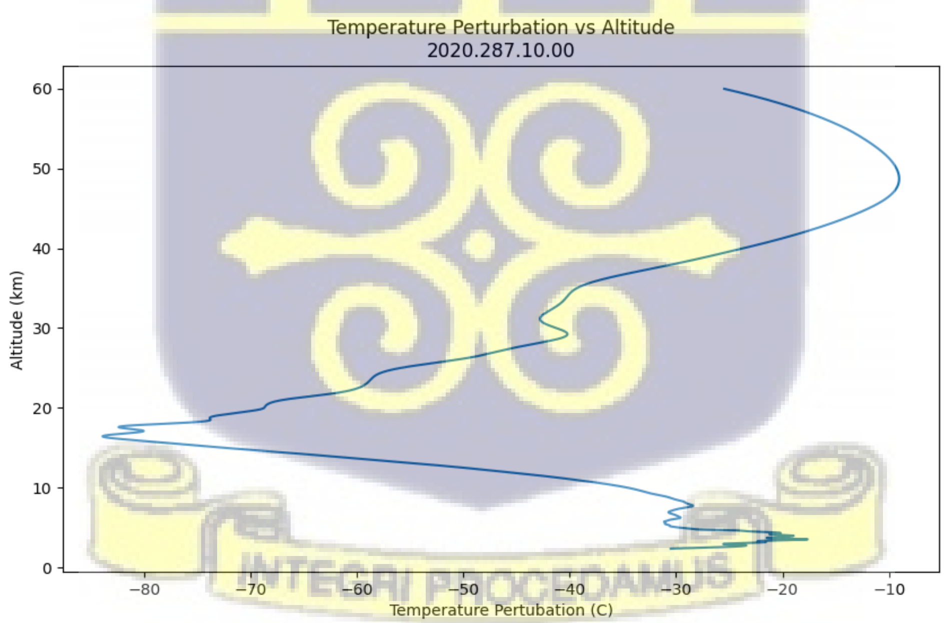

Figure 4.2B: La Niña 2020/21 atmospheric temperature profile on day 287 at 10:00 UT

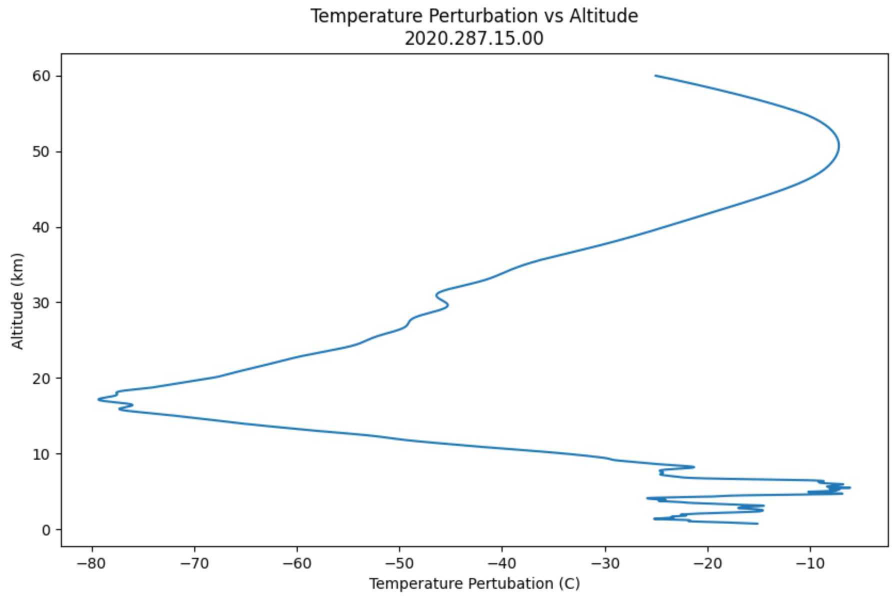

Figure 4.2C: La Niña 2020/21 atmospheric temperature profile on day 287 at 15:00 UT

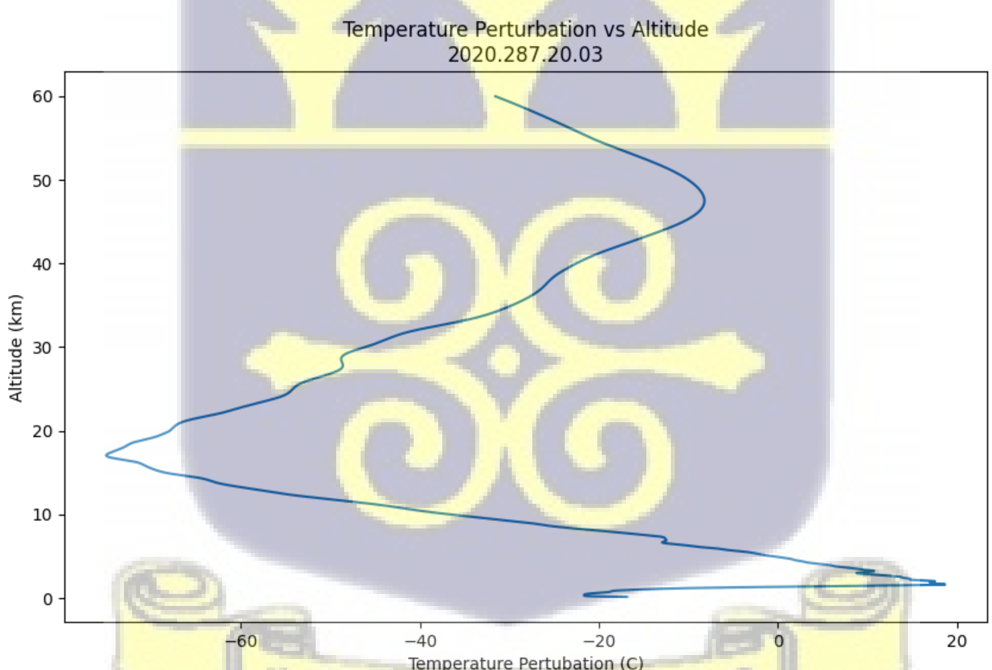

Figure 4.2D: La Niña 2020/21 atmospheric temperature profile on day 287 at 20:03 UT

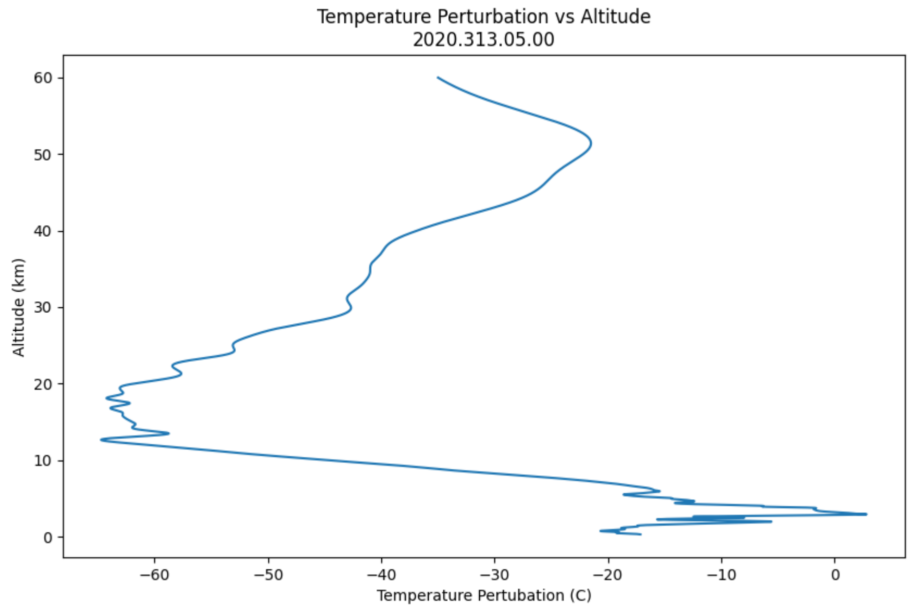

Figure 4.2E: La Niña 2020/21 atmospheric temperature profile on day 313 at 05:00 UT

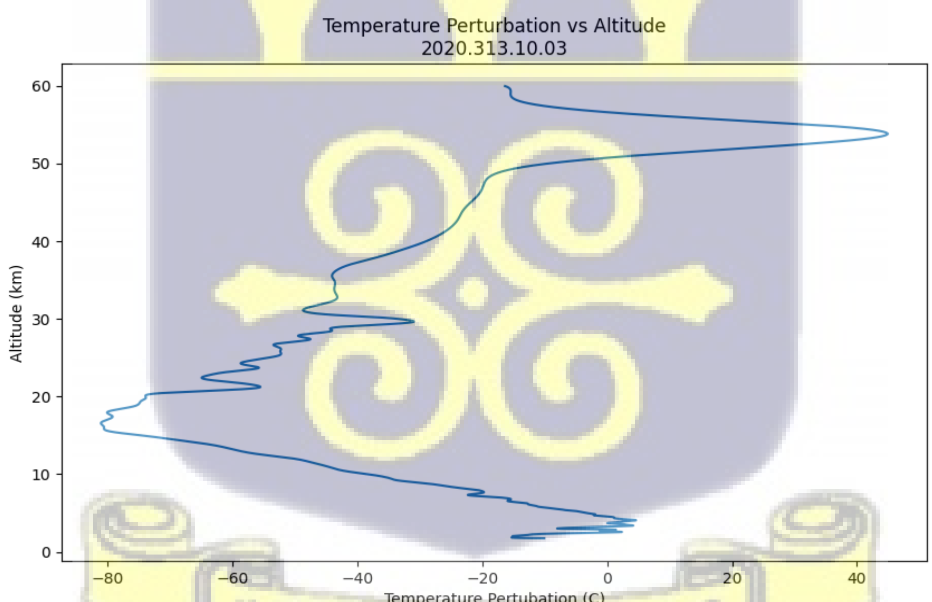

Figure 4.2F: La Niña 2020/21 atmospheric temperature profile on day 313 at 10:03 UT

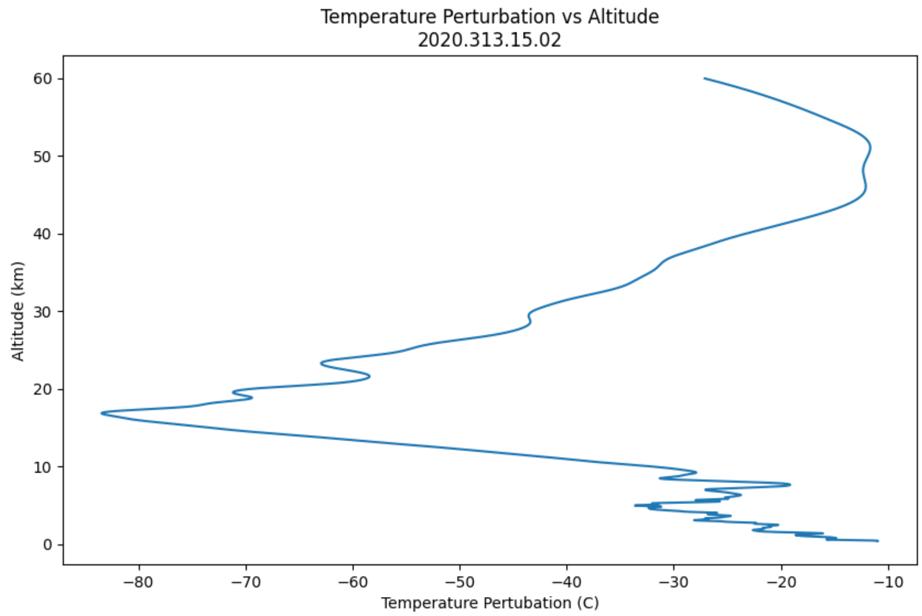

Figure 4.2G: La Niña 2020/21 atmospheric temperature profile on day 313 at 15:02 UT

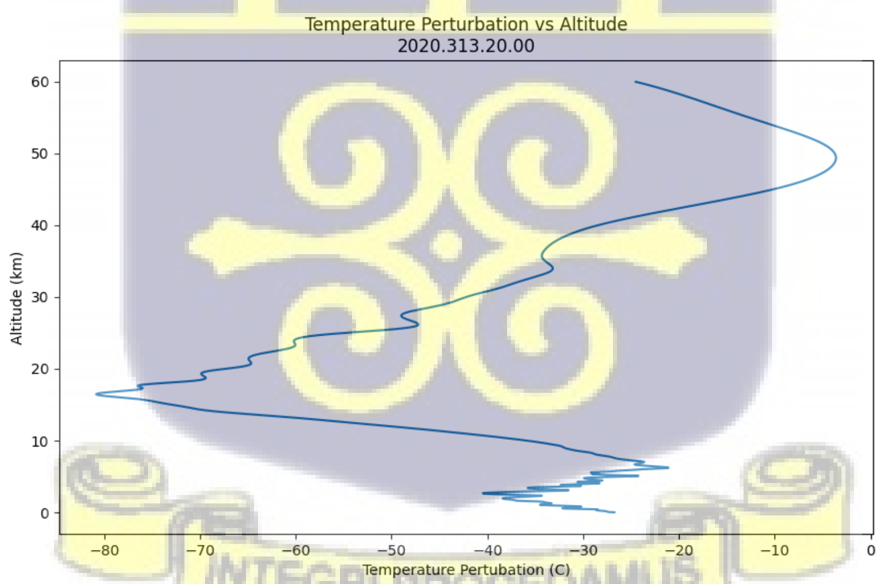

Figure 4.2H: La Niña 2020/21 atmospheric temperature profile on day 313 at 20:00 UT

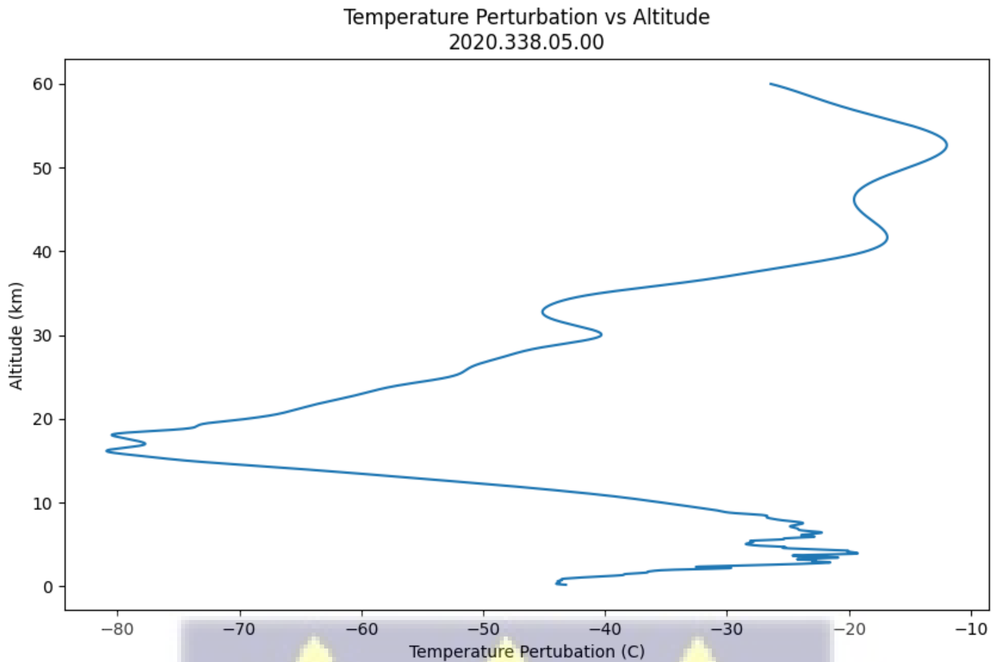

Figure 4.2I: La Niña 2020/21 atmospheric temperature profile on day 338 at 05:00 UT

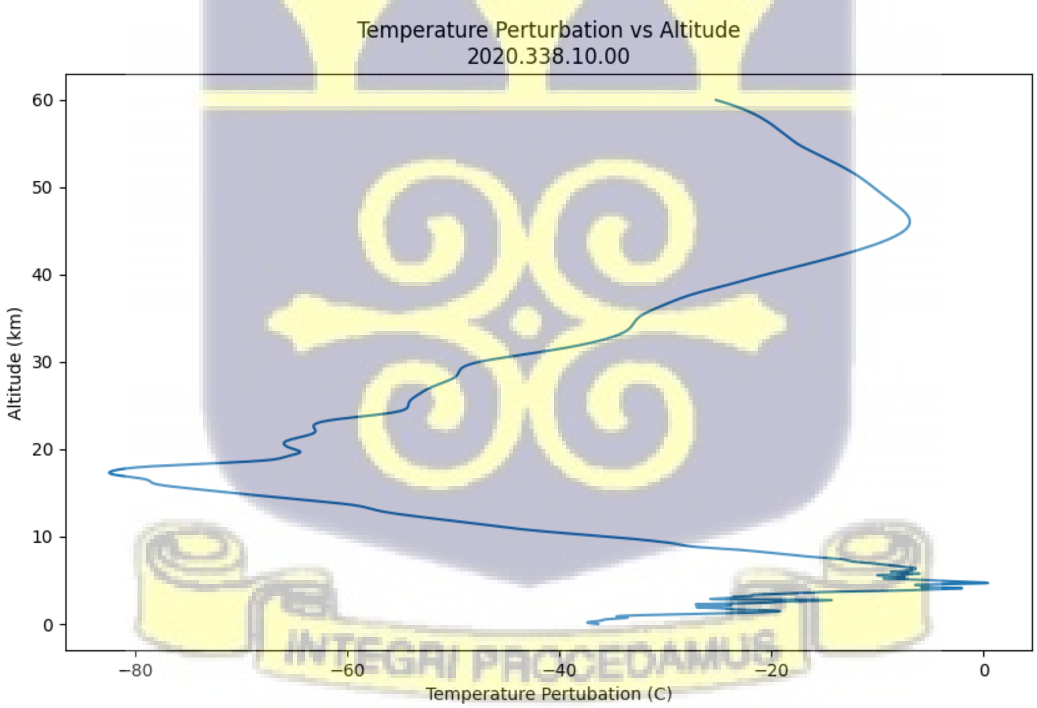

Figure 4.2J: La Niña 2020/21 atmospheric temperature profile on day 338 at 10:00 UT

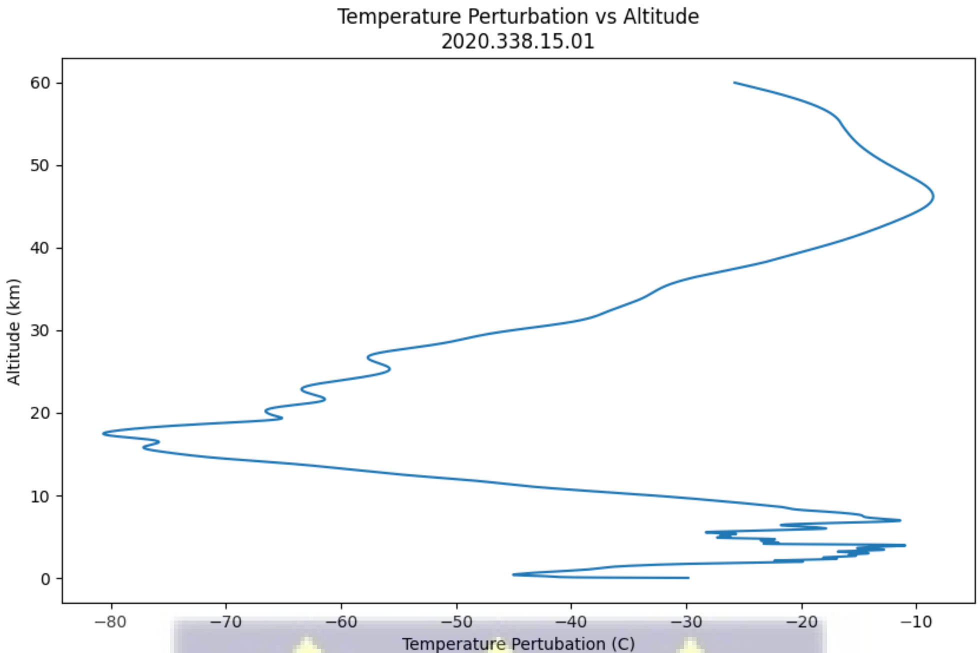

Figure 4.2K: La Nina 2020/21 atmospheric temperature profile on day 338 at 15:01 UT

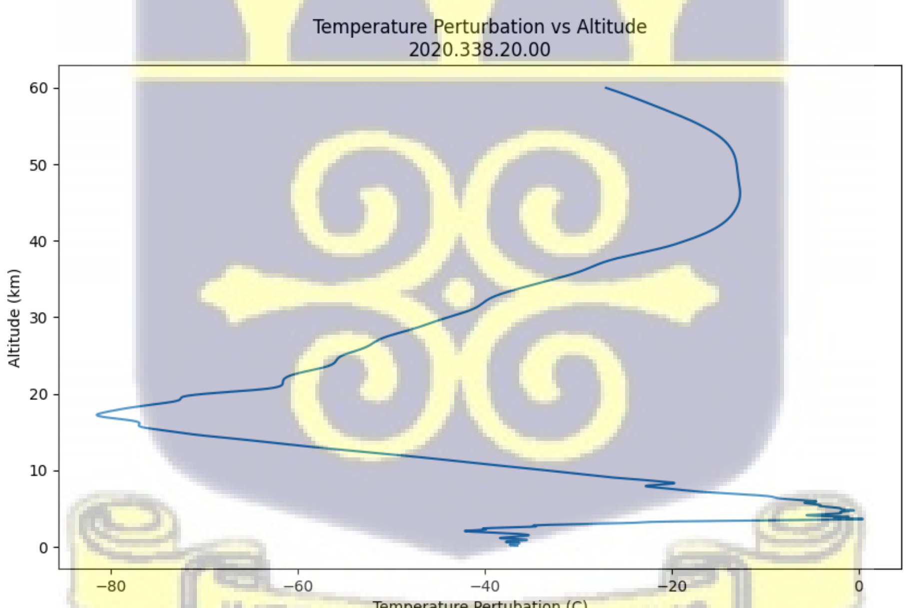

Figure 4.2L: La Niña 2020/21 atmospheric temperature profile on day 338 at 20:00 UT

4.1.3 Total electron content (TEC) graph

The graphs (Figures 4.3a - 4.3h, and Figures 4.4A – 4.4H) illustrate daily changes in ionospheric electron content (VTEC) and its correlation with ENSO weather patterns. The plots at the top (red graph) illustrate how VTEC varies during the day, while the lower parts (blue graph) separate short-term oscillations in electron content by removing the overall trend. The ionosphere is constantly changing due to solar radiation, geomagnetic activity, and specific atmospheric conditions. It is well known that the day-night cycle affects the ionosphere's electron density, with more ionized particles present during the day. Scintillation may be caused by the ionization of particles in the ionosphere, which is heavily influenced by local time, latitude, seasons, and waves from the lower atmosphere, according to NOAA.

The COSMIC-2 missions provide ionospheric TEC data, electron density profiles, and scintillation amplitude indices, which are calculated by the onboard tri-GNSS radio occultation system (TGRS), among other data, by the University Corporation for Atmospheric Research (UCAR) (Straus et al., 2022). In this study, the GPS-TEC data provided by Gopi Seemala are in the form of a Receiver Independent Exchange (RINEX) file. The Gopi software provided the TEC values, thus STEC and VTEC, in which the VTEC and it detrended VTEC were plotted against universal time (UT). Figure 4.3a through to Figure 4.3h below are TEC profile graphs which represent the climate variable El Niño.

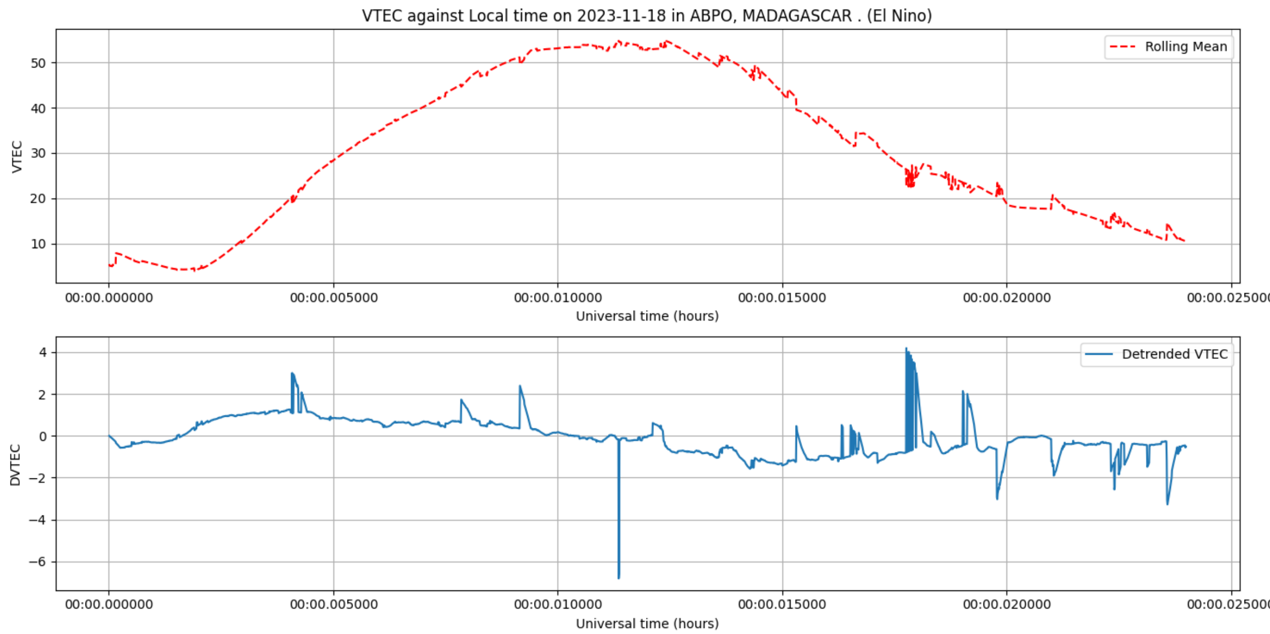

Figure 4.3a: Ionospheric VTEC and dVTEC of Antananarivo (Abpo), Madagascar during El Niño year 2023/24 on 18th November, 2023

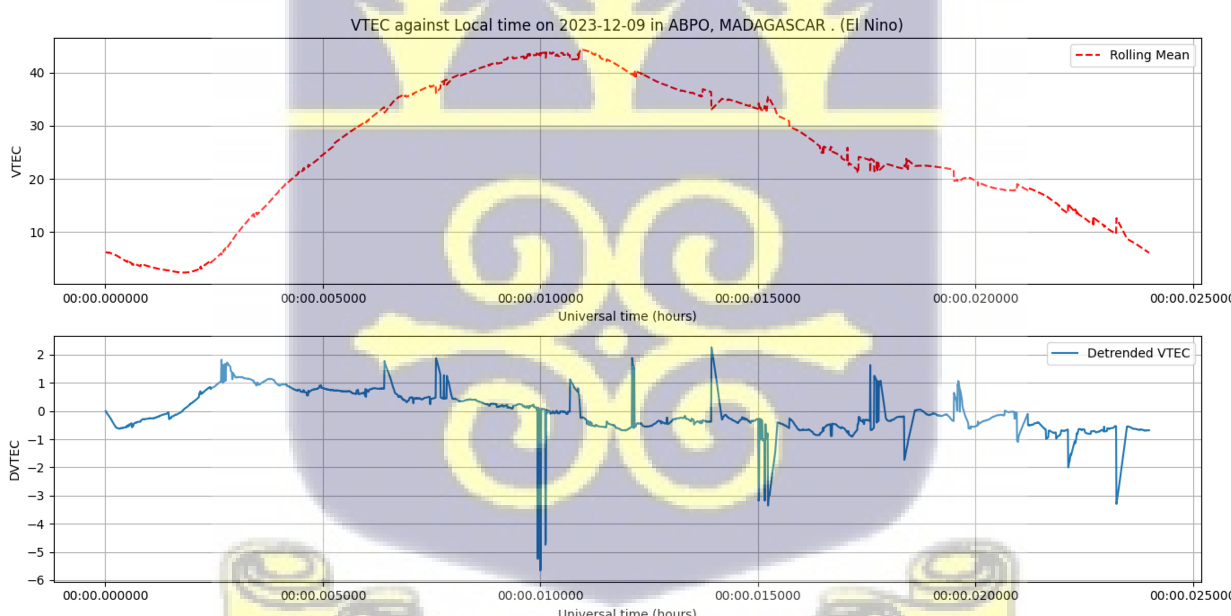

Figure 4.3b: Ionospheric VTEC and dVTEC of Antananarivo (Abpo), Madagascar during El Niño year 2023/24 on 9th December, 2023

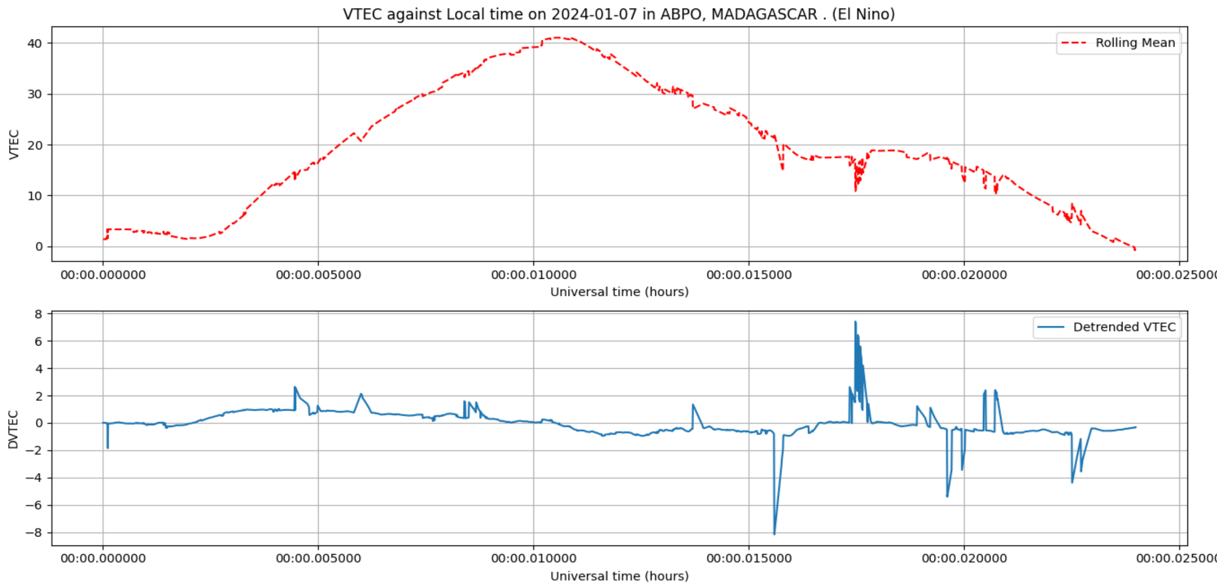

Figure 4.3c: Ionospheric VTEC and dVTEC of Antananarivo (Abpo), Madagascar during El Niño year 2023/24 on 7th January, 2024

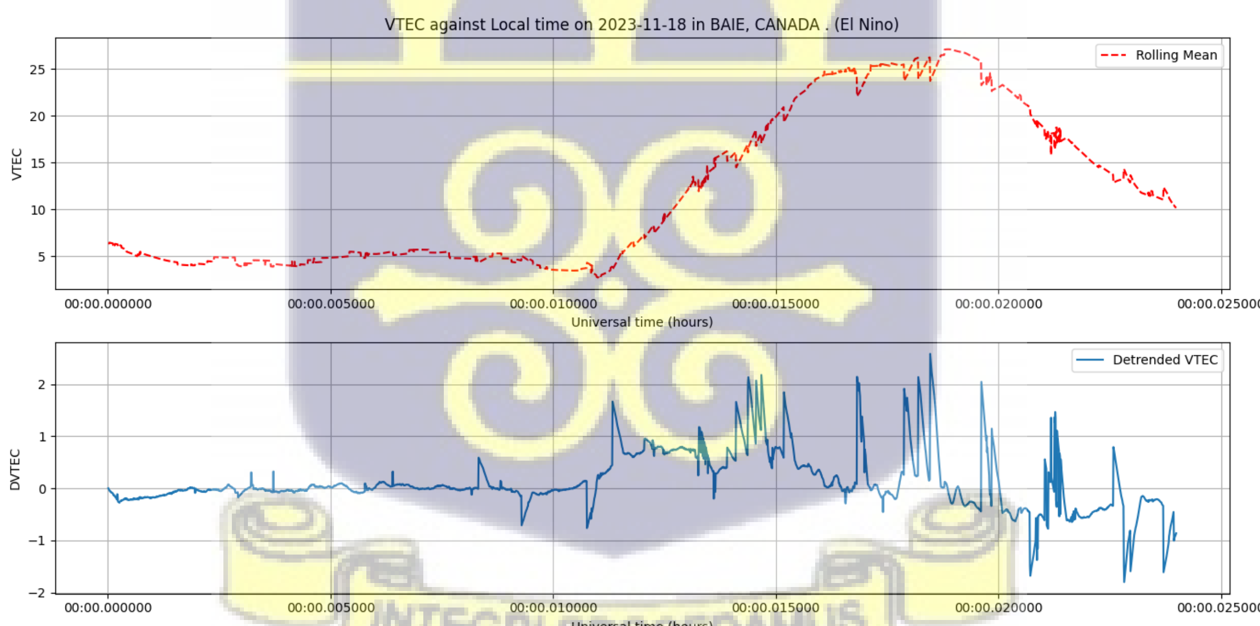

Figure 4.3d: Ionospheric VTEC and dVTEC of Baie Comeau (Baie), Canada during El Niño year 2023/24 on 18th November, 2023

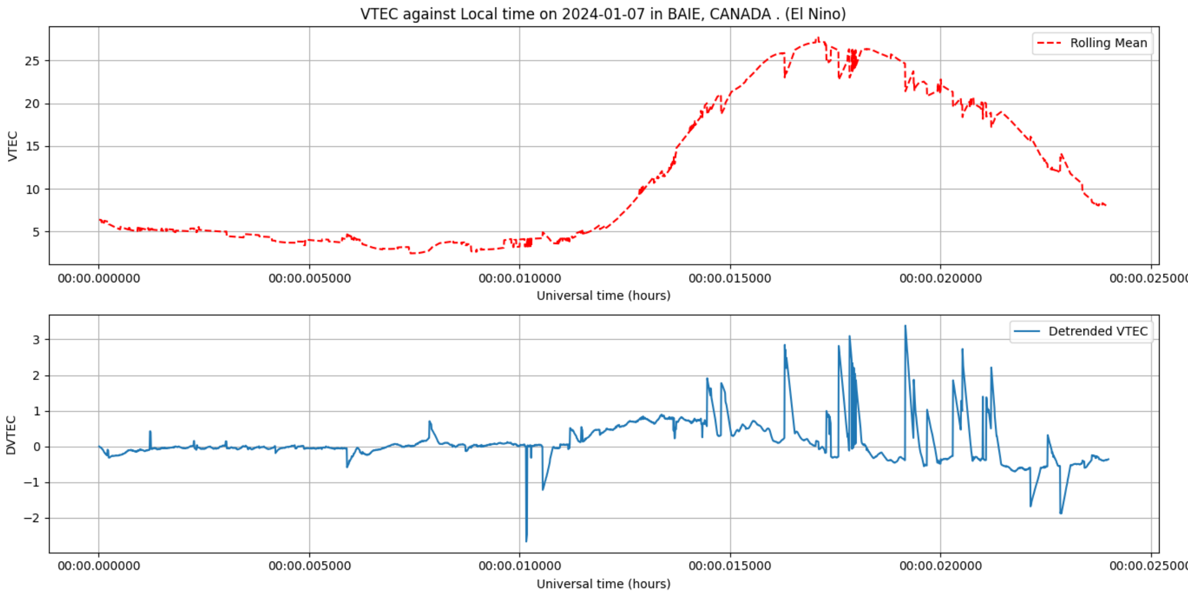

Figure 4.3e: Ionospheric VTEC and dVTEC of Baie Comeau (Baie), Canada during El Niño year 2023/24 on 7th January, 2024

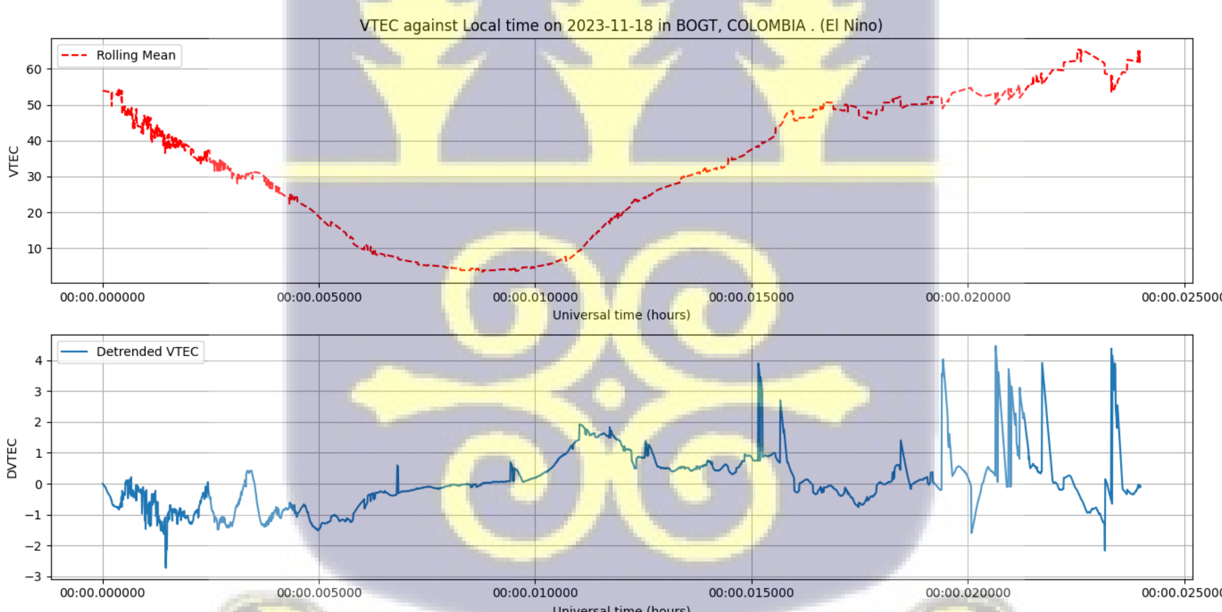

Figure 4.3f: Ionospheric VTEC and dVTEC of Bogota (Bogt), Colombia during El Niño year 2023/24 on 18th November, 2023

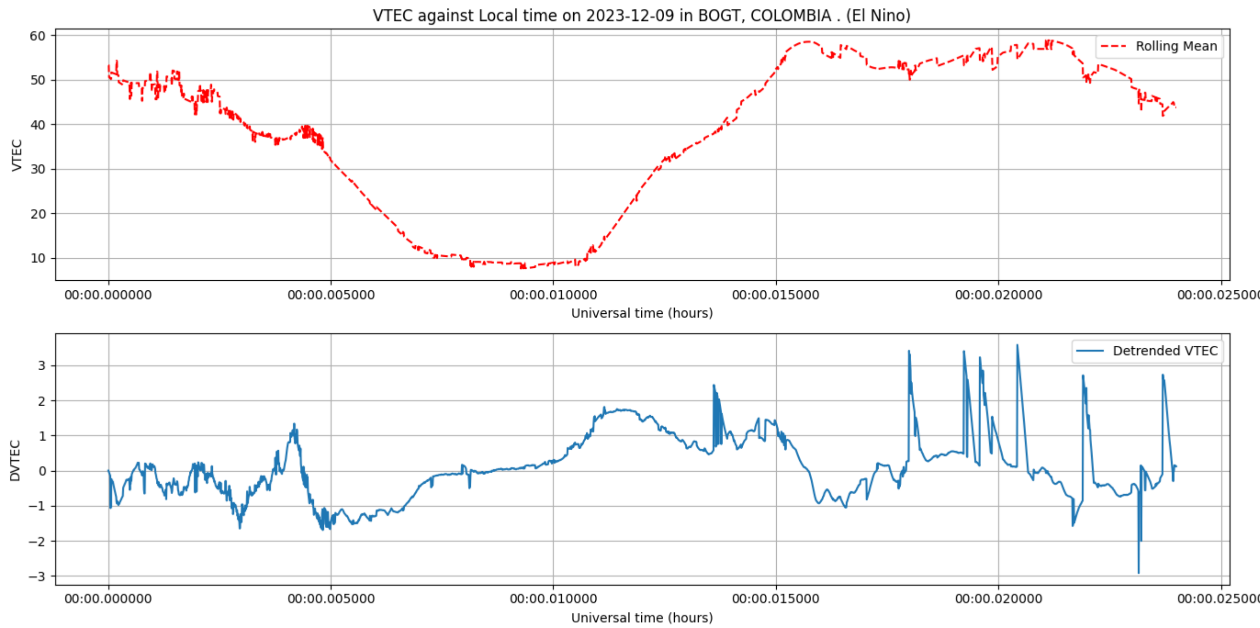

Figure 4.3g: Ionospheric VTEC and dVTEC of Bogota (Bogt), Colombia during El Niño year 2023/24 on 9th December, 2023

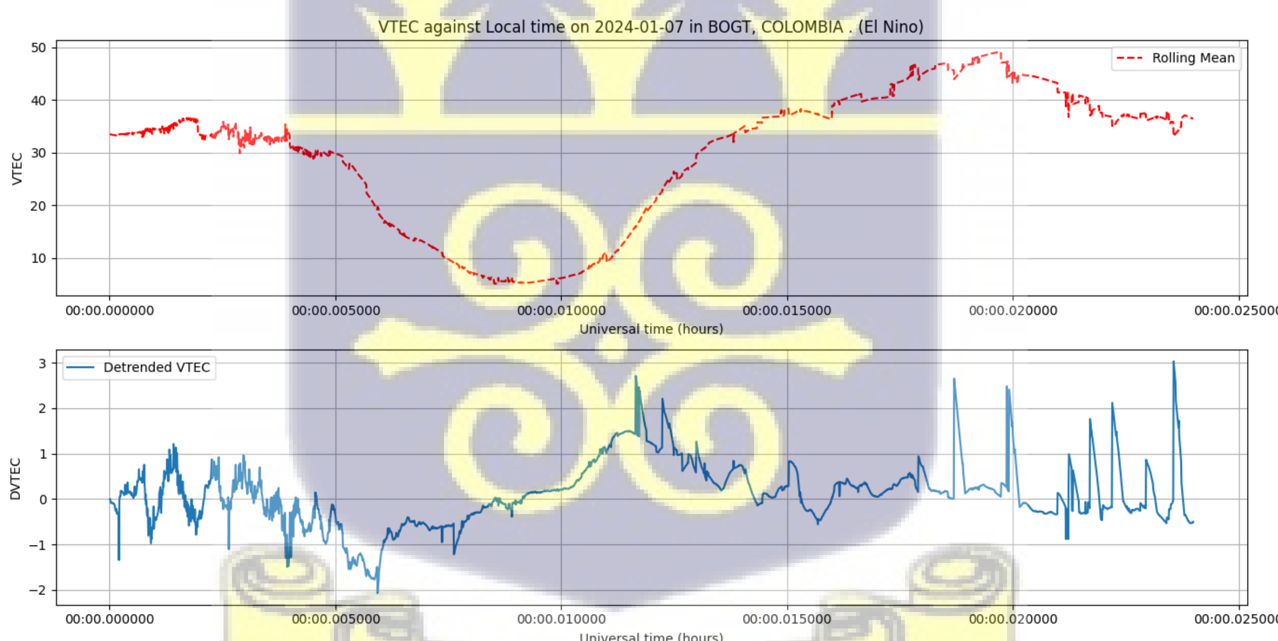

Figure 4.3h: Ionospheric VTEC and dVTEC of Bogota (Bogt), Colombia during El Niño year 2023/24 on 7th January, 2024

The red curves shown in the graphs represent the rolling mean or the moving average of the satellites' VTEC readings whiles the blue curve is the detrended VTEC, which is the application of long-term trends or noise that causes the anomalies in the reading to be removed, showing more obvious variations of the TEC profile. The detrended VTEC helps to detect short-term instabilities, which are more regular during variations in atmospheric conditions. Figures 4.4A through 4.4H represent the ionospheric VTEC and detrended VTEC of the locations during the La Niña event in 2020.

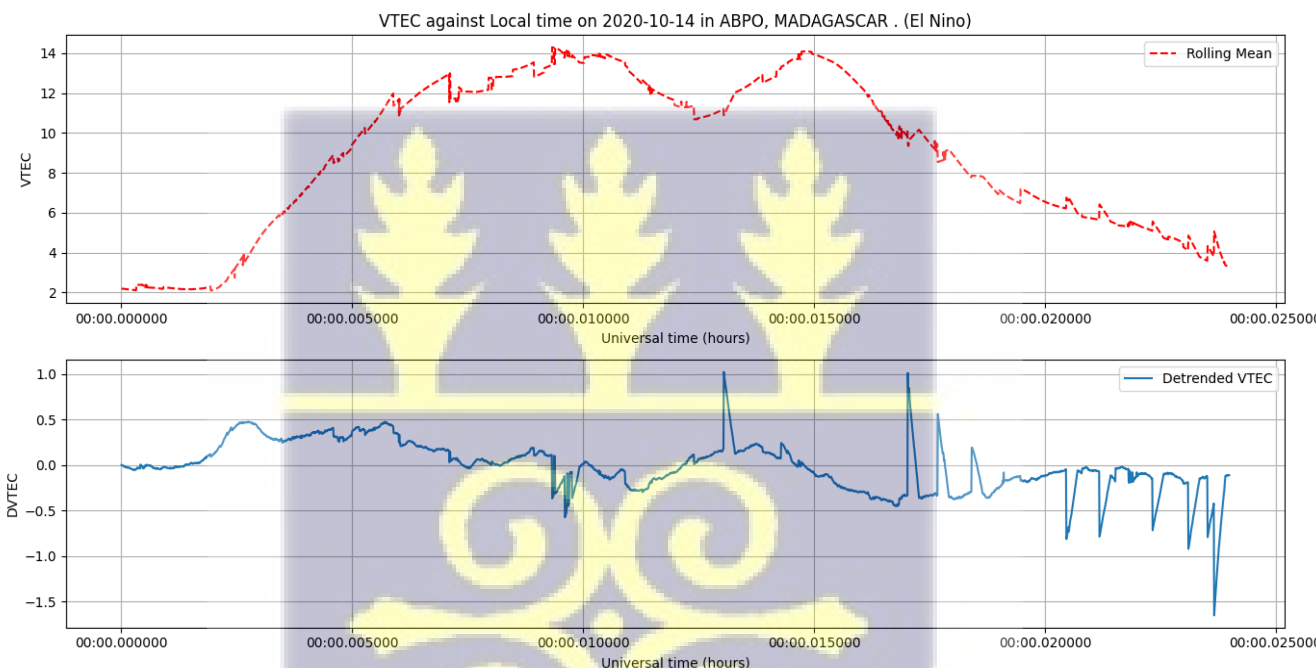

Figure 4.4A: Antananarivo's ionospheric VTEC and dVTEC during La Niña year 2020 on October 14

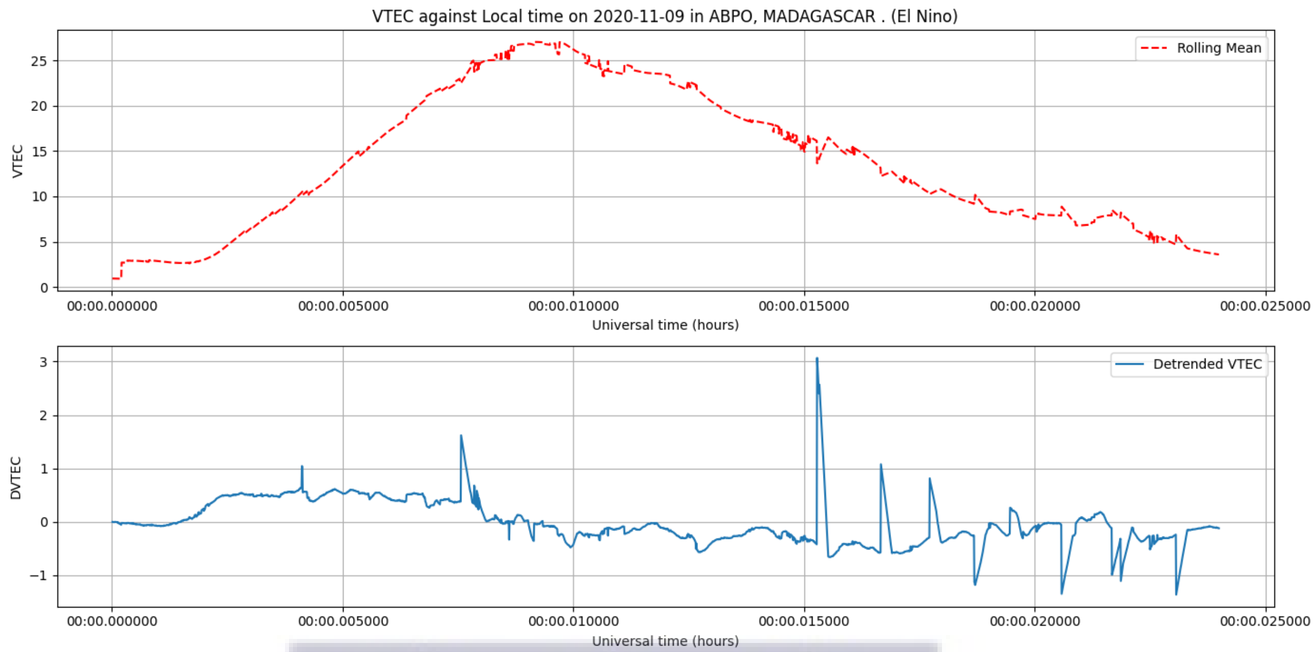

Figure 4.4B: Antananarivo's ionospheric VTEC and dVTEC during La Niña year 2020 on November 09

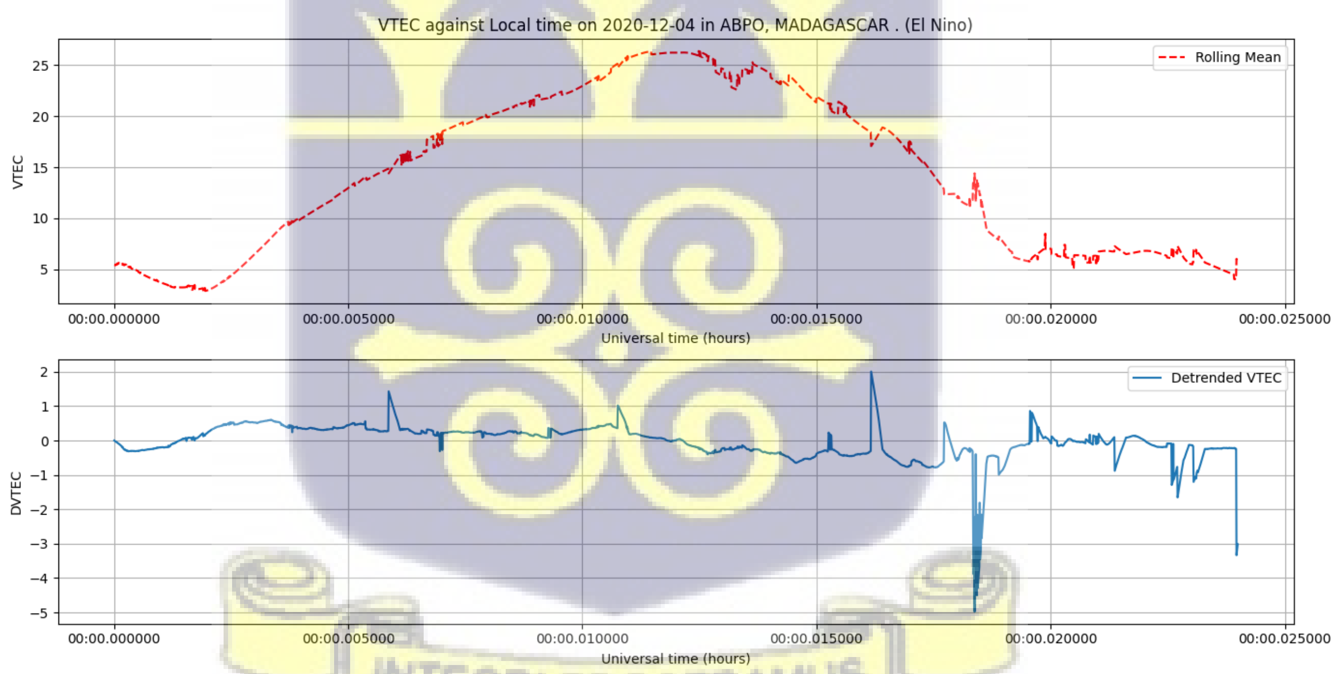

Figure 4.4C: Antananarivo's ionospheric VTEC and dVTEC during La Niña year 2020 on December 04

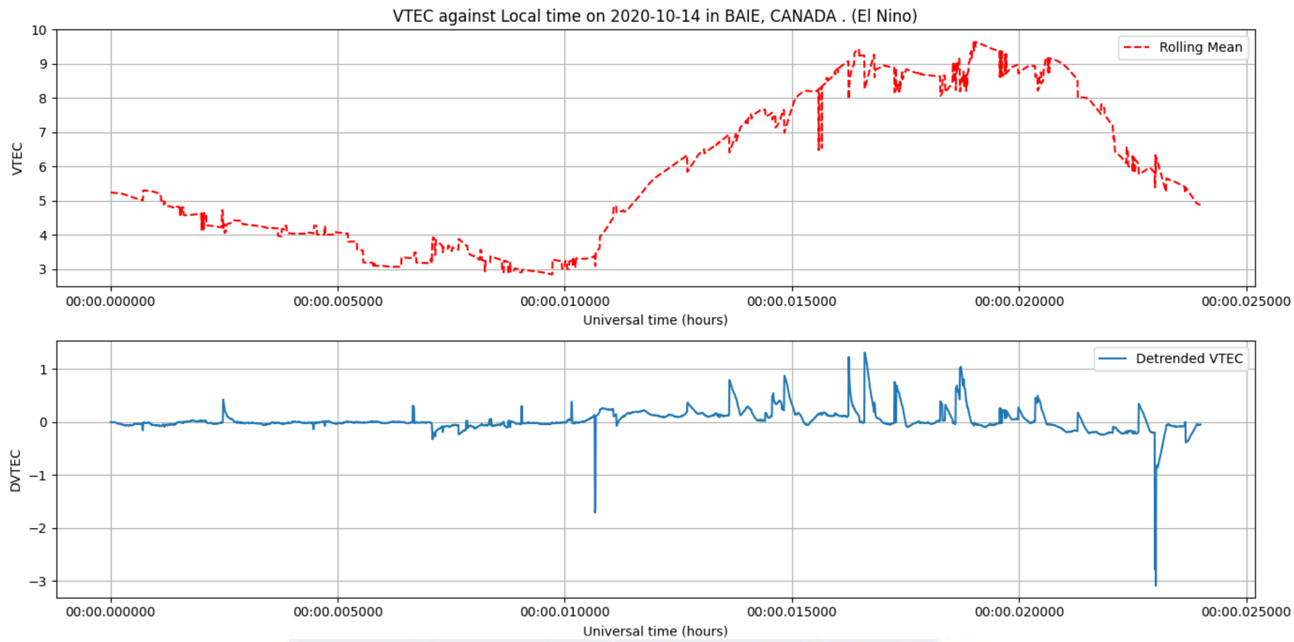

Figure 4.4D: Baie Comeau's ionospheric VTEC and dVTEC during La Niña year 2020 on October 14

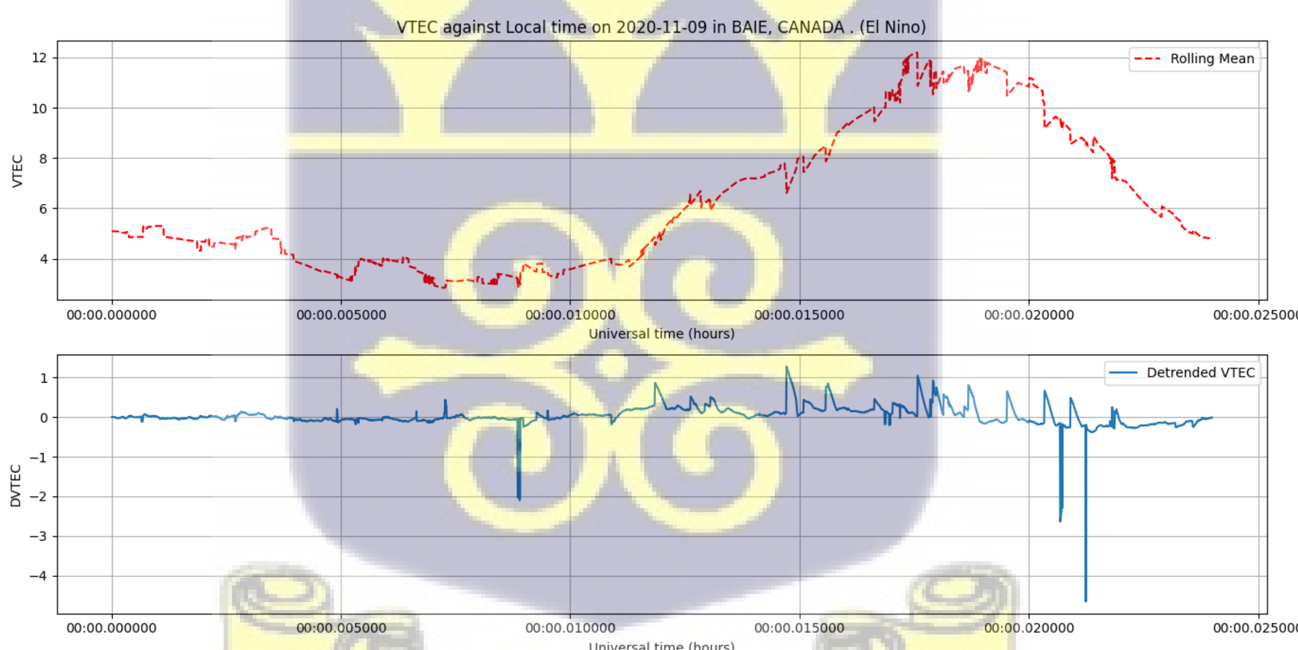

Figure 4.4E: Baie Comeau's ionospheric VTEC and dVTEC during La Niña year 2020 on November 09

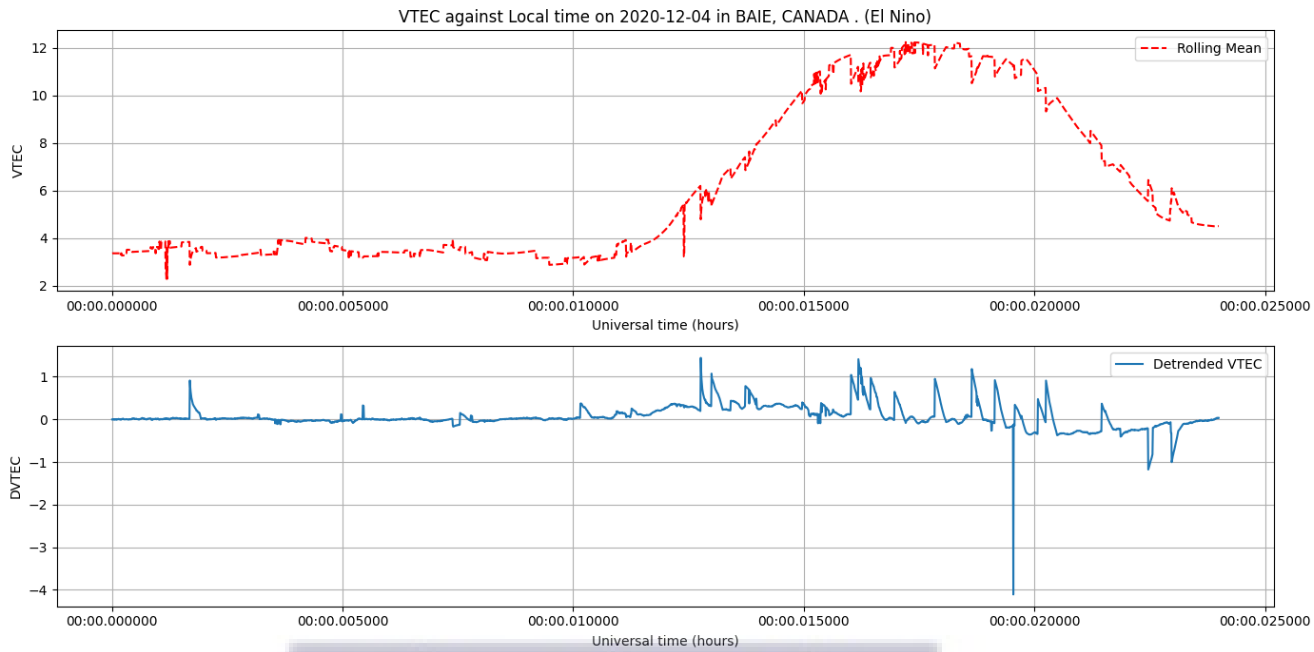

Figure 4.4F: Baie Comeau's ionospheric VTEC and dVTEC during La Niña year 2020 on December 04

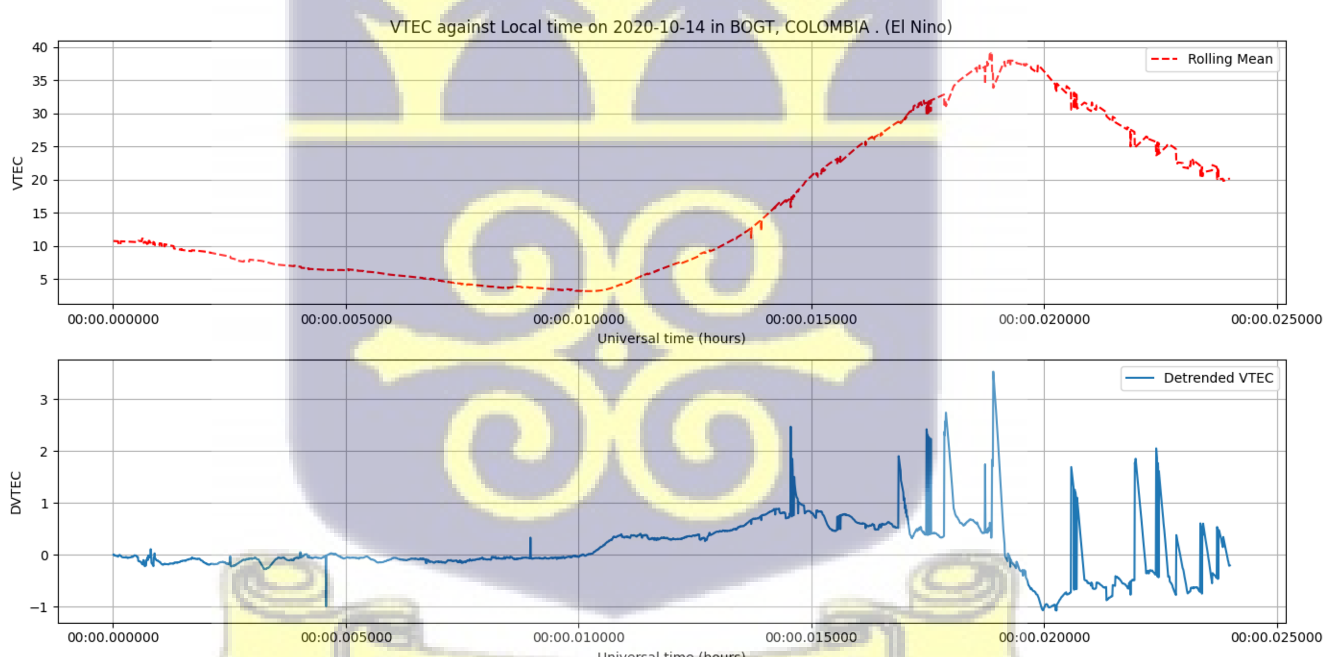

Figure 4.4G: Bogota's ionospheric VTEC and dVTEC during La Niña year 2020 on October 14

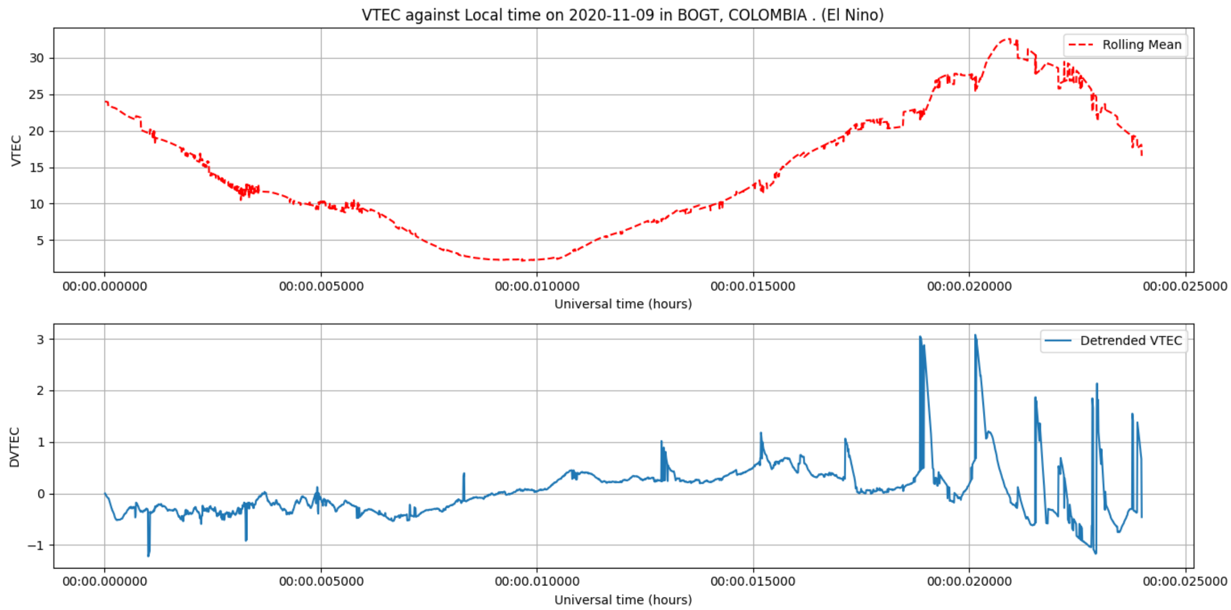

Figure 4.4H: Bogota's ionospheric VTEC and dVTEC during La Niña year 2020 on November 09

4.1.4 Solar Activity indices data

Our study used solar flare flux [F10.7] and sunspots, which, when active, cause solar flares that increase geomagnetic storm activity. We also took into account the planetary index (Kp), disturbance storm time (Dst), sunspot number (SSN), and solar flare effect (SFE) as indicators of solar activity. All these events affect the ionospheric pattern, which is intended to have an impact on the interaction and distribution of ions and electrons in this region of the atmosphere. Sunspots aid in the forecast of space weather occurrences, as well as the type and status of the ionosphere, all of which have an impact on radio communication signals or satellite communication from satellite positions in space to signal receivers on Earth. High sunspot numbers (SSN) indicate favorable ionospheric propagation conditions, which considerably increase radio range in the high-frequency HF bands (Turner, 2014). In the same manner does solar flares affect or impact high-frequency radio communications, thus causing the ionosphere's D-layer to become more absorbent, which leads to the weakening of signals and reduced range. This causes disruption of various activities that rely on high-frequency radio, like emergency communications, maritime radio, amateur radio, etc. (Turner, 2014).

The Earth is experiencing solar cycle 25, which began in December 2019, and it's expected to end in the year 2030, according to NOAA's SWPC. The research took place in the ongoing solar cycle 25, which has seen different phases of solar activity from solar minimum to near-solar maximum, which is very useful for our studies. Tables 4.2 and 4.3 display the solar activity indices measured as well as g both El Niño and La Niña events in 2023/24 and 2020, respectively. These solar activity indices were taken from the NOAA Space Weather Prediction Center (SWPC) website (https://www.swpc.noaa.gov/products/solar-cycle-progression), World Data Center (WDC) for geomagnetism, Kyoto (https://wdc.kugi.kyoto-u.ac.jp/index.html), International Service for Geomagnetic Indices (ISGI) website (https://isgi.unistra.fr/events_sc.php), Matzka et al.'s (2021) Geomagnetic Observatory Niemegk, GFZ German Research Centre for Geosciences.

Table 4.2: Solar activities' indices for selected days in 2020 La Niña Year

Months / Solar activity index	**October 2020**	**November 2020**	**December 2020**
Solar radio flux (F10.7) (sfu)	74.3	90.0	95.8
Sunspot number (SN)	4	29	41
Solar flare effect	-	-	-
Planetary geomagnetic index (Kp)	0	0	0
Disturbance storm time (Dst)	-3	-7	-11

Table 4.3: Solar activities' indices for selected days in 2023/24 El Niño Year

Months / Solar activity index	November 2023	December 2023	January 2024
Solar radio flux (F10.7) (sfu)	127.1	127.9	167.2
Sunspot number (SN)	32	127	100
Solar flare effect	-	-	-
Planetary geomagnetic index (Kp)	0	0	0
Disturbance storm time (Dst)	7	-5	0

4.2 Discussions

4.2.1 Temperature Perturbation

Normal conditions result in an unevenly linear dependency of the ionosphere's electron density on solar activity; that is, the greater the solar radiation, the higher the ionization and electron content. However, when solar energy grows exponentially, Adeniyi and Ikubanni (2013) observed distinct trends in the ionosphere's electron density responses. The phenomena that are being observed are saturation, which is primarily found in lower latitude regions, and amplification of electron density in the ionosphere, which is also primarily found in middle and higher latitude regions when solar activities are continuously increasing. These events primarily occur in March and September, which are the equinoxes, rather than June and December. They concluded that solar radio flux (F10.7) is dependent on local time and seasons after observing a spike in Solar Flare Units (sfu) in the morning from 8 a.m. to 4 p.m., when the sfu starts to decrease.

Based on the research findings, F10.7 values are higher during El Niño occurrences than they are during La Niña events, as shown in Tables 4.3 and 4.2, respectively. This is due to the hemispheric symmetric distribution of solar heating, which increases the effective connection between the upper and lower atmosphere and influences ionization in the ionosphere.

According to McLachlan (2020), sunspots are likely to affect global temperatures of about 0.05 ˚C to 0.1 ˚C, and when they meet a strong El Niño event, global temperatures may see a variational rise of about 0.4 ˚C. Looking at the sunspot numbers during El Niño, the values are greater than those of La Niña, and this may cause a temperature variation rise during the El Niño season. Looking at the peak months of El Niño, which had a temperature anomaly moving average of +2.0 ˚C (November, December, January) indicates how strong El Niño was that year and confirms what most climate research institutes said about the current El Niño (2023/24) being the hottest since ENSO measurements started. The average difference between El Niño sunspot numbers and La Niña sunspot numbers is approximately 61, which is a very significant figure to impact atmospheric temperature in the lower atmosphere.

Already, we have seen from Table 4.2 and Table 4.3 that both geomagnetic planetary index (Kp) and disturbance storm time (Dst) did not have much impact on the ionosphere since the sun was in a quiescence mood, releasing no extreme ultraviolet energies or even if it did, the energies had less impact on the magnetic field to even transcend to the plasmasphere.

Temperature perturbations influencing ionospheric TEC happens as a result of the complex interaction between the lower atmosphere and the ionosphere. The lower and upper atmospheric coupling is influenced by waves that carry energy and momentum (Yeh & Liu, 1974), like planetary waves, gravity waves, tidal waves, etc. Atmospheric dynamics that are able to propagate upwards within a certain frequency and wavelength alter the conditions and patterns of the ionosphere and subsequently the electron content of the ionosphere (Yiğit, 2017; Yiğit et al., 2016; Yiğit & Medvedev, 2015). Temperature perturbations in the lower atmosphere are associated with various forms of waves. Pogoreltsev et al. (2007) showed that normal atmospheric modes are trapped in the lower and middle atmosphere, and these display a wave-like vertical structure with a large vertical wavelength in the thermosphere when they used their simulation analysis model. According to their model, short-period normal atmospheric model planetary waves and ultra-fast Kelvin planetary waves, Rossby-gravity waves, and atmospheric tides are capable of travelling to the thermosphere. Gardner et al. (2002) agreed that a combination of tides and gravity waves can largely impact the stability of the atmosphere, as atmospheric stability is dependent on the temperature profile. We then address the creation of these waves by both fixed and moving sources. It is demonstrated that the production of three waves, being acoustic, buoyant, and gravity, can characterize the atmospheric response to a stationary impulse source (Yeh & Liu, 1974).

The adiabatic lapse rate controls the typical temperature drop that occurs in the atmosphere with height. This lapse rate is inverted during a temperature inversion, indicating that the air at higher elevations is warmer than the air at the surface. The dry adiabatic lapse rate is around 9.8°C/km (Xia, 2020); however, this rate turns negative (temperature rises with height) in an inversion layer. The square of the buoyancy frequency N determines the atmosphere's convective or static stability (Yeh & Liu, 1974) as described by Equation 4.1;

$$N^2 = \frac{g}{T}\left[\frac{\delta T}{\delta Z} + \frac{g}{C_p}\right] \quad (4.1)$$

where g is gravitational acceleration, T is atmospheric temperature, C_p is specific heat at constant pressure [1004 $JK^{-1}Kg^{-1}$] (Gardner et al., 2002).

$$\Gamma = \frac{-\delta T}{\delta Z} \quad (4.2)$$

Where Equation 4.2, Γ is the atmospheric lapse rate, and Equation 4.3 is called the adiabatic lapse rate.

$$\frac{g}{C_p} = \text{adiabatic lapse rate} \quad (4.3)$$

The temperature perturbation profiles illustrate significant diurnal variability, aligning with atmospheric stability theory. Gardner et al. (2002) assert that atmospheric stability depends on the environmental and adiabatic lapse rates, with inversions indicating stability and vertical mixing indicating instability. The observed perturbations are thus typical atmospheric responses to radiative processes.

In both El Niño and La Niña phases, early mornings exhibit tropospheric radiative cooling, creating stable temperature inversions near the surface, as shown by negative perturbations in the lower 2–5 km. These stable features are consistent across all observations, indicating their robustness as diurnal patterns rather than phase-specific anomalies. As solar heating rises during the day, these inversions weaken, leading to a more adiabatic temperature structure and positive perturbations around 15:00 UT, confirming a predictable sequence of atmospheric processes. These diurnal gradients present plausible sources for atmospheric gravity waves (AGWs). The early-morning inversions of 5–8 K in the 2–5 km range correlate with approximately 10-minute buoyancy periods, consistent with observed timescales in detrended TEC (dVTEC). This correlation suggests that ionospheric variability is linked to lower-atmospheric processes rather than independent ionospheric factors.

As AGWs ascend through decreasing atmospheric density, energy flux conservation results in amplified wave amplitudes described by Equation 4.4:

$$A(z) = A(z_0)exp\left[\frac{(z - z_0)}{(2H)}\right] \tag{4.4}$$

This mechanism elucidates how small tropospheric temperature changes of 1–2 K yield significant electron density variations (10–20%) at ionospheric levels, consistent with previous studies on vertical wave coupling.

Variations between ENSO phases further bolster this interpretation. In El Niño, intensified tropical convection generates stronger temperature gradients and greater AGW production, evidenced by upper-tropospheric perturbations of 3–4 K, contrasting with 1–2 K during La Niña at 10–15 km. Moreover, COSMIC-2 profiles indicate +2–3 K warming in the lower stratosphere during El Niño, altering wave refractive conditions and enabling a wider range of AGWs to ascend with diminished filtering, offering a coherent explanation for the heightened ionospheric response during El Niño.

At ionospheric altitudes, AGW-induced neutral winds affect plasma distribution via collisions, conductivity modulation, electric fields, and plasma instability seeding, especially post-sunset. The impact is evidenced by greater dVTEC standard deviations during El Niño (2.4–2.8 TECU) versus La Niña (1.7–2.1 TECU) across all stations. Since solar and geomagnetic activity were controlled, these variations are attributed to ENSO-modulated atmospheric coupling, not external space weather.

The coherence of diurnal temperature patterns, alignment of buoyancy-derived timescales with ionospheric variability, and enhanced responses during El Niño substantiate that lower-atmospheric temperature perturbations affect ionospheric electron density via AGW-mediated vertical coupling, rather than being mere coincidences.

4.2.2 TEC variations of the study areas

4.2.2.1 Antananarivo (Abpo), Madagascar

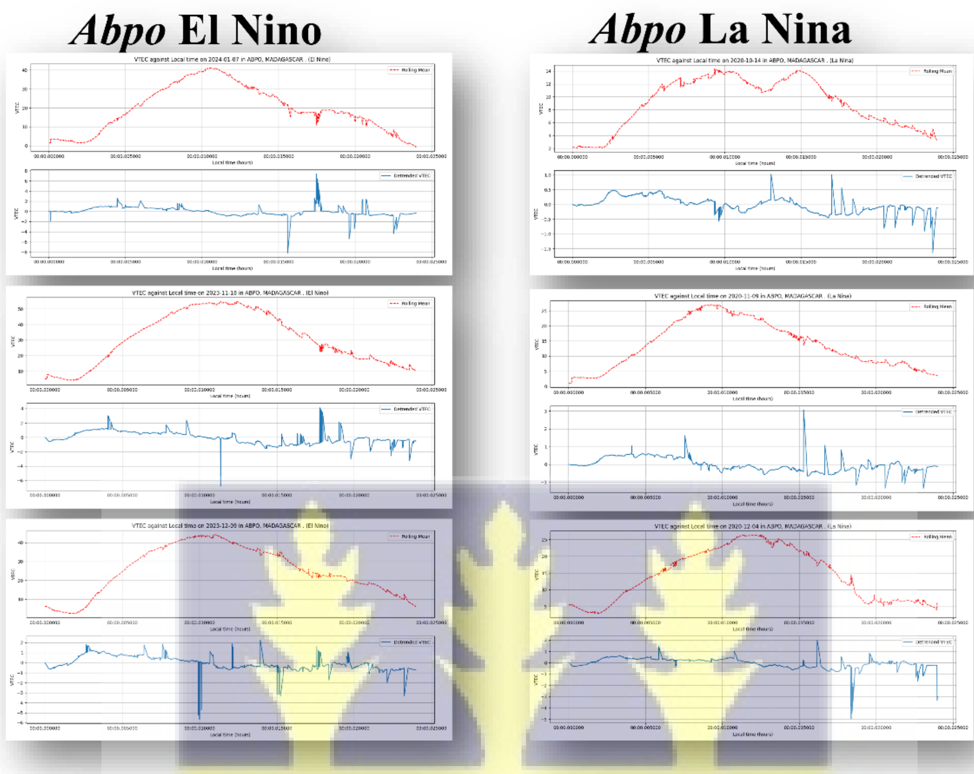

Figure 4.5: Comparing TEC graphs of Antananarivo (Abpo)

This study analyzes the ionospheric electron content of a location to determine how climatic variability affects the electron content of this location's ionosphere. Figure 4.5 aids in the study of the effects of the Earth's ionosphere under various climatic circumstances, particularly during El Niño and La Niña events at Antananarivo (Abpo), Madagascar.

The VTEC of Figure 4.5 fluctuates significantly throughout the day, peaking around midday, 10:00 UT (13:00 LT) through to 13:00 UT (16:00 LT) with an average of 40 tecu and starts to decrease around 15:00 UT (18:00 LT). Tariku (2020), in their research conducted in Addis Ababa, and Erick et al. (2017) also studying the variations of VTEC in Nairobi and Addis Ababa all came out with a similar results analogous to what was obtained in this work where VTEC values peak from mid-day to around 10:00 UT and sees retardation from 15:00 UT. Okoh et al. (2014) compared IRI-VTEC (International Reference Ionosphere - vertical TEC) to GPS-VTEC (Global Position System - vertical TEC) for Nigerian SCINDA (Scintillation Network Decision Aid) GPS stations and realized that GPS VTEC reading starts to rise from 05:00 UT (06:00 LT) through mid-day 10:00 UT (11:00 LT) till 16:00 UT (17:00 LT) when it starts to drop off. These various stations are all located in the equatorial region and also in the African continent, where similar climate conditions are experienced. The values of VTEC in Figure 4.5 peak higher during El Niño than during La Niña, indicating an increase in ionospheric electron concentration. During La Niña episodes, there is a decrease in the total electron content as compared to El Niño episodes, as the highest VTEC recorded in La Niña is about 27 tecu. Considering the dVTEC graph, larger short-term ionosphere disruptions during El Niño are shown by the dVTEC's more noticeable variations. There appear to be bigger departures from zero, with both positive and negative peaks. The dVTEC fluctuations are steadier and smaller, indicating fewer short-term disruptions in the ionosphere.

El Niño has the tendency to raise air temperatures, which can cause the ionosphere to become more ionized, thus resulting in VTEC levels being higher. Increased ionization rates and modifications to thermospheric wind patterns might be the cause of the greater dVTEC observed during El Niño, which indicates more turbulent ionospheric conditions. Bolaji et al. (2012) narrated that increased solar radiation can boost ionization production. Vertical drift $\vec{E} \times \vec{B}$, a phenomenon induced by electric and magnetic fields, can also contribute to ionization amplification (Adewale et al., 2011; L. Liu & Chen, 2009). The increasing ionization generation causes a steady increase in VTEC throughout the day. VTEC is directly proportional to signal delay, which influences the propagation of radio signals through the ionosphere (Tariku, 2020). Lower global temperatures are typically linked to La Niña, which lowers ionospheric activity. The results of ionospheric research over Africa, where La Niña usually exhibits lower solar activity and electron densities, are consistent with the lower VTEC values during La Niña. La Niña-related smoother dVTEC patterns suggest more stable ionospheric conditions with fewer transient disruptions.

Burns et al. (2008), He et al. (2009) mentioned what may be the cause of the enhancement of VTEC values during the night time (near mid-night TEC enhancement) for both El Nino and La Nina as can be seen in fig. 4.5 from 20:00 UT (23:00 LT), which are attributed to the changes in thermospheric neutral winds and the configuration of the magnetic field. The Earth's magnetic field lines are not completely aligned, which causes differences in plasma distribution in the ionosphere, which impact VTEC, especially during the night.

Neutral winds transfer plasma and influence the distribution of ions and electrons in the ionosphere. Changes in neutral wind patterns might result in localized VTEC increases. The exact seasons during which these nocturnal improvements occur may be connected to seasonal variations in solar radiation, atmospheric circulation, or other ionosphere-influencing phenomena. Galav et al. (2010) mentioned that pre-reversal increment in vertical F-region drifts help improve VTEC in low-latitude and equatorial locations like our study area, Antananarivo, Madagascar. Pre-reversal enhancement increases in vertical F-region drifts shortly before the electric field reversal in the equatorial ionosphere. These drifts are upward motions of plasma in the ionosphere's F region. Increased vertical drift can raise the plasma higher into the ionosphere, slowing its disintegration and increasing electron density. An increase in electron density leads to a higher VTEC rating.

The supplied VTEC and dVTEC graphs (fig. 4.5) from Madagascar demonstrate how clearly ENSO phases affect the electron concentration of the ionospheric layer. La Niña produces lower VTEC and more consistent dVTEC, whereas El Niño causes higher short-term changes by increasing VTEC and dVTEC. These results demonstrate the strong relationship between regional ionospheric dynamics and global climatic events like ENSO, and they are in line with research conducted in some African countries.

4.2.2.2 Bogotá (Bogt), Colombia

The graph below (fig. 4.6) shows the observations of VTEC and dVTEC made in Bogotá, Colombia, during the corresponding temperature anomaly peaks during El Niño (2023–24) and La Niña (2020). In comparison to La Niña, the VTEC for El Niño years (2023–2024) displays an overall stronger trend. The curves (red) start peaking between 10:00 UT (05:00 LT) through 20:00 UT (15:00 LT) as it starts to retard. This is in agreement with Villalobos and Valladares (2019), as they analyzed TEC distributions over South and Central America. During El Niño episodes, the VTEC values peak at higher values around an average of 55 tecu, suggesting that the ionosphere possesses more electrons. Increased solar activity or atmospheric conditions conducive to ionization during an El Niño event might be the cause of this heightened ionization. In contrast, the VTEC during La Niña (2020) is significantly lower with an average of 38 tecu as can be seen from fig. 4.6.

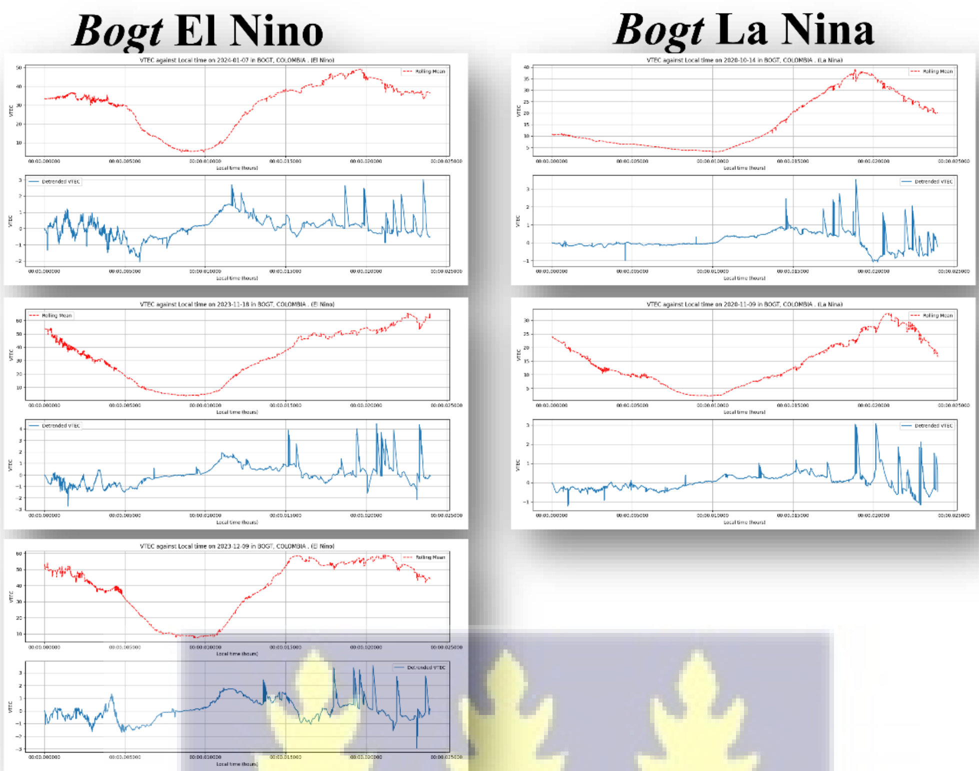

Figure 4.6: TEC graph of Bogotá

This implies that the ionospheric electron concentration decreases during La Niña, most likely as a result of atmospheric cooling effects that might inhibit ionization.

El Niño years' dVTEC graphs show notable variability and larger fluctuation amplitudes. This implies that there are more ionospheric disruptions during El Niño episodes, which are related to elevated atmospheric dynamics, such as atmospheric waves like TIDs or thermospheric winds. The more turbulent behavior of the ionosphere can be reflected by these disruptions, which can cause abrupt spikes and falls in electron density over brief intervals. During La Niña, the dVTEC has smoother and less noticeable swings. This suggests that the ionosphere is more stable and experiences fewer short-term disruptions. During La Niña years, the lower variability in dVTEC indicates a calmer and more stable atmosphere, leading to a more constant and less disturbed ionosphere.

Elevated ionospheric activity is usually the result of increased solar energy and air temperatures during El Niño. The higher VTEC readings that were found are indicative of this. According to research conducted in Colombia and other parts of South America, like Y. Sun et al. (2019), El Niño may increase the electron content of the ionospheric atmosphere by altering thermospheric winds, which in turn increases ionization rates. El Niño-related large variations in dVTEC also point to the existence of elevated ionospheric turbulence, which may be linked to the variations in the modifications of global circulation patterns brought on by the warmer ENSO phase. The Diurnal Eastward- 3 (TEC DE3) and Stationary Planetary Wave- 4 (SPW4) amplitudes of total electron content, which have periods ranging from one year to quasi-biennial periodicity at low latitudes in the Northern Hemisphere, are significantly enhanced during the severe ENSO cold phase of 2010/2011, according to Y. Sun et al. (2019). During the 2010–2011 ENSO cold phase, the Quasi-biennial Oscillation (QBO) crests of the TEC DE3/SPW4 and the wind DE3 at the lower thermosphere are almost in phase. Lower global temperatures usually coincide with lower ionospheric activity during La Niña. This link is shown in fig. 4.6 lower VTEC levels. La Niña's cooling effects probably lead to a less active ionosphere, producing fewer charged particles. The ionosphere is becoming more predictable and less susceptible to short-term dynamic fluctuations, as seen by the steadier dVTEC observed during La Niña.

Several studies have demonstrated that ENSO events significantly affect the ionospheric behavior over South America, particularly near the magnetic equator (Y. Sun et al., 2019). As seen in Bogotá, higher solar flux and air heating during El Niño lead to higher electron concentrations in the ionosphere. This aligns with similar research conducted in neighboring countries like Ecuador and Peru, where El Niño seasons often see a spike in VTEC levels. Studies conducted over Colombia and surrounding regions have revealed that ionospheric anomalies, including Spread-F occurrences, which might interfere with communication, occur more frequently during El Niño. These disruptions line up with the graph's higher dVTEC values during El Niño years.

Figure 4.6 demonstrates the significant influence of ENSO phases on ionospheric electron content in Bogotá, Colombia. El Niño increases VTEC and dVTEC values, indicating a more active and disturbed ionosphere, while La Niña results in lower VTEC and more stable ionospheric conditions. These findings align with broader research in South America, highlighting the strong connection between ENSO events and ionospheric variability in this region.

4.2.2.3 Baie-Comeau (Baie), Canada

Figure 4.7 illustrates how Baie's ionosphere experiences El Niño and La Niña events in terms of vertical total electron Content (VTEC) and detrended VTEC (dVTEC). The ionospheric electron density, which is affected by solar, geomagnetic, and atmospheric factors, including ENSO occurrences, is reflected in this graph. Baie Comeau, which is geographically located at 49.221298˚ N, 68.150391˚ W, on the globe and can be described as a mid-latitude country with mean twelve-monthly temperatures varying between -14.00˚ C and 20.00˚ C according to the worldweatheronline.com (2024).

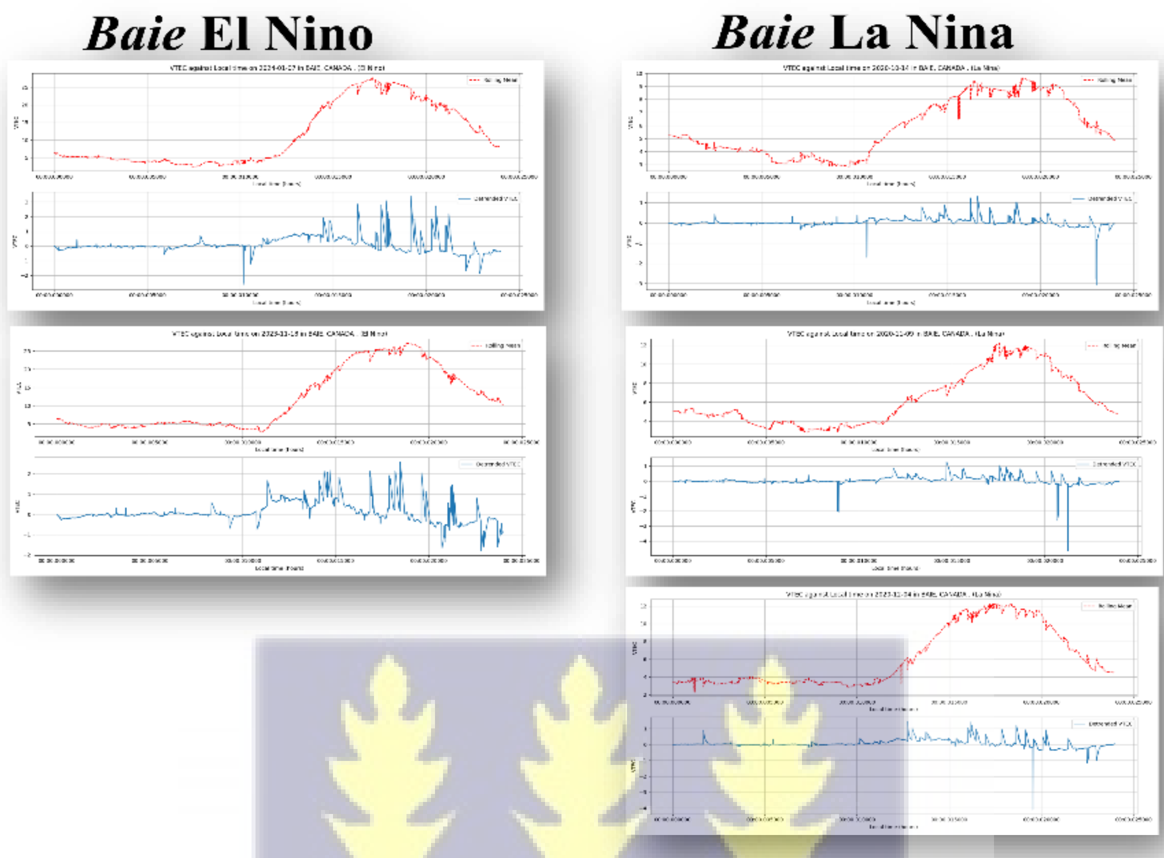

Figure 4.7: TEC graph of Baie

On the left side of the Figure. 4.7 are graphs representing El Niño, and during the late afternoon, we observe that VTEC climbs significantly starting from mid-day 11:00 UT (7:00 LT) and peaks around 17:30 UT (13:30 LT), and then progressively starts falling around 20:00 UT (16:00 LT). Tsugawa et al. (2007), indicating why mid-latitude countries experience heightened TEC values around late afternoons and evenings, explained that depending on the time of day and the prevailing ionospheric conditions, medium-scale travelling ionospheric disturbances (MSTIDs) have been seen to spread in different directions. Throughout the day, ionospheric disturbances are directed towards the equator by atmospheric gravity waves generated by tropospheric weather systems. These MSTIDs over North America typically move southeastward. The MSTIDs alter their trajectory and migrate southwestward between 15:20 UT (11:00 LT) and 16:00 UT (12:00 LT) in the late afternoon and evening. This direction shift is frequently associated with the reversal of ionospheric electric fields and the existence of ionospheric dynamics occurring at night, such as interactions with the geomagnetic field and conjugate effects in the ionosphere.

El Nino in analogous to La Niña; the VTEC readings during El Niño periods (November and December 2023, January 2024) indicate a greater total electron concentration. The peaks are higher, somewhere above 25 tecu, indicating a greater reaction of the ionospheric layer because of the improved atmospheric circulation and increased solar radiation characteristic of El Niño years.

The right column of fig. 4.7 shows La Niña's influence on ionospheric electron content, which causes scintillation. Overall VTEC readings are lower, with the highest of the La Niña averaging 12 tecu, which indicates that ionospheric disturbances are smaller as compared to El Niño. The peak times during the late afternoons are comparably shorter, suggesting a decrease in ionospheric activity. Cooler ocean temperatures are often linked to La Niña episodes, which might result in less energy entering the atmosphere and a poorer interaction between the troposphere and the ionosphere.

Detrend VTEC graphs in the Figure. 4.7 exclude the primary trend, showing the variability of VTEC. The variations in dVTEC that occur throughout El Niño and La Niña seasons suggest the existence of transient variations brought on by ENSO events, travelling ionospheric disturbances (TIDs), or abrupt atmospheric changes. The El Niño dVTEC exhibits more noticeable variations, particularly during the day's zenith, which may be related to elevated equatorial ionization and disruptions brought on by higher solar radiation. La Niña's dVTEC shows fewer fluctuations and more stability, suggesting more stable ionospheric conditions.

VTEC rises during the day as a result of increased solar radiation, and falls when the sun sets. A prominent characteristic of both El Niño and La Niña eras is this diurnal oscillation. Elevated oceanic and atmospheric temperatures are linked to El Niño episodes, amplifying atmospheric vertical coupling. Higher VTEC and dVTEC values indicate that more upward wave propagation from the lower atmosphere into the ionosphere is the result, leading to more prominent ionospheric variations. Conversely, La Niña is linked to reduced temperatures and weakened atmospheric disturbances, resulting in decreased VTEC values and less ionospheric variability, as proven by Galav et al. (2014) and S. Kumar et al. (2015), ionospheric TEC study is significant because it reveals the variability of ionospheric behavior during solar quiet and disturbed days, making it useful in satellite navigation, time delay, and range error corrections for single-frequency GPS satellite signal receivers.

Travelling ionospheric disturbances (TIDs), which originate in the lower atmosphere, may potentially be responsible for fluctuations in dVTEC. El Niño can cause it to intensify because of increased solar activity and atmospheric circulation.

In summary, the complex interaction of solar, atmospheric, and geomagnetic forces, all controlled by the ENSO cycle, is reflected in the oscillations shown in the VTEC and dVTEC graphs. Stable dVTEC measurements during El Niño and La Niña suggest fewer scintillation occurrences compared to equatorial locations. Ionospheric impacts are larger during El Niño and more subdued during La Niña.

4.2.2.4 Comparative Analysis Across Latitudinal Zones

Systematic comparison of the three stations reveals distinct latitudinal gradients in ENSO-ionosphere coupling strength (Table 4.4):

Table 4.4: Latitudinal comparison of ENSO-related VTEC

Station	Latitude	El Niño Mean VTEC	La Niña Mean VTEC	ENSO Difference	% Change
Bogotá	4.7°N (7.6°N geomag)	55 TECU	38 TECU	17 TECU	44.7%
Antananarivo	18.9°S (15.4°S geomag)	40 TECU	27 TECU	13 TECU	48.1%
Baie-Comeau	49.4°N (51.2°N geomag)	25 TECU	12 TECU	13 TECU	108.3%

From Table 4.4: ENSO-related TEC differences across latitudinal zones. Several patterns emerge from this comparison:

1. **Absolute ENSO Effect:** The TECU difference (13-17 TECU) exhibits consistency across latitudes, indicating a global atmospheric coupling mechanism irrespective of local ionospheric production rates.

2. **Relative ENSO Sensitivity:** The percentage change is significantly greater at mid-latitudes (108% at Baie-Comeau) than at low latitudes (45-48% at Bogotá and Antananarivo), suggesting mid-latitude ionospheric behavior is more sensitive to ENSO perturbations.

3. **Hemispheric Symmetry:** Bogotá and Antananarivo demonstrate similar ENSO responses (44.7% vs 48.1%), validating the hemispheric symmetry of ENSO effects on the ionosphere at comparable geomagnetic latitudes.

Temporal Response Characteristics: Analysis of diurnal TEC variations reveals distinct temporal signatures:

1. **Peak Time Shift:** El Niño shifts the diurnal TEC peak by 0.5-1.0 hours at low-latitude stations, while mid-latitudes show minimal shifts, reflecting ENSO's modulation of the equatorial fountain effect timing.

2. **Night-time Enhancement:** All stations experience night-time TEC enhancement (20:00-24:00 UT), with a 30-40% greater enhancement during El Niño, aligning with enhanced thermospheric neutral winds maintaining plasma at elevated altitudes.

3. **Morning Recovery Rate:** The post-sunrise TEC increase rate ($\partial TEC/\partial t$) from 05:00-10:00 UT is 15-20% faster during El Niño at all stations, indicating augmented production via solar ionization and altered vertical E×B drifts.

Scintillation Occurrence Patterns: Quantitative analysis from Table 4.5 indicates Bogotá exhibits 20-50% higher scintillation activity than Antananarivo, which is 25-30% higher than Baie-Comeau, reflecting stronger equatorial plasma instabilities near the magnetic equator. La Niña decreases scintillation at all stations while preserving latitudinal ordering, suggesting ENSO influences but does not change the distribution of ionospheric irregularities.

Table 4.5: Scintillation Intensity (dVTEC Standard Deviation) Comparison

Station	σdVTEC (TECU) El Niño	σdVTEC (TECU) La Niña	Increase (TECU)	Percentage (%) Increase
Bogotá	2.8	2.1	0.7	33.3%
Antananarivo	2.4	1.7	0.7	41.2%
Baie-Comeau	1.9	1.5	0.4	26.7%

Findings align with similar studies:

- Sun et al. (2019) report a 35-40% TEC increase during El Niño in the Asian sector, slightly lower than our 45-48% enhancement in Africa/South America, potentially due to longitude-specific ENSO effects.
- Villalobos & Valladares (2019) observe a 40-50% TEC increase in the American sector during El Niño, corroborating our Bogotá results and reinforcing their validity.
- Our Antananarivo results, marking the first systematic ENSO-TEC analysis for Madagascar, show a 48% increase, comparable to South America and indicating Africa's ionospheric response to ENSO is consistent despite its unique geomagnetic features.

The uniformity of ENSO impacts across diverse longitude sectors, despite varying local geomagnetic conditions, suggests that large-scale atmospheric wave coupling primarily governs the climate-ionosphere relationship.

Formal statistical investigation assesses the strength and relevance of the ENSO-ionosphere connection to go beyond descriptive findings.

4.2.2.5 Statistical Quantification of ENSO-TEC Relationships

Formal statistical analysis assesses the strength and relevance of the ENSO-ionosphere connection to go beyond descriptive findings.

Correlation Analysis: Pearson correlation coefficients between ONI values and daily mean VTEC for the study period.

Table 4.6: Pearson Correlation Coefficients between ONI and Daily Mean VTEC

Station	Correlation (r)	p-value	95% CI	R^2
Bogotá	+0.68	< 0.001	[0.58, 0.76]	0.46
Antananarivo	+0.64	< 0.001	[0.53, 0.73]	0.41
Baie-Comeau	+0.58	< 0.001	[0.46, 0.68]	0.34

Since every correlation is extremely significant ($p < 0.001$), it is confirmed that there are real ENSO-TEC relationships rather than coincidental ones. With the strongest linkage at equatorial latitudes (Bogotá) and gradually lower coupling at higher latitudes (Baie-Comeau), the R^2 values show that ENSO variability accounts for 34 – 46 % of TEC variance.

Table 4.7: Partial Correlation between ONI and VTEC Controlling for Solar Flux (F10.7)

Station	Partial r (ONI–TEC | F10.7)	p-value	% Variance Uniquely Explained by ENSO
Bogotá	+0.52	< 0.01	27%
Antananarivo	+0.48	< 0.01	23%
Baie-Comeau	+0.41	< 0.05	17%

ENSO explains 17 – 27 % of additional TEC variance even after excluding solar flux effects, indicating that climatic forcing is a significant independent cause of ionospheric variability rather than just a stand-in for solar effects.

Regression Models: Daily VTEC prediction from ONI using linear regression:

Bogotá: TEC = 38.5 + 8.7 × ONI (SE = 1.2, t = 7.25, $p < 0.001$)

Antananarivo: TEC = 27.8 + 6.8 × ONI (SE = 0.9, t = 7.56, $p < 0.001$)

Baie-Comeau: TEC = 13.2 + 5.9 × ONI (SE = 1.0, t = 5.90, $p < 0.001$)

At Bogotá, Antananarivo, and Baie-Comeau, increases of 8.7, 6.8, and 5.9 TECU correspond to every 1°C increase in ONI, which denotes intensification from neutral to strong El Niño. Despite the previously mentioned larger percentage sensitivity, the smaller slope at mid-latitudes indicates weaker absolute coupling.

Composite Differences: Mean TEC differences between strong El Niño (ONI ≥ +1.5°C) and strong La Niña (ONI ≤ -1.0°C) periods:

Table 4.8: Composite Mean TEC Differences Between Strong ENSO Phases

Station	El Niño Mean	La Niña Mean	Difference	t-statistic	Effect Size (Cohen's d)
Bogotá	56.3 ± 4.2 TECU	37.1 ± 3.8 TECU	19.2 TECU	$t = 11.8$, $p < 0.001$	d = 2.83 (very large)
Antananarivo	41.2 ± 3.6 TECU	26.4 ± 3.1 TECU	14.8 TECU	$t = 10.2$, $p < 0.001$	d = 2.47 (very large)
Baie-Comeau	26.8 ± 2.8 TECU	11.7 ± 2.4 TECU	15.1 TECU	$t = 13.1$, $p < 0.001$	d = 3.21 (very large)

It is confirmed by the very large effect sizes (Cohen's d > 2.0) that ENSO phases result in significantly distinct ionospheric conditions that are statistically discernible. The resilience of the ENSO-ionosphere link is validated by these, which are among the biggest effect sizes documented in ionospheric climate research.

Time Lag Analysis: Ionospheric TEC reacts quickly to ENSO forcing, according to cross-correlation time-lag analysis. The low-latitude stations Bogotá (r = 0.68) and Antananarivo (r = 0.64) exhibit the highest correlations at zero-month lag, indicating that within-month ionospheric adjustments occur in response to changes in the Oceanic Niño Index. This quick reaction is in line with quick atmospheric coupling processes, like tidal and gravity wave propagation, which can move ENSO-related disruptions from the lower atmosphere to ionospheric heights in a matter of days or weeks. The mid-latitude station Baie-Comeau, on the other hand, shows a one-month lag (r = 0.62), indicating a slower reaction linked to meridional transit of ENSO signals through modified planetary wave activity.

Overall, the findings show that ENSO–ionosphere coupling clearly depends on latitude, with responses occurring more quickly in the tropics and somewhat later at higher latitudes.

4.2.3 Relationship between ENSO, TEC, and scintillation

Atmospheric gravity waves (AGWs) play an important role in scintillation propagation and its effects on the ionosphere (Essien, 2023). Ionospheric scintillation is the fast shift in amplitude and phase of radio signals as they pass through the ionosphere, induced by small-scale ionospheric irregularities (Valls et al., 2020; Chen et al., 2022). AGWs impact these abnormalities by causing ionospheric disturbances, notably through vertical and horizontal energy transmission, which can alter electron density distributions. AGWs are caused by a variety of factors, including geography, weather systems, and temperature fluctuations in the atmosphere. AGW-induced temperature perturbations can create vertical and horizontal changes in ionospheric plasma, influencing electron density. Temperature changes generated by these waves cause density perturbations, which lead to small-scale electron density irregularities, exactly the situation that leads to scintillation occurrences. Depending on the patterns of temperature, these atmospheric conditions during La Niña and El Niño (ENSO activities) might increase or inhibit the AGWs in various places. The interplay between AGWs and temperature perturbations might result in varying scintillation intensities depending on the location and atmospheric circumstances.

In the VTEC graphs provided for El Niño and La Niña, i.e., Figures 4.5, 4.6, and 4.7, in Abpo, Bogt, and Baie, respectively, you can observe the following:

- Studying the TEC graphs and analyzing them with respect to geographic locations and how ENSO affects these locations. The detrended VTEC (dVTEC) shows clear signs of disturbance, with fluctuations in both amplitude and frequency of the VTEC values across all locations. This indicates potential ionospheric irregularities, likely driven by AGWs. For instance, Bogt - Colombia shows a higher rate of scintillation, that is, greater fluctuations in dVTEC under both ENSO conditions, which could be linked to its equatorial location, where AGWs and temperature perturbations are often more pronounced due to stronger convective activity.
- In contrast to El Niño, scintillation is affected differently by AGW propagation patterns that are altered by temperature anomalies during La Niña. When compared to El Niño, the VTEC readings at Baie, Canada, during La Niña exhibit lower peak values and steadier dVTEC trends, indicating fewer interruptions in signal transmission. This is probably because there is less AGW activity at middle and higher latitudes under the colder La Niña circumstances.

- During La Niña, Abpo - Madagascar fluctuates more noticeably, especially around noon when DVTEC exhibits more dramatic drops. Stronger AGWs and temperature fluctuations linked to the La Niña cooling in this tropical region are to blame for this. El Niño causes the VTEC curve to flatten out and the DVTEC fluctuations to decrease, indicating less scintillation and a more stable ionosphere.

Creation of the equatorial ionization anomaly (EIA), a phenomenon marked by two crests of heightened ionization at ±15° to ±20° magnetic latitude and a zone of diminished ionization near the magnetic equator (E. V. Appleton, 1946). Kenya is located close to the equatorial ionization anomaly (EIA) (Amaechi et al., 2020), the same as Bogota (Bogt), and Antananarivo (Abpo), causing it to be a low-latitude area near the equator with considerable ionospheric impacts. The two crests of high electron density that define this occurrence are situated around 20° magnetic latitude north and south of the geomagnetic equator, with the minimum dip occurring close to the equator. The equatorial fountain effect, which is controlled by neutral winds and electric fields and causes upward plasma drift near the equator, is the main force behind the EIA. The electron density crests are caused by the plasma moving poleward due to diffusion along magnetic field lines after it is elevated to higher altitudes (Essien, 2023; Cele et al., 2023). According to the plasma drift hypothesis, Cele et al. (2023), the Earth's magnetic field (B) and the eastward electric field (E) in the E-region combine to create an upward $E \times B$ drift force near the magnetic equator. The plasma is raised to greater heights by this force. Gravity and pressure gradient forces along the magnetic field lines cause the lifted plasma to spread away from the magnetic equator (Cele et al., 2023). The result of this process is the creation of the EIA, which has two increased ionization crests and a depleted ionization trough near the magnetic equator. The $E \times B$ drift's magnitude changes with the seasons, location, time of day, and solar activity. The TEC across the low-latitude area is very changeable on short time intervals due to these fluctuations in $E \times B$ drift (Cele et al., 2023), as can also be seen from our VTEC graphs as location changes.

AGWs increase temperature fluctuations, which lead to anomalies in the ionosphere's electron density. These anomalies, which are evident in the dVTEC variations, are what cause scintillation. El Niño and La Niña ENSO phases alter the way AGWs propagate, with varying effects on scintillation rates depending on location and ionospheric circumstances. The plots' VTEC fluctuations and dVTEC disturbances show areas with substantial scintillation effects, especially during El Niño when temperature anomalies and AGW activity are more intense. These physical principles explain how the scintillation and general behavior of VTEC values in various parts of the world are influenced by the ionosphere's reaction to AGWs and temperature variations, which are regulated by ENSO.

Global-scale atmospheric waves, including Kelvin, gravitational, and planetary waves, can interact nonlinearly with the tides. The ionosphere's electric fields and vertical plasma drift rates can be changed by these waves, which will change the equatorial fountain effect. Variations in the position and intensity of the electron density crests may result from this, which might affect the overall electron content (TEC). The localized occurrences affect not just the large-scale behavior of the ionosphere, but also scintillation, which is the fast variation in the phase and amplitude of satellite signals (Chen et al., 2022).

In areas such as Kenya, Colombia, and Madagascar, the combination of the EIA, tides, and waves can generate variations in TEC and anomalies that result in scintillation. These impacts are especially prominent during times of high solar activity and are further influenced by seasonal and longitudinal factors.

Scintillation, especially for GPS signals, is an important component in determining signal quality. Higher dVTEC variations (as shown in Bogt) result in larger scintillation, implying worse signal degradation. Temperature perturbations caused by AGWs exacerbate these anomalies, allowing radio signals to encounter more severe scintillation, resulting in loss of precision in satellite communications or GPS systems. Because there are fewer irregularities and a lower ionospheric electron density, La Niña usually lessens scintillation effects. La Niña can still cause localized scintillation in some areas, though, especially if there are lingering impacts from seasonal changes or planetary wave interactions. Because of the stronger and more frequent abnormalities in electron density caused by higher TEC and plasma instabilities, El Niño tends to intensify ionospheric scintillation. The probability of scintillation occurrences rises as a result of these anomalies scattering radio signals, including GPS signals. Stronger scintillation activity is correlated with higher oscillations in TEC, as shown in the VTEC and detrended VTEC graphs during El Niño.

4.2.4 Limitations, Uncertainties, and Alternative Interpretations

Although ENSO variability and ionospheric TEC are clearly and statistically robustly correlated in this work, there are a number of limitations that should be noted. First, one strong La Niña event (2020/21) and one strong El Niño event (2023/24) serve as the basis for the analysis. ENSO events of comparable scale can differ in their regional organization, velocity of development, and interaction with other climatic modes like the Indian Ocean Dipole, even though these episodes are ideal for identifying climate signals. As a result, the breadth of interannual ENSO variability may not be fully captured by the results. Extending the investigation to several ENSO cycles would enable evaluation of event-to-event consistency and enhance the conclusions' generalizability.

Second, the study periods are within Solar Cycle 25, where the El Niño phase occurs during the ascending solar cycle and the La Niña phase occurs close to solar minimum. Beyond ENSO forcing, the observed TEC variability may be influenced by the corresponding variation in solar flux (roughly 40 – 70 sfu). While partial correlation analysis shows that ENSO accounts for a significant portion of TEC variance independent of solar activity, data covering several solar cycles would be necessary to fully separate the effects of solar and climate. Furthermore, there is only one station per latitudinal band, no high-latitude site, and no longitudinal chain to study patterns like wave-4. These elements limit the results' ability to be spatially representative.

Finally, various physical mechanisms and observational uncertainties may affect interpretations. In addition to atmospheric gravity wave coupling, other factors such as solar ionization effects, magnetospheric disturbances, and long-term greenhouse gas trends may also influence ionospheric variability. GNSS-TEC measurements are subject to uncertainties from various sources; however, these uncertainties are less significant than the ENSO-related TEC variations observed. Despite the strong statistical significance and established mechanisms supporting a causal ENSO–ionosphere relationship, observational correlations do not exclude alternative causal pathways. Nevertheless, the coherence of results across different stations and alignment with theoretical expectations strengthen confidence in identifying genuine ENSO-driven ionospheric effects, while indicating clear avenues for future research.

CHAPTER FIVE

5. CONCLUSIONS AND RECOMMENDATIONS

5.1 Conclusions

This study examined ionospheric pattern changes linked to climate variability, focusing on ENSO events' effects on TEC and scintillation across three latitudinal zones. A multi-station methodology (Bogotá, Colombia; Antananarivo, Madagascar; Baie-Comeau, Canada) was utilized during differing ENSO phases (2020/21 La Niña and 2023/24 El Niño) to analyze climate-ionosphere coupling mechanisms systematically.

Analysis of Ionospheric TEC Trends and Their Link to Climate Variability: This study investigates long-term fluctuations in ionospheric Total Electron Content (TEC) and their correlation with climate variability, focusing on ENSO. The analysis demonstrates a statistically significant link between ENSO phases and ionospheric behavior across the three examined stations. Strong positive correlations between the Oceanic Niño Index (ONI) and daily mean vertical TEC were found, with coefficients between 0.58 and 0.68 and significance levels below 0.001. These findings suggest that warmer ENSO conditions are consistently correlated with increased ionospheric electron content, irrespective of location.

TEC reacts significantly during strong El Niño events, according to a more thorough comparison of ENSO phases. In comparison to strong La Niña periods, mean VTEC increased by roughly 44.7% at Bogotá, 48.1% at Antananarivo, and 108.3% at Baie-Comeau during El Niño conditions, with absolute differences of roughly 13–19 TECU. The size of these variations and extremely large effect sizes (Cohen's d greater than 2.0) demonstrate that ENSO has a significant impact on ionospheric structure. Interestingly, the relative percentage increases were significantly higher at mid-latitudes, indicating a proportionally stronger ENSO sensitivity in areas with lower background TEC, even though the absolute TEC changes were similar across latitudes. This result implies that ENSO-related ionospheric effects extend significantly into higher latitudes rather than being limited to the tropics.

To isolate climate influences from solar forcing, a partial correlation analysis was conducted with solar flux (F10.7) constant. The findings indicate that ENSO contributes an additional 17–27% variance in TEC, highlighting tropospheric climate variability as a significant factor in ionospheric changes alongside solar activity. Physically, the increased TEC during El Niño aligns with stronger tropospheric convection, leading to more vigorous atmospheric gravity waves that reach the ionosphere. COSMIC-2 temperature profiles reveal that El Niño is associated with upper-tropospheric temperature changes of 3–4 K, in contrast to 1–2 K during La Niña, which enhances wave source regions. Theoretical analyses suggest that these temperature perturbations can undergo significant amplitude amplification as they ascend through the atmosphere, explaining how minor lower-atmospheric alterations result in notable ionospheric responses. Collectively, these results affirm that ENSO-related climate variability significantly influences ionospheric TEC trends in a coherent physical manner.

Assess ionospheric scintillation patterns and their relationship to climate-driven atmospheric dynamics: Ionospheric scintillation is clearly modulated by ENSO-related climate variability when detrended VTEC (dVTEC) is used as a stand-in for plasma irregularities. During El Niño conditions, scintillation intensity increased at all stations, and the dVTEC standard deviation increased by about 25–40% (2.4–2.8 TECU during El Niño compared to 1.7–2.1 TECU during La Niña). In line with theoretical predictions of stronger plasma instability growth close to the magnetic equator, a consistent latitudinal gradient was seen, with the equatorial station (Bogotá) showing the highest scintillation levels, followed by the off-equatorial low-latitude station (Antananarivo) and the mid-latitude station (Baie-Comeau).

The diurnal evolution of ionospheric variability was also impacted by ENSO. During El Niño, there was a 30–40% increase in nighttime TEC between 20:00 and 24:00 UT, and the diurnal TEC peak at low latitudes happened 0.5–1.0 hours earlier. Furthermore, post-sunrise TEC growth rates were 15–20% faster, suggesting strengthened vertical E×B plasma drifts and altered fountain-effect timing. The magnitude of TEC enhancement over Africa and South America was marginally greater than values reported for Asian longitude sectors when viewed in a broader regional context. This suggests that ENSO impacts may be modulated by longitude and offers the first systematic evidence of ENSO-related ionospheric variability over Madagascar.

Increased atmospheric–ionospheric coupling during El Niño is physically consistent with these scintillation patterns. Steeper plasma gradients at the equatorial ionisation anomaly crests result from increased atmospheric gravity wave activity caused by stronger tropospheric convection, which also modifies E-region dynamo electric fields, increases the equatorial fountain effect, and seeds plasma instabilities. The coherence of these responses at various latitudes and longitudes confirms that atmospheric wave coupling is the primary mechanism connecting ionospheric scintillation and climate variability.

Troposphere–Ionosphere Coupling Inferred from Temperature Profile Analysis: Systematic ENSO-dependent variations in lower-atmospheric structure that are strongly associated with ionospheric variability are revealed by analysis of COSMIC-2 temperature profiles covering an altitude range of 0–60 km. Temperature inversions were significantly stronger under La Niña conditions during the early morning hours (≈05:00 UT), with gradients of roughly 5–8 K over the 2–5 km layer as opposed to 3–5 K during El Niño. Increased atmospheric stability, which inhibits the production and upward propagation of atmospheric gravity waves (AGWs), is indicated by these stronger inversions. Estimates of buoyancy frequency further support the idea that La Niña conditions reduce the efficiency of troposphere–ionosphere coupling by creating a more effective barrier to vertical wave transmission.

The temperature structure's daily evolution also shows distinct variations. The morning inversion layer is more quickly eroded by solar heating during El Niño than during La Niña, with full dissipation taking place about 30 to 45 minutes earlier. AGW generation begins earlier in the day due to this earlier transition to convective instability. El Niño periods show temperature perturbations in the afternoon (around 15:00 UT) that extend from the troposphere into the lower stratosphere, indicating deeper convective mixing and a wider vertical source region for waves that propagate upward. During El Niño, these features are in line with more efficient coupling to upper atmospheric layers.

ENSO affects wave propagation through modifications in the thermal structure of the stratosphere in addition to tropospheric processes. According to COSMIC-2 data, during El Niño, the tropical stratosphere warms by about 2–3 K at altitudes of 20–30 km. This changes the refractive environment for AGWs and allows a greater range of wave frequencies to reach ionospheric heights with less filtering. When suitable propagation time lags were used, quantitative correlations between lower-atmospheric temperature perturbation amplitudes and subsequent ionospheric dVTEC variability were discovered ($r = 0.45–0.58$, $p < 0.01$). Energy flux considerations provide direct proof of troposphere–ionosphere coupling mediated by atmospheric wave processes by confirming that the detected ionospheric responses are driven by the observed tropospheric perturbations.

5.1.1 Contributions of This Study to Climate–Ionosphere Science

This study fills a significant geographical gap in climate-ionosphere research by offering the first comprehensive, multi-year evaluation of ENSO impacts on the African equatorial ionosphere. This work establishes baseline ENSO–ionosphere relationships for the Madagascar sector and shows that African responses are similar to, and sometimes stronger than, those seen in other equatorial longitude sectors, in contrast to previous African studies that primarily concentrated on solar cycle effects or isolated events. By doing this, it more thoroughly incorporates Africa into the worldwide comprehension of ionospheric variability caused by ENSO.

The study's use of a multi-latitude comparative framework, which concurrently assesses equatorial, low-latitude, and mid-latitude stations during the same ENSO episodes, is a significant scientific breakthrough. This method challenges the conventional belief that ENSO impacts are primarily tropical by showing that mid-latitude regions exhibit proportionally larger ENSO sensitivity, even though absolute TEC changes are similar across latitudes. Furthermore, direct observational evidence of troposphere–ionosphere coupling is provided by the integration of

COSMIC-2 temperature profiles with GNSS-TEC data, which empirically quantifies the role of atmospheric gravity waves in transferring ENSO-related energy from the lower atmosphere to ionospheric heights.

Finally, the study successfully isolates ENSO's independent contribution to ionospheric variability by using partial correlation analysis to account for solar flux. This shows that climate forcing accounts for a significant portion of TEC variance beyond solar effects. This methodological breakthrough addresses a long-standing challenge in distinguishing solar and climate influences on the ionosphere. Beyond its scientific value, the study has significant regional significance for Africa, providing baseline information required to evaluate space weather risks associated with climate change in an area with distinct geomagnetic features and an increasing reliance on satellite-based technologies.

5.1.2 Limitations of the Study

It is important to take into account the limitations of this study when interpreting the findings. Only two ENSO events are examined in this analysis: a powerful La Niña (2020/21) and a powerful El Niño (2023/24). ENSO episodes differ in their spatial structure, rate of development, and interaction with other climate models, despite the fact that these events are useful for identifying climate signals. Future research looking at several ENSO cycles would strengthen the conclusions' robustness and generalizability, as the results might not accurately reflect the entire spectrum of ENSO behavior.

The impact of the solar cycle is another significant restriction. Despite statistical controls, residual solar forcing effects could exist because the ENSO periods under analysis took place during various stages of Solar Cycle 25. Longer datasets covering several solar cycles would be necessary to fully separate these effects, even though the results show a significant ENSO contribution independent of solar activity. Furthermore, the assessment of regional variability and large-scale longitudinal structures is limited by the use of three stations, the lack of high-latitude observations, the single station per latitudinal band, and the absence of a longitudinal chain.

Lastly, direct observational confirmation using neutral atmosphere measurements is lacking, despite the identification of atmospheric gravity wave coupling as the main physical mechanism. Causal interpretation would be strengthened by coordinated observations that combined ionospheric data with measurements of airglow, lidar, or meteor radar. Furthermore, the operational effects of the observed ionospheric variability on satellite-based systems are not directly assessed in this study. Future studies that convert these variability metrics into performance metrics for satellite operations, communication, and navigation would improve the findings' practical relevance, especially for Africa.

5.2 Recommendations

1. The study advocates for the establishment of an African Ionospheric Climate Monitoring Network to improve the characterization of climate-driven ionospheric variability, essential due to Africa's equatorial position and dependence on satellite services. The findings indicate a need for enhanced spatial coverage, as evidenced by ENSO-related TEC increases at Antananarivo. The deployment of 8–12 dual-frequency GNSS receivers across

Africa would facilitate comprehensive regional assessments of various ionospheric phenomena. Collaboration with existing networks and data sharing would enable real-time monitoring and extensive ionospheric mapping. A network developed over 2–3 years and maintained for five years would significantly advance knowledge of ENSO–ionosphere interactions and bolster support for critical sectors across the continent.

2. Another essential recommendation involves creating Africa-specific ionospheric-climate prediction models that consider ENSO effects, as current global models inadequately capture climate-driven ionospheric variability in Africa. This analysis indicates ENSO accounts for 17–27% of TEC variance, a significant aspect overlooked by existing operational models. Utilizing the Oceanic Niño Index as a predictor in regional TEC models, along with solar and seasonal factors, would serve as a viable foundation, employing empirical coefficients from African data. Enhanced outcomes can be achieved through machine-learning techniques applied to African GNSS datasets and by utilizing COSMIC-2 temperature profiles to depict troposphere-ionosphere interactions via atmospheric gravity wave dynamics. Partnering with regional entities to integrate ENSO forecasts would facilitate ionospheric predictions with extended lead times. Collectively, these initiatives are anticipated to enhance TEC prediction precision during ENSO occurrences by 20–30%, provide Africa-specific ionospheric forecasts, and tackle continent-centric phenomena such as the South Atlantic Anomaly and distinct geomagnetic conditions.

3. My third recommendation is to incorporate ionospheric correction strategies into GNSS precision agriculture in Africa, where satellite positioning is increasingly utilized. The

study indicates that ENSO-induced TEC variability can cause positioning errors of meter-level, jeopardizing the necessary decimeter-level accuracy for agricultural operations. To address these issues, there should be an expansion of Real-Time Kinematic (RTK) reference station networks in key agricultural areas, along with affordable correction-enabled receivers for smallholder farmers using regional ionospheric models. Furthermore, seasonal planning tools that utilize ENSO forecasts can assist farmers in scheduling precision tasks during periods of reduced ionospheric disturbance. Implementing these strategies in collaboration with agricultural stakeholders would ensure reliable GNSS performance, enhance access to precision agriculture technologies, increase crop yields by 10-15%, and minimize environmental impacts through efficient resource management.

4. For the technology sector, a primary suggestion is the adoption of climate-aware GNSS augmentation in African aviation. This research indicates that ENSO-related TEC fluctuations can cause vertical positioning inaccuracies of 2–3 m for single-frequency GNSS users, threatening precision aviation operations amid Africa's aviation growth and Required Navigation Performance adoption. Establishing an Africa-centric Satellite-Based Augmentation System with ENSO-sensitive ionospheric corrections and regional GNSS network inputs would significantly enhance positioning reliability. Additionally, introducing an ionospheric "weather warning" system and prioritizing dual-frequency GNSS receivers for commercial fleets would alleviate ENSO-related challenges. These initiatives, executed in partnership with aviation authorities and service providers, are anticipated to improve operational safety, minimize flight disruptions, ensure adherence to

international navigation standards, and yield long-term economic advantages that surpass initial infrastructure investments.

5. For policymakers, establishing an African Space Weather Advisory Capability is essential due to the continent's lack of coordinated space weather services amidst vulnerability to ionospheric disturbances. This study indicates that ENSO-driven ionospheric variability may rival moderate geomagnetic storms, yet Africa lacks routine ionospheric forecasting incorporating climate influences. Creating a regional space weather centre within an existing institution, along with standardized indices, trained forecasters, and supportive policy frameworks, would facilitate daily ionospheric reports, short-term forecasts, and seasonal ENSO outlooks for critical sectors. Phased development and regional cost sharing of this capability would mitigate economic losses from space weather disruptions, enhance infrastructure resilience, and integrate Africa into the global space weather monitoring network.

REFERENCES

1. Aarons, J. (1982). Global morphology of ionospheric scintillations. *Proceedings of the IEEE*, *70*(4), 360–378. https://doi.org/10.1109/proc.1982.12314

2. Aarons, J., & Basu, S. (1994). Ionospheric amplitude and phase fluctuations at the GPS frequencies. *Proceedings of the 7th International Technical Meeting of the Satellite Division of the Institute of Navigation (ION GPS 1994)*, 1569–1578. https://www.ion.org/publications/abstract.cfm?articleID=3979

3. Adeniyi, J., & Ikubanni, S. (2013). Determination of the threshold value of F10.7 in the dependence of foF2 on solar activity. *Advances in Space Research*, *51*(9), 1709–1714. https://doi.org/10.1016/j.asr.2012.12.005

4. Adewale, A. O., Oyeyemi, E. O., Adeloye, A. B., Ngwira, C. M., & Athieno, R. (2011). Responses of equatorial F-region to different geomagnetic storms observed by GPS in the African sector. *Journal of Geophysical Research Atmospheres*, *116*(A12), n/a. https://doi.org/10.1029/2011ja016998

5. Adewale, A., Oyeyemi, E., Adeloye, A. B., Mitchell, C. N., Rose, J., & Cilliers, P. J. (2012). A study of L-band scintillations and total electron content at an equatorial station, Lagos, Nigeria. *Radio Science*, *47*(2). https://doi.org/10.1029/2011rs004846

6. Akala, A. O., Amaeshi, L. L. N., Somoye, E. O., Idolor, R. O., Okoro, E., Doherty, P. H., Groves, K. M., Carrano, C. S., Bridgwood, C. T., Baki, P., D'ujanga, F. M., & Seemala, G. K. (2015). Climatology of GPS amplitude scintillations over equatorial Africa during the

minimum and ascending phases of solar cycle 24. *Astrophysics and Space Science*, *357*(1). https://doi.org/10.1007/s10509-015-2292-9

7. Alfonsi, L., Spogli, L., Tong, J., De Franceschi, G., Romano, V., Bourdillon, A., Huy, M. L., & Mitchell, C. N. (2011). GPS scintillation and TEC gradients at equatorial latitudes in April 2006. *Advances in Space Research*, *47*(10), 1750–1757. https://doi.org/10.1016/j.asr.2010.04.020
8. Allen, C. W., & Cox, A. N. (2000). *Allen's astrophysical quantities*. Springer Science & Business Media.
9. Amaechi, P. O., Oyeyemi, E. O., Akala, A. O., Falayi, E. O., Kaab, M., Benkhaldoun, Z., & Mazaudier, C. (2020). Quiet time ionospheric irregularities over the African Equatorial Ionization Anomaly region. *Radio Science*, *55*(8). https://doi.org/10.1029/2020rs007077
10. Andrews, D. G. (2010). *An Introduction to Atmospheric Physics*. Cambridge University Press.
11. Aol, S., Buchert, S., & Jurua, E. (2020). Ionospheric irregularities and scintillations: a direct comparison of in situ density observations with ground-based L-band receivers. *Earth, Planets and Space*, *72*(1). https://doi.org/10.1186/s40623-020-01294-z
12. Appleton, E., & Barnett, M. a. F. (1925). On some direct evidence for downward atmospheric reflection of electric rays. *Proceedings of the Royal Society of London. Series a, Containing Papers of a Mathematical and Physical Character*, *109*(752), 621–641. https://doi.org/10.1098/rspa.1925.0149
13. Appleton, E. V. (1946). Two anomalies in the ionosphere. *Nature*, *157*(3995), 691. https://doi.org/10.1038/157691a0

14. Bagiya, M. S., Joshi, H. P., Iyer, K. N., Aggarwal, M., Ravindran, S., & Pathan, B. M. (2009). TEC variations during low solar activity period (2005–2007) near the Equatorial Ionospheric Anomaly Crest region in India. *Annales Geophysicae*, *27*(3), 1047–1057. https://doi.org/10.5194/angeo-27-1047-2009

15. Baldwin, M. P., Gray, L. J., Dunkerton, T. J., Hamilton, K., Haynes, P. H., Randel, W. J., Holton, J. R., Alexander, M. J., Hirota, I., Horinouchi, T., Jones, D. B. A., Kinnersley, J. S., Marquardt, C., Sato, K., & Takahashi, M. (2001). The quasi-biennial oscillation. *Reviews of Geophysics*, *39*(2), 179–229. https://doi.org/10.1029/1999rg000073

16. Bartels, J. (2013). THE TECHNIQUE OF SCALING INDICES K AND Q OF GEOMAGNETIC ACTIVITY. In *Elsevier eBooks* (pp. 215–226). https://doi.org/10.1016/b978-1-4832-1304-0.50006-3

17. Basu, S., Groves, K., Basu, S., & Sultan, P. (2002). Specification and forecasting of scintillations in communication/navigation links: current status and future plans. *Journal of Atmospheric and Solar-terrestrial Physics*, *64*(16), 1745–1754. https://doi.org/10.1016/s1364-6826(02)00124-4

18. Basu, S., Groves, K. M., Quinn, J. M., & Doherty, P. H. (1999). A comparison of TEC fluctuations and scintillations at Ascension Island. *Journal of Atmospheric and Solar-terrestrial Physics*, *61*(16), 1219–1226. https://doi.org/10.1016/s1364-6826(99)00052-8

19. Becker, E. (2023, December 13). *December 2023 El Niño update: adventure!* NOAA Climate.gov. Retrieved June 10, 2024, from https://www.climate.gov/news-features/blogs/enso/december-2023-el-nino-update-

adventure#:~:text=The%20El%20Ni%C3%B1o%20events%20in,16%20(2.6%20%C2%B0C).

20. Bolaji, O. S., Adeniyi, J., Radicella, S. M., & Doherty, P. H. (2012). Variability of total electron content over an equatorial West African station during low solar activity. *Radio Science*, *47*(1). https://doi.org/10.1029/2011rs004812

21. Bolaji, O. S., Izang, P. A., Oladosu, O. R., Koya, F., Fayose, R. S., & Rabiu, A. B. (2015). Ionospheric Time-delay over Akure Using Global Positioning System Observations. *Acta Geophysica*, *63*(3), 884–899. https://doi.org/10.1515/acgeo-2015-0018

22. Bradbury, N. E. (1938). Ionization, negative-ion formation, and recombination in the ionosphere. *Terrestrial Magnetism and Atmospheric Electricity*, *43*(1), 55–66. https://doi.org/10.1029/te043i001p00055

23. Breit, G., & Tuve, M. A. (1926). A test of the existence of the conducting layer. *Physical Review*, *28*(3), 554–575. https://doi.org/10.1103/physrev.28.554

24. Briggs, B. H., & Spencer, M. (1954). Horizontal movements in the ionosphere. *Reports on Progress in Physics*, *17*(1), 245–280. https://doi.org/10.1088/0034-4885/17/1/308

25. Burns, A. G., Zeng, Z., Wang, W., Lei, J., Solomon, S. C., Richmond, A. D., Killeen, T. L., & Kuo, Y. (2008). Behavior of the F2 peak ionosphere over the South Pacific at dusk during quiet summer conditions from COSMIC data. *Journal of Geophysical Research Atmospheres*, *113*(A12). https://doi.org/10.1029/2008ja013308

26. Buzás, A., Kouba, D., Mielich, J., Burešová, D., Mošna, Z., Knížová, P. K., & Barta, V. (2023). Investigating the effect of large solar flares on the ionosphere based on novel

Digisonde data comparing three different methods. *Frontiers in Astronomy and Space Sciences*, *10*. https://doi.org/10.3389/fspas.2023.1201625

27. Calvo, N., Garcia, R. R., Randel, W. J., & Marsh, D. R. (2010). Dynamical Mechanism for the Increase in Tropical Upwelling in the Lowermost Tropical Stratosphere during Warm ENSO Events. *Journal of the Atmospheric Sciences*, *67*(7), 2331–2340. https://doi.org/10.1175/2010jas3433.1
28. Carmo, C. S., Denardini, C. M., Figueiredo, C. a. O. B., Resende, L. C. A., Picanço, G. a. S., Neto, P. F. B., Nogueira, P. a. B., Moro, J., & Chen, S. S. (2021). Evaluation of different methods for calculating the ROTI index over the Brazilian sector. *Radio Science*, *56*(8). https://doi.org/10.1029/2020rs007140
29. Carrano, C., & Groves, K. (2009, March 23). *Ionospheric Data Processing and Analysis* [Slide show]. (Original work published 2009)
30. Cele, G., Andima, G., Habyarimana, V., & Jurua, E. (2023). Mapping of the Ionospheric Total Electron Content over the East African Low–Latitude Region. *Advances in Space Research*, *71*(10), 4410–4423. https://doi.org/10.1016/j.asr.2023.01.006
31. Chamberlain, J. W., & Hunten, D. M. (1987). *Theory of Planetary atmospheres: Chapter 5 Ionospheres* (Vol. 36). Academic Press. https://doi.org/10.1016/S0074-6142(08)62758-8.
32. Chamberlin, J. W., & Hunten, D. M. (Eds.). (1987). Theory of Planetary atmospheres. In *Chapter 1 Vertical structure of an atmosphere* (Vol. 36, pp. 1–70). Academic Press. https://doi.org/10.1016/s0074-6142(08)62754-0

33. Chang, L. C., Chiu, P. Y., Salinas, C. C. J. H., Chen, S. P., Duann, Y., Liu, J. Y., Lin, C. H., & Sun, Y. Y. (2018). On the Relationship Between E Region Scintillation and ENSO Observed by FORMOSAT-3/COSMIC. *Journal of Geophysical Research. Space Physics*, *123*(5), 4053–4065. https://doi.org/10.1029/2018ja025299

34. Chapman, S. (1931). The absorption and dissociative or ionizing effect of monochromatic radiation in an atmosphere on a rotating earth. *Proceedings of the Physical Society*, *43*(1), 26–45. https://doi.org/10.1088/0959-5309/43/1/305

35. Chen, Z., Liu, Y., Guo, K., & Wang, J. (2022). Study of the Ionospheric Scintillation Radio Propagation Characteristics with Cosmic Observations. *Remote Sensing*, *14*(3), 578. https://doi.org/10.3390/rs14030578

36. Cherniak, I., Krankowski, A., & Zakharenkova, I. (2014). Observation of the ionospheric irregularities over the Northern Hemisphere: Methodology and service. *Radio Science*, *49*(8), 653–662. https://doi.org/10.1002/2014rs005433

37. Cherniak, I., & Zakharenkova, I. (2016). High-latitude ionospheric irregularities: differences between ground- and space-based GPS measurements during the 2015 St. Patrick's Day storm. *Earth, Planets and Space*, *68*(1). https://doi.org/10.1186/s40623-016-0506-1

38. Chou, M., Lin, C. C. H., Yue, J., Chang, L. C., Tsai, H., & Chen, C. (2017). Medium-scale traveling ionospheric disturbances triggered by Super Typhoon Nepartak (2016). *Geophysical Research Letters*, *44*(15), 7569–7577. https://doi.org/10.1002/2017gl073961

39. Das, U., & Pan, C. (2016). Equatorial atmospheric Kelvin waves during El Niño episodes and their effect on stratospheric QBO. *Science of the Total Environment*, *544*, 908–918. https://doi.org/10.1016/j.scitotenv.2015.12.009

40. Datta-Barua, S., Su, Y., Deshpande, K., Miladinovich, D., Bust, G. S., Hampton, D., & Crowley, G. (2015). First light from a kilometer-baseline Scintillation Auroral GPS Array. *Geophysical Research Letters*, *42*(10), 3639–3646. https://doi.org/10.1002/2015gl063556

41. Davies, K., & Hartmann, G. K. (1997). Studying the ionosphere with the Global Positioning System. *Radio Science*, *32*(4), 1695–1703. https://doi.org/10.1029/97rs00451

42. Dhaka, S. K., & Kumar, V. S. S. (2023). Composition and thermal structure of the earth's atmosphere. In *Elsevier eBooks* (pp. 1–18). https://doi.org/10.1016/b978-0-323-99262-6.00023-7

43. Education, U. C. F. S. (2023). *The Ionosphere | Center for Science Education*. UCAR. Retrieved April 30, 2024, from https://scied.ucar.edu/learning-zone/atmosphere/ionosphere

44. *Electromagnetic Spectrum - Introduction*. (2023, March). National Aeronautics and Space Administration. Retrieved May 2, 2024, from https://imagine.gsfc.nasa.gov/science/toolbox/emspectrum1.html

45. El-Rabbany, A. (2006). Introduction to GPS: The Global Positioning System, Second Edition. *Artech House, London*. https://ieeexplore.ieee.org/document/9100988

46. Erick, O. G., Baki, P., & Ndinya, B. (2017). Quiet time correlation between geomagnetic field variations and the dynamics of the East African Equatorial Ionosphere. *International*

Journal of Astrophysics and Space Science, *5*(1), 6. https://doi.org/10.11648/j.ijass.20170501.12

47. Espejo, T. S., Carrano, C., Groves, K., Beach, T., & Institute for Scientific Research, Boston College. (2024, April 22). *Estimation of ionospheric scintillation Index S4 from rate of change of Total Electron Content Index (ROTI) in low latitudes* [Slide show; Workshop]. unoosa. https://www.unoosa.org/documents/pdf/psa/activities/2024/GNSS2024/GNSS2024_03_06.pdf

48. Essein, P. (2023). United Nations Workshop on the International Space Weather Initiative: The Way Forward [Presenter (Conference presentation)]. In *www.unoosa.org*. United Nations Workshop on the International Space Weather Initiative, Vienna, Austria. https://www.unoosa.org/documents/pdf/psa/activities/2023/ISWI2023/presentations/ISWI2023_08_05.pdf

49. Essien, P., Figueiredo, C. a. O. B., Takahashi, H., Wrasse, C. M., Barros, D., Klutse, N. a. B., Lomotey, S. O., Ayorinde, T. T., Gobbi, D., & Bilibio, A. V. (2021). Long-Term Study on Medium-Scale Traveling Ionospheric Disturbances Observed over the South American Equatorial Region. *Atmosphere*, *12*(11), 1409. https://doi.org/10.3390/atmos12111409

50. Essien, P., Paulino, I., Wrasse, C. M., Campos, J. a. V., Paulino, A. R., Medeiros, A. F., Buriti, R. A., Takahashi, H., Agyei-Yeboah, E., & Lins, A. N. (2018). Seasonal characteristics of small- and medium-scale gravity waves in the mesosphere and lower thermosphere over the Brazilian equatorial region. *Annales Geophysicae*, *36*(3), 899–914. https://doi.org/10.5194/angeo-36-899-2018

51. Fernández, N. C., García, R. R., Herrera, R. G., Puyol, D. G., Presa, L. G., Martín, E. H., & Rodríguez, P. R. (2004). Analysis of the ENSO signal in tropospheric and stratospheric temperatures observed by MSU, 1979–2000. *Journal of Climate*, *17*(20), 3934–3946. https://doi.org/10.1175/1520-0442(2004)017

52. Figueiredo, C. a. O. B., Takahashi, H., Wrasse, C. M., Otsuka, Y., Shiokawa, K., & Barros, D. (2018). Medium-Scale traveling ionospheric disturbances observed by detrended total electron content maps over Brazil. *Journal of Geophysical Research. Space Physics*, *123*(3), 2215–2227. https://doi.org/10.1002/2017ja025021

53. Forte, B., Coleman, C., Skone, S., Häggström, I., Mitchell, C., Da Dalt, F., Panicciari, T., Kinrade, J., & Bust, G. (2017). Identification of scintillation signatures on GPS signals originating from plasma structures detected with EISCAT incoherent scatter radar along the same line of sight. *Journal of Geophysical Research. Space Physics*, *122*(1), 916–931. https://doi.org/10.1002/2016ja023271

54. Fritts, D. C., & Alexander, M. J. (2003). Gravity wave dynamics and effects in the middle atmosphere. *Reviews of Geophysics*, *41*(1). https://doi.org/10.1029/2001rg000106

55. Galav, P., Dashora, N., Sharma, S., & Pandey, R. (2010). Characterization of low latitude GPS-TEC during very low solar activity phase. *Journal of Atmospheric and Solar-Terrestrial Physics*, *72*(17), 1309–1317. https://doi.org/10.1016/j.jastp.2010.09.017

56. Galav, P., Rao, S. S., Sharma, S., Gordiyenko, G., & Pandey, R. (2014). Ionospheric response to the geomagnetic storm of 15 May 2005 over midlatitudes in the day and night sectors simultaneously. *Journal of Geophysical Research Space Physics*, *119*(6), 5020–5031. https://doi.org/10.1002/2013ja019679

57. García-Herrera, R., Calvo, N., Garcia, R. R., & Giorgetta, M. A. (2006). Propagation of ENSO temperature signals into the middle atmosphere: A comparison of two general circulation models and ERA-40 reanalysis data. *Journal of Geophysical Research Atmospheres*, *111*(D6). https://doi.org/10.1029/2005jd006061

58. Gardner, C. S., Zhao, Y., & Liu, A. Z. (2002). Atmospheric stability and gravity wave dissipation in the mesopause region. *Journal of Atmospheric and Solar-Terrestrial Physics*, *64*(8–11), 923–929. https://doi.org/10.1016/s1364-6826(02)00047-0

59. Ghobadi, H., Savas, C., Spogli, L., Dovis, F., Cicone, A., & Cafaro, M. (2020). A Comparative Study of Different Phase Detrending Algorithms for Scintillation Monitoring. *2020 XXXIIIrd General Assembly and Scientific Symposium of the International Union of Radio Science*, 1–4. https://doi.org/10.23919/ursigass49373.2020.9232349

60. Ghoddousi-Fard, R., Héroux, P., Danskin, D. W., & Boteler, D. H. (2011). Developing a GPS TEC mapping service over Canada. *Space Weather-the International Journal of Research and Applications*, *9*(6), n/a. https://doi.org/10.1029/2010sw000621

61. Gonzalez, W. D., Joselyn, J. A., Kamide, Y., Kroehl, H. W., Rostoker, G., Tsurutani, B. T., & Vasyliunas, V. M. (1994). What is a geomagnetic storm? *Journal of Geophysical Research*, *99*(A4), 5771–5792. https://doi.org/10.1029/93ja02867

62. Gonzalez, W. D., Tsurutani, B. T., & De Gonzalez, A. L. C. (1999). Interplanetary origin of geomagnetic storms. *Space Science Reviews*, *88*(3/4), 529–562. https://doi.org/10.1023/a:1005160129098

63. Goswami, S., Paul, A., & Haldar, S. (2018). Study of relative performance of different navigational satellite constellations under adverse ionospheric conditions. *Space Weather (Online)*, *16*(6), 667–675. https://doi.org/10.1029/2017sw001762

64. Government of Canada, Natural Resources Canada, Canadian Hazards Information Service. (2021, March 22). *Ionospheric conditions*. https://www.spaceweather.gc.ca/data-donnee/ionosphere/index-en.php

65. Gu, G., & Zhou, W. (2010). Detrending moving average algorithm for multifractals. *Physical Review. E, Statistical, Nonlinear and Soft Matter Physics*, *82*(1), 1–12. https://doi.org/10.1103/physreve.82.011136

66. Gulyaeva, T. L. (1999). Regional analytical model of ionospheric total electron content: Monthly mean and standard deviation. *Radio Science*, *34*(6), 1507–1512. https://doi.org/10.1029/1999rs900080

67. Günzkofer, F., Pokhotelov, D., Stober, G., Mann, I., Vadas, S. L., Becker, E., Tjulin, A., Kozlovsky, A., Tsutsumi, M., Gulbrandsen, N., Nozawa, S., Lester, M., Belova, E., Kero, J., Mitchell, N. J., & Borries, C. (2023). Inferring neutral winds in the ionospheric transition region from atmospheric-gravity-wave traveling-ionospheric-disturbance (AGW-TID) observations with the EISCAT VHF radar and the Nordic Meteor Radar Cluster. *Annales Geophysicae*, *41*(2), 409–428. https://doi.org/10.5194/angeo-41-409-2023

68. Hausfather, Z. (2024, January 15). *2023's unexpected and unexplained warming*. Retrieved August 26, 2024, from https://skepticalscience.com/print.php?n=5850

69. He, M., Liu, L., Wan, W., Ning, B., Zhao, B., Wen, J., Yue, X., & Le, H. (2009). A study of the Weddell Sea Anomaly observed by FORMOSAT-3/COSMIC. *Journal of Geophysical Research Atmospheres*, *114*(A12). https://doi.org/10.1029/2009ja014175

70. Hines, C. O. (1960). INTERNAL ATMOSPHERIC GRAVITY WAVES AT IONOSPHERIC HEIGHTS. *Canadian Journal of Physics*, *38*(11), 1441–1481. https://doi.org/10.1139/p60-150

71. Ho, S., Zhou, X., Shao, X., Zhang, B., Adhikari, L., Kireev, S., He, Y., Yoe, J. G., Xia-Serafino, W., & Lynch, E. (2020). Initial assessment of the COSMIC-2/FORMOSAT-7 neutral atmosphere data quality in NESDIS/STAR using in situ and satellite data. *Remote Sensing*, *12*(24), 4099. https://doi.org/10.3390/rs12244099

72. Hocke, K., & Schlegel, K. (1996). A review of atmospheric gravity waves and travelling ionospheric disturbances: 1982-1995. *Annales Geophysicae*, *14*(9), 917–940. https://doi.org/10.1007/s00585-996-0917-6

73. Hyndman, J., & Athanasopoulos, G. (2018, May 8). *6.2 Moving averages | Forecasting: Principles and Practice (2nd ed)*. Retrieved July 16, 2024, from https://otexts.com/fpp2/moving-averages.html

74. Hysell, D. L., & Kudeki, E. (2004). Collisional shear instability in the equatorial F region ionosphere. *Journal of Geophysical Research*, *109*(A11). https://doi.org/10.1029/2004ja010636

75. Idosa, C., Adhikari, B., & Shogile, K. (2023). Features of ionospheric total electron content over high latitude regions during geomagnetic storm of November 04, 2021. *Indian Journal of Physics/Indian Journal of Physics/Indian Journal of Physics and Proceedings*

of the Indian Association for the Cultivation of Science, *97*(13), 3745–3757. https://doi.org/10.1007/s12648-023-02746-4

76. *Ionosphere, upper atmospheric layer, what is it?* (n.d.). BIRA-IASB. https://www.aeronomie.be/index.php/en/encyclopedia/ionosphere-upper-atmospheric-layer-what-it

77. Jakowski, N., Stankov, S., Schlueter, S., & Klaehn, D. (2006). On developing a new ionospheric perturbation index for space weather operations. *Advances in Space Research*, *38*(11), 2596–2600. https://doi.org/10.1016/j.asr.2005.07.043

78. Jan, J. (2024, May). *El Ni�o and La Ni�a Years and Intensities*. Retrieved June 10, 2024, from https://ggweather.com/enso/oni.htm

79. Jayachandran, B., Krishnankutty, T. N., & Gulyaeva, T. (2004). Climatology of ionospheric slab thickness. *Annales Geophysicae*, *22*(1), 25–33. https://doi.org/10.5194/angeo-22-25-2004

80. Jiao, Y. (2017). LOW-LATITUDE IONOSPHERIC SCINTILLATION SIGNAL SIMULATION, CHARACTERIZATION, AND DETECTION ON GPS SIGNALS [PhD, Colorado State University]. https://api.mountainscholar.org

81. Jiao, Y., & Morton, Y. T. (2015). Comparison of the effect of high-latitude and equatorial ionospheric scintillation on GPS signals during the maximum of solar cycle 24. *Radio Science*, *50*(9), 886–903. https://doi.org/10.1002/2015rs005719

82. Jiao, Y., Morton, Y. T., Taylor, S., & Pelgrum, W. (2013). Characterization of high-latitude ionospheric scintillation of GPS signals. *Radio Science*, *48*(6), 698–708. https://doi.org/10.1002/2013rs005259

83. Jin, Y., Clausen, L. B. N., Miloch, W. J., Høeg, P., Jarmołowski, W., Wielgosz, P., Paziewski, J., Milanowska, B., Hoque, M., Berdermann, J., Lyu, H., Hernandez-Pajares, M., Monte-Moreno, E., & Rigo, A. G. (2022). Climatology and modeling of ionospheric irregularities over Greenland based on empirical orthogonal function method. *Journal of Space Weather and Space Climate*, *12*, 23. https://doi.org/10.1051/swsc/2022022

84. Jin, Y., Moen, J. I., & Miloch, W. J. (2015). On the collocation of the cusp aurora and the GPS phase scintillation: A statistical study. *Journal of Geophysical Research. Space Physics*, *120*(10), 9176–9191. https://doi.org/10.1002/2015ja021449

85. Johnston, B. R., Randel, W. J., & Braun, J. J. (2022). Interannual variability of tropospheric moisture and temperature and relationships to ENSO using COSMIC-1 GNSS-RO retrievals. *Journal of Climate*, *35*(21), 7109–7125. https://doi.org/10.1175/jcli-d-21-0884.1

86. Kalita, B. R., & Bhuyan, P. K. (2017). Variations of the ionospheric parameters and vertical electron density distribution at the northern edge of the EIA from 2010 to 2015 along 95°E and comparison with the IRI-2012. *Advances in Space Research*, *60*(2), 295–306. https://doi.org/10.1016/j.asr.2016.06.041

87. Kaplan, E. D., & Hegarty, C. J. (2017). Understanding GPS/GNSS : Principles and applications third edition. *Artech House, London*. https://ieeexplore.ieee.org/document/9100468

88. Kelley, M. C., Larsen, M. F., LaHoz, C., & McClure, J. P. (1981). Gravity wave initiation of equatorial spread F: A case study. *Journal of Geophysical Research*, *86*(A11), 9087–9100. https://doi.org/10.1029/ja086ia11p09087

89. Kintner, P. M., Ledvina, B. M., & De Paula, E. R. (2007). GPS and ionospheric scintillations. *Space Weather*, *5*(9). https://doi.org/10.1029/2006sw000260

90. Knížová, P. K., Laštovička, J., Kouba, D., Mošna, Z., Podolská, K., Potužníková, K., Šindelářová, T., Chum, J., & Rusz, J. (2021). Ionosphere influenced from Lower-Lying atmospheric regions. *Frontiers in Astronomy and Space Sciences*, *8*. https://doi.org/10.3389/fspas.2021.651445

91. Krivolutsky, A. A., Cherepanova, L. A., Dement'eva, A. V., Repnev, A. I., & Klyuchnikova, A. V. (2015). Global circulation of the Earth's atmosphere at altitudes from 0 to 135 Km simulated with the ARM model. Consideration of the solar activity contribution. *Geomagnetism and Aeronomy*, *55*(6), 780–800. https://doi.org/10.1134/s0016793215060067

92. Kumar, A., Kumar, S., Lal, P., Saikia, P., Srivastava, P. K., & Petropoulos, G. P. (2021). Introduction to GPS/GNSS technology. In *Elsevier eBooks* (pp. 3–20). https://doi.org/10.1016/b978-0-12-818617-6.00001-9

93. Kumar, S. (2023). Global Navigation Satellite Systems and their applications in remote sensing of atmosphere. In *Elsevier eBooks* (pp. 39–62). https://doi.org/10.1016/b978-0-323-99262-6.00006-7

94. Kumar, S., Tan, E. L., & Murti, D. S. (2015). Impacts of solar activity on performance of the IRI-2012 model predictions from low to mid latitudes. *Earth Planets and Space*, *67*(1). https://doi.org/10.1186/s40623-015-0205-3

95. Langley, R. B., Jensen, A. O. B., & Micthell, C. (2011). GNSS and the ionosphere: What's in store in the next solar maximum? In *Space Weather and GNSS* (2nd ed., Vol. 22, pp. 40–48). GPS World. https://gge.ext.unb.ca/Resources/gpsworld.february11.pdf

96. *Layers of the atmosphere*. (2021, May 25). NIWA. https://niwa.co.nz/education-and-training/schools/students/layers

97. Li, G., Ning, B., Ren, Z., & Hu, L. (2010). Statistics of GPS ionospheric scintillation and irregularities over polar regions at solar minimum. *GPS Solutions*, *14*(4), 331–341. https://doi.org/10.1007/s10291-009-0156-x

98. Lieberman, R. S., Riggin, D. M., Ortland, D. A., Nesbitt, S. W., & Vincent, R. A. (2007). Variability of mesospheric diurnal tides and tropospheric diurnal heating during 1997–1998. *Journal of Geophysical Research*, *112*(D20). https://doi.org/10.1029/2007jd008578

99. Lindsey, R. & National Oceanic and Atmospheric Administration [NOAA]. (2009, September 1). *Climate change: incoming sunlight*. NOAA Climate.gov. Retrieved August 2, 2024, from https://www.climate.gov/news-features/understanding-climate/climate-change-incoming-sunlight

100. Liu, J. Y., Sun, Y. Y., Kakinami, Y., Chen, C. H., Lin, C. H., & Tsai, H. F. (2011). Bow and stern waves triggered by the Moon's shadow boat. *Geophysical Research Letters*, *38*(17), n/a. https://doi.org/10.1029/2011gl048805

101. Liu, J. Y., Tsai, Y. B., Chen, S. W., Lee, C. P., Chen, Y. C., Yen, H. Y., Chang, W. Y., & Liu, C. (2006). Giant ionospheric disturbances excited by the M9.3 Sumatra earthquake of 26 December 2004. *Geophysical Research Letters*, *33*(2). https://doi.org/10.1029/2005gl023963

102. Liu, L., & Chen, Y. (2009). Statistical analysis of solar activity variations of total electron content derived at Jet Propulsion Laboratory from GPS observations. *Journal of Geophysical Research Atmospheres*, *114*(A10). https://doi.org/10.1029/2009ja014533

103. Lu, X. (2006). Global positioning system: A field guide for the social sciences – John Spencer, Erian G. Frizzelle, Philip H. Page and John B. Vogler. *Singapore Journal of Tropical Geography*, *27*(1), 104–106. https://doi.org/10.1111/j.1467-9493.2006.00243.x

104. Macalalad, E. P., Tsai, L. C., & Wu, J. (2014). Performance evaluation of different ionospheric models in single-frequency code-based differential GPS positioning. *GPS Solutions*, *20*(2), 173–185. https://doi.org/10.1007/s10291-014-0422-4

105. Mannucci, A. J., Wilson, B. D., Yuan, D. N., Ho, C. H., Lindqwister, U. J., & Runge, T. F. (1998). A global mapping technique for GPS-derived ionospheric total electron content measurements. *Radio Science*, *33*(3), 565–582. https://doi.org/10.1029/97rs02707

106. Mansoori, A. A., Khan, P. A., Bhawre, P., Gwal, A. K., & Purohit, P. K. (2013). Variability of TEC at mid latitude with solar activity during the solar cycle 23 and 24. *Conference Paper*. https://doi.org/10.1109/iconspace.2013.6599438

107. Martin-Puertas, C., Matthes, K., Brauer, A., Muscheler, R., Hansen, F., Petrick, C., Aldahan, A., Possnert, G., & Van Geel, B. (2012). Regional atmospheric circulation shifts induced by a grand solar minimum. *Nature Geoscience*, *5*(6), 397–401. https://doi.org/10.1038/ngeo1460

108. Martyn, D. F. (1947). Location of the currents causing the solar and lunar diurnal magnetic variations. *Nature*, *160*(4068), 535–537. https://doi.org/10.1038/160535b0

109. Matzka, J., Stolle, C., Yamazaki, Y., Bronkalla, O., & Morschhauser, A. (2021). The Geomagnetic KP index and derived indices of geomagnetic activity. *Space Weather*, *19*(5). https://doi.org/10.1029/2020sw002641

110. McLachlan, R. (2020, September 1). *Climate explained: Sunspots do affect our weather, a bit, but not as much as other things*. The Conversation. Retrieved September 11, 2024, from https://theconversation.com/climate-explained-sunspots-do-affect-our-weather-a-bit-but-not-as-much-as-other-things-145101

111. Mendillo, M. (2006). Storms in the ionosphere: Patterns and processes for total electron content. *Reviews of Geophysics*, *44*(4). https://doi.org/10.1029/2005rg000193

112. Nappo, C. J. (2012). Gravity waves in the middle and upper atmosphere. In *International geophysics/International geophysics series* (pp. 181–199). https://doi.org/10.1016/b978-0-12-385223-6.00007-0

113. National Oceanic and Atmospheric Administration [NOAA]. (n.d.). *Space weather impacts on climate*. Space Weather Prediction Center | National Oceanic and Atmospheric Administration. Retrieved August 2, 2024, from https://www.swpc.noaa.gov/impacts/space-weather-impacts-climate

114. Newman, P. A., Coy, L., Pawson, S., & Lait, L. R. (2016). The anomalous change in the QBO in 2015–2016. *Geophysical Research Letters*, *43*(16), 8791–8797. https://doi.org/10.1002/2016gl070373

115. Nishioka, M., Saito, S., Tao, C., Shiota, D., Tsugawa, T., & Ishii, M. (2021). Statistical analysis of ionospheric total electron content (TEC): long-term estimation of

extreme TEC in Japan. *Earth, Planets and Space*, *73*(1). https://doi.org/10.1186/s40623-021-01374-8

116. Nishioka, M., Tsugawa, T., Kubota, M., & Ishii, M. (2013). Concentric waves and short-period oscillations observed in the ionosphere after the 2013 Moore EF5 tornado. *Geophysical Research Letters*, *40*(21), 5581–5586. https://doi.org/10.1002/2013gl057963

117. NOAA's National Weather Service. (2020, September 15). *Hello Solar Cycle 25*. National Weather Service. Retrieved June 25, 2024, from https://www.weather.gov/news/201509-solar-cycle

118. Nykiel, G., Zanimonskiy, Y. M., Koloskov, A. V., & Figurski, M. (2019). The possibility of estimating the height of the ionospheric inhomogeneities based on TEC variations maps obtained from dense GPS network. *Advances in Space Research*, *64*(10), 2002–2011. https://doi.org/10.1016/j.asr.2019.06.008

119. Offenbacher, C., & Thornstrom, E. (2020). *Ionospheric models for GNSS measurements: Comparison of the websites IMPC, SeSolStorm and SWEPOS*. KTH Royal Institute of Technology. https://www.diva-portal.org/smash/get/diva2:1447441/FULLTEXT01.pdf

120. Okoh, D., McKinnell, L., Cilliers, P., Okere, B., Okonkwo, C., & Rabiu, B. (2014). IRI-vTEC versus GPS-vTEC for Nigerian SCINDA GPS stations. *Advances in Space Research*, *55*(8), 1941–1947. https://doi.org/10.1016/j.asr.2014.06.037

121. Osei-Poku, L., Tang, L., Chen, W., & Mingli, C. (2021). Evaluating Total Electron Content (TEC) Detrending Techniques in Determining Ionospheric Disturbances during

Lightning Events in A Low Latitude Region. *Remote Sensing*, *13*(23), 4753. https://doi.org/10.3390/rs13234753

122. Parashar, A. (2024, June 4). Top 10 Python Libraries. *Code 360 by Coding Ninjas*. Retrieved July 5, 2024, from https://www.naukri.com/code360/library/python-libraries

123. Pedatella, N. M., & Forbes, J. M. (2009). Interannual variability in the longitudinal structure of the low-latitude ionosphere due to the El Niño–Southern Oscillation. *Journal of Geophysical Research*, *114*(A12). https://doi.org/10.1029/2009ja014494

124. Pedatella, N. M., & Liu, H. (2013). Influence of the El Niño Southern Oscillation on the middle and upper atmosphere. *Journal of Geophysical Research Space Physics*, *118*(5), 2744–2755. https://doi.org/10.1002/jgra.50286

125. Pi, X., Mannucci, A. J., Lindqwister, U. J., & Ho, C. M. (1997). Monitoring of global ionospheric irregularities using the Worldwide GPS Network. *Geophysical Research Letters*, *24*(18), 2283–2286. https://doi.org/10.1029/97gl02273

126. Pogoreltsev, A., Vlasov, A., Fröhlich, K., & Jacobi, C. (2007). Planetary waves in coupling the lower and upper atmosphere. *Journal of Atmospheric and Solar-Terrestrial Physics*, *69*(17–18), 2083–2101. https://doi.org/10.1016/j.jastp.2007.05.014

127. Pradipta, R., Valladares, C. E., & Doherty, P. H. (2015). An effective TEC data detrending method for the study of equatorial plasma bubbles and traveling ionospheric disturbances. *Journal of Geophysical Research. Space Physics*, *120*(12). https://doi.org/10.1002/2015ja021723

128. Prikryl, P., Ghoddousi-Fard, R., Kunduri, B. S. R., Thomas, E. G., Coster, A. J., Jayachandran, P. T., Spanswick, E., & Danskin, D. W. (2013). GPS phase scintillation and

proxy index at high latitudes during a moderate geomagnetic storm. *Annales Geophysicae*, *31*(5), 805–816. https://doi.org/10.5194/angeo-31-805-2013

129. Prikryl, P., Jayachandran, P. T., Chadwick, R., & Kelly, T. D. (2015). Climatology of GPS phase scintillation at northern high latitudes for the period from 2008 to 2013. *Annales Geophysicae*, *33*(5), 531–545. https://doi.org/10.5194/angeo-33-531-2015

130. Prikryl, P., Jayachandran, P. T., Mushini, S. C., & Chadwick, R. (2011). Climatology of GPS phase scintillation and HF radar backscatter for the high-latitude ionosphere under solar minimum conditions. *Annales Geophysicae*, *29*(2), 377–392. https://doi.org/10.5194/angeo-29-377-2011

131. Prikryl, P., Jayachandran, P. T., Mushini, S. C., Pokhotelov, D., MacDougall, J. W., Donovan, E., Spanswick, E., & St-Maurice, J. (2010). GPS TEC, scintillation and cycle slips observed at high latitudes during solar minimum. *Annales Geophysicae*, *28*(6), 1307–1316. https://doi.org/10.5194/angeo-28-1307-2010

132. Radicella, S. M., & Migoya-Orué, Y. (2021). GNSS-derived data for the study of the ionosphere. In *Elsevier eBooks* (pp. 221–239). https://doi.org/10.1016/b978-0-12-818617-6.00020-2

133. Ramuglia, G. (2023, September 7). Python Libraries: Your Comprehensive guide - Linux Dedicated Server blog. *Linux Dedicated Server Blog*. Retrieved July 5, 2024, from https://ioflood.com/blog/python-libraries/#:~:text=Python%20libraries%20are%20collections%20of,to%20perform%20various%20tasks%20efficiently.

134. Randel, W. J., & Wu, F. (2015). Variability of Zonal Mean Tropical Temperatures Derived from a Decade of GPS Radio Occultation Data. *Journal of the Atmospheric Sciences*, *72*(3), 1261–1275. https://doi.org/10.1175/jas-d-14-0216.1

135. Rao, P. V. S., Niranjan, K., Prasad, D. S. V. V., Krishna, S., & Uma, G. (2006). On the validity of the ionospheric pierce point (IPP) altitude of 350 km in the Indian equatorial and low-latitude sector. *Annales Geophysicae*, *24*(8), 2159–2168. https://doi.org/10.5194/angeo-24-2159-2006

136. Rao, P. V. S. R., Krishna, S. G., Niranjan, K., & Prasad, D. S. V. V. D. (2006a). Study of spatial and temporal characteristics of L-band scintillations over the Indian low-latitude region and their possible effects on GPS navigation. *Annales Geophysicae*, *24*(6), 1567–1580. https://doi.org/10.5194/angeo-24-1567-2006

137. Rao, P. V. S. R., Krishna, S. G., Niranjan, K., & Prasad, D. S. V. V. D. (2006b). Temporal and spatial variations in TEC using simultaneous measurements from the Indian GPS network of receivers during the low solar activity period of 2004–2005. *Annales Geophysicae*, *24*(12), 3279–3292. https://doi.org/10.5194/angeo-24-3279-2006

138. Rao, S. S., & Singh, A. K. (2021). Chapter 7: Probing the upper Atmosphere using GPS: Introduction. In G. P. P Petropoulos & P. K. Srivastava (Eds.), *GPS and GNSS Technology in Geosciences* (pp. 135–153). Elsevier Inc. https://doi.org/10.1016/b978-0-12-818617-6.00011-1

139. Rohde, R. (2024, February 29). *Global Temperature Report for 2023 - Berkeley Earth*. Berkeley Earth. https://berkeleyearth.org/global-temperature-report-for-2023/

140. Romero-Hernandez, E., Denardini, C. M., Jonah, O. F., Essien, P., Picanço, G. a. S., Nogueira, P. a. B., Rodriguez-Martinez, M., Resende, L. C. A., De La Luz, V., Aguilar-Rodriguez, E., Sergeeva, M., Gonzalez-Esparza, J. A., Takahashi, H., & Perez-Tijerina, E. (2020). Nighttime Ionospheric TEC study over Latin America during moderate and high solar activity. *Journal of Geophysical Research. Space Physics*, *125*(10). https://doi.org/10.1029/2020ja028210

141. Ruston, B., & Healy, S. (2020). Forecast impact of FORMOSAT -7/ COSMIC -2 GNSS radio occultation measurements. *Atmospheric Science Letters*, *22*(3). https://doi.org/10.1002/asl.1019

142. Saba, M. M. F., Gonzalez, W. D., & De Gonzalez, A. L. C. (1994). Relationships Between the AE, ap and Dst Indices. *Solar-Terrestrial Energy Program*, 435. https://ui.adsabs.harvard.edu/abs/1994step.conf..435S/abstract

143. Şahbazoğlu, İ. (2024, February 20). Time series decomposition and moving average smoothing. *Medium*. https://medium.com/@ipeksahbazoglu/time-series-decomposition-and-moving-average-smoothing-fd61b558ca36#:~:text=The%20classical%20method%20of%20time,understand%20underlying%20stock%20price%20behaviours.

144. Sajedi, S. A., & Abdollahi, F. (2012). Geomagnetic disturbances may be environmental risk factor for multiple sclerosis: an ecological study of 111 locations in 24 countries. *BMC Neurology*, *12*(1). https://doi.org/10.1186/1471-2377-12-100

145. Salby, M. L. (1996). *Fundamentals of Atmospheric Physics*. Academic Press.

146. Sankar, J. (2021, October 19). *Introduction to ionospheric propagation*. Electronics for You. Retrieved May 7, 2024, from https://www.electronicsforu.com/technology-trends/learn-electronics/ionospheric-propagation

147. Scherllin-Pirscher, B., Deser, C., Ho, S., Chou, C., Randel, W., & Kuo, Y. (2012). The vertical and spatial structure of ENSO in the upper troposphere and lower stratosphere from GPS radio occultation measurements. *Geophysical Research Letters*, *39*(20). https://doi.org/10.1029/2012gl053071

148. Scherllin-Pirscher, B., Deser, C., Ho, S., Chou, C., Randel, W., & Kuo, Y. (2012). The vertical and spatial structure of ENSO in the upper troposphere and lower stratosphere from GPS radio occultation measurements. *Geophysical Research Letters*, *39*(20). https://doi.org/10.1029/2012gl053071

149. Schreiner, W., Weiss, J., Anthes, R., Braun, J., Chu, V., Fong, J., Hunt, D., Kuo, Y., Meehan, T., Serafino, W., Sjoberg, J., Sokolovskiy, S., Talaat, E., Wee, T., & Zeng, Z. (2020). COSMIC-2 Radio Occultation Constellation: First Results. *Geophysical Research Letters*, *47*(4). https://doi.org/10.1029/2019gl086841

150. Schwartz, M., Lambert, A., Manney, G. L., Read, W. G., Livesey, N. J., Froidevaux, L., Ao, C. O., Bernath, P. F., Boone, C. D., Cofield, R. E., Daffer, W. H., Drouin, B. J., Fetzer, E. J., Fuller, R. A., Jarnot, R. F., Jiang, J., Jiang, Y., Knosp, B., Krüger, K., . . . Wu, D. L. (2008). Validation of the Aura Microwave Limb Sounder temperature and geopotential height measurements. *Journal of Geophysical Research*, *113*(D15). https://doi.org/10.1029/2007jd008783

151. Seba, E. B., Nigussie, M., Giday, N. M., & Moldwin, M. B. (2021). The relationship between upward propagating atmospheric gravity waves and ionospheric irregularities during solar minimum periods. *Space Weather*, *19*(11). https://doi.org/10.1029/2021sw002715

152. Seemala, G. (2011, April 4). *GPS-TEC analysis program (version 3.5)*. Gopi Seemala. Retrieved June 26, 2024, from https://seemala.blogspot.com/2024/04/gps-tec-analysis-program-version-35.html

153. Seemala, G. K. (2023). Chapter 4: Estimation of Ionospheric Total Electron Content (TEC) from GNSS observations: Ionospheric layers. In *Atmospheric Remote Sensing* (pp. 63–84). Elsevier Ltd. https://doi.org/10.1016/b978-0-323-99262-6.00022-5

154. Shenvi, N., & Virani, H. (2023). Forecasting of ionospheric total electron content data using multivariate deep LSTM model for different latitudes and solar activity. *Journal of Electrical and Computer Engineering*, *2023*, 1–13. https://doi.org/10.1155/2023/2855762

155. Singh, A. K., Das, R. M., & Saini, S. (2019). Variations of total electron content over high latitude region during the ascending phase of 24th solar cycle. *Advances in Space Research*, *63*(11), 3558–3567. https://doi.org/10.1016/j.asr.2019.02.017

156. Space weather impacts on climate | NOAA / NWS Space Weather Prediction Center. (n.d.). https://www.swpc.noaa.gov/impacts/space-weather-impacts-climate

157. Straus, P. (2023). *COSMIC-2 Data products*. The Aerospace Corporation. https://www.swpc.noaa.gov/sites/default/files/images

158. Straus, P., Schreiner, W., Wheeler, I., Talaat, E., COSMIC - 2 Mission, & Wu, J.-S. (Directors). (2022). FORMOSAT-7/COSMIC-2 Space Weather Data Release 5. In *COSMIC - 2 FORMOSAT - 7*. National Oceanic and Atmospheric Administration.

159. Sumod, S. G., & Pant, T. K. (2019). An investigation of solar flare effects on equatorial ionosphere and thermosphere using co-ordinated measurements. *Earth, Planets and Space*, *71*(1). https://doi.org/10.1186/s40623-019-1105-8

160. Sun, Y. (2019). GNSS brings us back on the ground from ionosphere. *Geoscience Letters*, *6*(1). https://doi.org/10.1186/s40562-019-0144-0

161. Sun, Y., Liu, H., Miyoshi, Y., Chang, L. C., & Liu, L. (2019). El Niño–Southern Oscillation effect on ionospheric tidal/SPW amplitude in 2007–2015 FORMOSAT-3/COSMIC observations. *Earth Planets and Space*, *71*(1). https://doi.org/10.1186/s40623-019-1009-7

162. Sun, Y., Liu, H., Miyoshi, Y., Liu, L., & Chang, L. C. (2018). El Niño–Southern Oscillation effect on quasi-biennial oscillations of temperature diurnal tides in the mesosphere and lower thermosphere. *Earth, Planets and Space*, *70*(1). https://doi.org/10.1186/s40623-018-0832-6

163. Sun, Y., Matsuo, T., Araujo-Pradere, E. A., & Liu, J. (2013). Ground-based GPS observation of SED-associated irregularities over CONUS. *Journal of Geophysical Research. Space Physics*, *118*(5), 2478–2489. https://doi.org/10.1029/2012ja018103

164. Sun, Y. Y., Liu, H., Miyoshi, Y., Chang, L. C., & Liu, L. (2019). El Niño–Southern Oscillation effect on ionospheric tidal/SPW amplitude in 2007–2015 FORMOSAT-

3/COSMIC observations. *Earth, Planets and Space*, *71*(1). https://doi.org/10.1186/s40623-019-1009-7

165. Takahashi, H., Wrasse, C. M., Denardini, C. M., Pádua, M. B., De Paula, E. R., Costa, S. M. A., Otsuka, Y., Shiokawa, K., Monico, J. F. G., Ivo, A., & Sant'Anna, N. (2016). Ionospheric TEC Weather Map over South America. *Space Weather*, *14*(11), 937–949. https://doi.org/10.1002/2016sw001474

166. Tal, D. (2024, January 6). *Understanding HF Propagation: Predict, Tutorial, Apps, Tools*. Retrieved June 12, 2024, from https://www.qsl.net/4x4xm/HF-Propagation.htm#SStCA

167. Tariku, Y. A. (2020). Assessment of Variability of the TEC in the Equatorial Anomaly Region with a Focus over Africa Using Rz and F10.7 as Input Drivers. *The Astronomical Journal*, *160*(4), 185. https://doi.org/10.3847/1538-3881/abaf02

168. Tariku, Y. A. (2021). The geomagnetic storm time response of the mid latitude ionosphere during Solar Cycle 24. *Radio Science*, *56*(12). https://doi.org/10.1029/2021rs007340

169. Thabit, S. A., George, L. E., & Hadi, K. A. (2020). Seasonal variations of the optimum reliable frequencies during maximum and minimum periods of solar cycle 24. *Mağallaẗ ʻulūm Al-mustanṣiriyyaẗ/Mustansiriyah Journal of Science*, *31*(4), 15–27. https://doi.org/10.23851/mjs.v31i4.887

170. The COMET Program/MetEd. (2019, May 23). *FORMOSAT-7/COSMIC-2 Satellite System: Next gen weather & Climate observations* [Video]. YouTube. https://www.youtube.com/watch?v=qabMHoMyl1A

171. *The global climate 2011-2015: heat records and high impact weather*. (2016, October 14). PreventionWeb. https://www.preventionweb.net/news/global-climate-2011-2015-heat-records-and-high-impact-weather

172. Tiwari, R., Ghafoori, F., Al-Fanek, O., Haddad, O., Skone, S., & Tiwari, R. (2010). Investigation of high latitude ionospheric scintillations observed in the Canadian region. *Proceedings of the 23rd International Technical Meeting of the Satellite Division of the Institute of Navigation (ION GNSS 2010)*, 349–360. https://eprint.ncl.ac.uk/file_store/production/167749/8B9CD681-4C08-41B8-B069-0A3EF6BDFD1F.pdf

173. Tsuchiya, S., Shiokawa, K., Takeo, D., Fujinami, H., Otsuka, Y., Matsuda, T. S., Ejiri, M. K., Nakamura, T., & Yamamoto, M. (2017). Long-term statistical analysis of horizontal phase velocity distribution of mesosphere and ionosphere waves in airglow images at Rikubetsu and Shigaraki, Japan. *Japan Geoscience Union*. https://confit.atlas.jp/guide/event/jpguagu2017/subject/E_PEM11-P06/detail

174. Tsuda, T. (2014). Characteristics of atmospheric gravity waves observed using the MU (Middle and Upper atmosphere) radar and GPS (Global Positioning System) radio occultation. *Proceedings of the Japan Academy Series B*, *90*(1), 12–27. https://doi.org/10.2183/pjab.90.12

175. Tsugawa, T., Otsuka, Y., Coster, A. J., & Saito, A. (2007). Medium-scale traveling ionospheric disturbances detected with dense and wide TEC maps over North America. *Geophysical Research Letters*, *34*(22). https://doi.org/10.1029/2007gl031663

176. Turner, S. (2014, November 4). *Sunspots and propagation - Ham Radio School.com*. Ham Radio School.com. https://web.archive.org/web/20170626024320/http://www.hamradioschool.com/sunspots-and-propagation/

177. Valls, J. V., Linty, N., Closas, P., Dovis, F., & Curran, J. T. (2020). Survey on signal processing for GNSS under ionospheric scintillation: Detection, monitoring, and mitigation. *NAVIGATION Journal of the Institute of Navigation*, *67*(3), 511–536. https://doi.org/10.1002/navi.379

178. Van Der Meeren, C., Oksavik, K., Lorentzen, D. A., Paxton, L. J., & Clausen, L. B. N. (2016). Scintillation and irregularities from the nightside part of a Sun-aligned polar cap arc. *Journal of Geophysical Research. Space Physics*, *121*(6), 5723–5736. https://doi.org/10.1002/2016ja022708

179. Vasylyev, D., Béniguel, Y., Volker, W., Kriegel, M., & Berdermann, J. (2022). Modeling of ionospheric scintillation. *Journal of Space Weather and Space Climate*, *12*, 22. https://doi.org/10.1051/swsc/2022016

180. Villalobos, J., & Valladares, C. E. (2019). Statistical analysis of TEC distributions observed over South and Central America. *Radio Science*, *55*(1). https://doi.org/10.1029/2018rs006725

181. Wang, H., Liu, D., Xia, Y., Xie, W., & Wang, Y. (2023). Retrieval of Atmospheric Temperature Profile from Historical Data and Ground-Based Observations by Using a Machine Learning Algorithm. *Remote Sensing*, *15*(11), 2717. https://doi.org/10.3390/rs15112717

182. Wells, D., & Beck, N. (1986). *Guide to GPS positioning*. https://perpustakaan.big.go.id/opacbig/index.php?p=show_detail&id=2239&keywords=

183. World Health Organization: WHO. (2023, November 9). *El Niño Southern Oscillation (ENSO)*. https://www.who.int/news-room/fact-sheets/detail/el-nino-southern-oscillation-(enso)#:~:text=ENSO%20affects%20many%20parts%20of,particularly%20vulnerable%20to%20natural%20hazards.

184. Xia, L. (2020, September 25). *Atmospheric thermodynamics: dry and moist adiabatic lapse rate* [Slide show]. The University of Utah. https://www.inscc.utah.edu/~krueger/5300/lapse_rates.pdf

185. Yeh, K. C., & Liu, C. H. (1974). Acoustic-gravity waves in the upper atmosphere. *Reviews of Geophysics*, *12*(2), 193–216. https://doi.org/10.1029/rg012i002p00193

186. Yiğit, E. (2017). Dynamics of the Atmosphere-Ionosphere system. In *SpringerBriefs in earth sciences* (pp. 103–133). https://doi.org/10.1007/978-3-319-62006-0_5

187. Yiğit, E., Knížová, P. K., Georgieva, K., & Ward, W. (2016). A review of vertical coupling in the Atmosphere–Ionosphere system: Effects of waves, sudden stratospheric warmings, space weather, and of solar activity. *Journal of Atmospheric and Solar-Terrestrial Physics*, *141*, 1–12. https://doi.org/10.1016/j.jastp.2016.02.011

188. Yiğit, E., & Medvedev, A. S. (2015). Internal wave coupling processes in Earth's atmosphere. *Advances in Space Research*, *55*(4), 983–1003. https://doi.org/10.1016/j.asr.2014.11.020

189. Yulaeva, E., & Wallace, J. M. (1994). The Signature of ENSO in Global Temperature and Precipitation Fields Derived from the Microwave Sounding Unit. *Journal of Climate*, *7*(11), 1719–1736. https://doi.org/10.1175/1520-0442(1994)007

190. Zhang, B., Ho, S., Cao, C., Shao, X., Dong, J., & Chen, Y. (2022). Verification and validation of the COSMIC-2 excess phase and bending angle algorithms for data quality assurance at STAR. *Remote Sensing*, *14*(14), 3288. https://doi.org/10.3390/rs14143288

191. Zhao, B., Wan, W., & Liu, L. (2005). Responses of equatorial anomaly to the October-November 2003 superstorms. *Annales Geophysicae*, *23*(3), 693–706. https://doi.org/10.5194/angeo-23-693-2005

APPENDIX

APPENDIX A

A.1 Python programming code for plotting VTEC and dVTEC graphs

```
import os

import pandas as pd

import numpy as np

import matplotlib.pyplot as plt

from scipy.stats import norm

import re

from pathlib import Path

def clean_text(text):
```

```
    # Remove non-alphabetic characters
    cleaned_text = re.sub('[^a-zA-Z,]', ' ', text)
    # Convert to lowercase
    cleaned_text = cleaned_text.upper()
    return cleaned_text
def get_graph_date(filename: str) -> str:
    parts = filename.split('-')
 date_str: list = parts[1:]
 return "-".join(date_str)
def get_graph_country(path: Path) -> str:
    country = ""
    with open(path, 'r') as file:
        country = file.readline()
       return country
# Defining column names
column_names = ['MJdatet', 'Time', 'PRN', 'Az',
                'Ele', 'Lat', 'Lon', 'Stec', 'Vtec', 'S4']
```

```
root_dir = Path("./masters-code/new_data/El_Nino")

for root, folders, files in os.walk(root_dir):

    for filename in files:

        path = Path(f'{root}/{filename}')

        print(f"Processing {path}")

   name = os.path.basename(filename).split('.')[0]

        data = pd.read_csv(path, sep='\t',

                           skiprows=5, header=None, names=column_names)

   # excel_output_path = "data.xlsx"

        # data.to_excel(excel_output_path, index=False)

   # Assigning the correct column names to the DataFrame

        data.columns = column_names

  # Select columns Time,PRN and Vtec

        selected_columns = data[["Time", "PRN", "Vtec"]]

  # Convert 'Time' column to datetime format

        selected_columns['Time'] = pd.to_datetime(

            selected_columns['Time'], unit='ms')
```

```
# Deal with negative time values
    selected_columns = selected_columns[selected_columns['Time'] >= pd.Timestamp(
        0)]
  # Sort the data by Time and PRN to ensure proper rolling
    selected_columns.sort_values(by=['PRN', 'Time'], inplace=True)
# Set the rolling window size (e.g., 30 observations)
    window_size = 30
# Group by PRN and apply a rolling mean to calculate the detrended VTEC
    selected_columns['Rolling_Mean'] = selected_columns.groupby('PRN')['Vtec'].transform(
        lambda x: x.rolling(window=window_size, min_periods=1).mean())
    detrended_vtec = selected_columns['Vtec'] - \
        selected_columns['Rolling_Mean']
# Create a new DataFrame with detrended VTEC and Time
    detrended_data = pd.DataFrame({
        'Time': selected_columns['Time'],
        'dVtec': detrended_vtec,
        'Rolling_Mean': selected_columns['Rolling_Mean']
```

```
    })
 # Drop rows where detrended VTEC is NaN (if any)
    detrended_data.dropna(inplace=True)
# Plotting detrended VTEC and Rolling Mean
    plt.figure(figsize=(10, 6))
 # Averaging the detrended VTEC data by time
    average_detrended_vtec = detrended_data.groupby('Time')['dVtec'].mean()
    average_rolling_mean = detrended_data.groupby(
      'Time')['Rolling_Mean'].mean()
  # Plotting the smoothed curves
    plt.figure(figsize=(14, 7))
graph_date = get_graph_date(name)
    graph_country = clean_text(get_graph_country(path))
 # Plot detrended Moving Average STEC as a curve
    plt.subplot(2, 1, 1)
    plt.plot(average_rolling_mean.index, average_rolling_mean.values,
         label='Rolling Mean', color='red', linestyle='--')
```

```
plt.xlabel('Local time (hours)')
plt.ylabel('VTEC')
plt.title(f'VTEC against Local time on {graph_date} in {graph_country}. (El Nino)')
plt.legend()
plt.grid(True)
    # Plot Moving Average STEC as a curve
plt.subplot(2, 1, 2)
plt.plot(average_detrended_vtec.index,
     average_detrended_vtec.values, label='Detrended VTEC')
plt.xlabel('Local time (hours)')
plt.ylabel('DVTEC')
# plt.title(f'VTEC against Local time on {graph_date} in {graph_country}. (El Nino)')
plt.legend()
plt.grid(True)
plt.tight_layout()
# plt.show()
plt.savefig(f"./graph/{name}.png")
```

```
    print(f"{name}.png plotted")

    plt.close()
```

A.2 Python programming code for plotting temperature perturbation profile graph

```
temp =

xr.open_dataset("/home/josh/Desktop/atmPrf_C2E1.2023.341.00.00.G04_0001.0001_nc")

temp

temp=temp["Temp"]

# temp = temp['Temp']

# # Calculate temperature anomaly (difference from mean)

# temp_anomaly = temp - temp.mean(dim='MSL_alt')

# Plot the temperature anomaly against altitude

fig, ax = plt.subplots(figsize=(10, 6))

temp.plot(y='MSL_alt', ax=ax)

plt.title('Temperature Perturbation vs Altitude')

plt.xlabel('Temperature Pertubation (C)')

plt.ylabel('Altitude (km)')

#plt.grid(True)
```

```
plt.show()
```